The Mechanics of Drug Dissolution

A demonstration of the potential of mathematical and numerical methods for solving flow related problems in pharmaceutics

Niall McMahon BA, BAI

A Dissertation Presented to Dublin City University for the Degree of Doctor of Philosophy

Under the supervision of Dr. Martin Crane, Professor Heather J. Ruskin, and Professor Lawrence Crane

School of Computing

July 2008

Declaration

"I hereby certify that this material, which I now submit for assessment on the programme of study leading to the award of Doctor of Philosophy is entirely my own work, that I have exercised reasonable care to ensure that the work is original, and does not to the best of my knowledge breach any law of copyright, and has not been taken from the work of others save and to the extent that such work has been cited and acknowledged within the text of my work".

Niall McMahon

Dublin City University, Monday July 7th 2008.

Student Number: 52171230

To my parents Deirdre and Michael, my sister Ciara, my brothers Simon and Aidan, to Gladys and Tommy and, of course,

To Maggie

Acknowledgements

"It is well, then, to write in a modest and straightforward manner, and to give others their due amount of credit" [1].

With a glad heart, I think of all those who have helped me in various ways over these past few years. Many people and groups made this thesis possible; those I would like to thank include: Dublin City University. Martin Clynes and Mairead Callan of the National Institute for Cellular Biotechnology (NICB) for their help. A NICB scholarship enabled me to undertake these studies. My DCU advisors Martin Crane and Heather Ruskin for offering me this opportunity and for the guidance and encouragement they gave me. Lawrence Crane, my auxiliary advisor, whose active retirement, help, encouragement and ideas will always be appreciated. Together with Lawrence Crane, Daphne Gilbert and Brendan Redmond of DIT were both instrumental in my move to DCU. Francis Muir of Stanford and Audrey Glauert of Cambridge for their kind help. Sustainable Energy Ireland (SEI) and Brian Hurley, formerly of Airtricity. The people of the Institute for Numerical Computation and Analysis (INCA), in particular, Diarmuid Herlihy. INCA sponsored my attendance at EWEC 2004. The Institute of Physics (IoP), the European Society for Mathematical and Theoretical Biology (ESMTB) and Massachusetts Institute of Technology (MIT) for various forms of support. Mike Hopkins for his encouragement.

The people who I do not know but whose work and stories informed my work. People such as Muriel Glauert and André Lévêque. There are a very many people that fall into this category, some whose work is listed in the bibliography. The story of NACA Research Authorization 201 [2] lifted my heart with its many characters and its conclusion that *"[i]f the research under that authorization left a trail that now appears aimless and confused, it was for that very reason typical of most research into the unknown"*.

My acquaintances who have helped in many varied ways. Eoin Dormer, Jonathan

McGuinness and Michael Conry, for their steadfastness; John, in particular, Robert, Neal, Eoin, David and Adrian among others. Hyowon Lee for his friendship and Wasim Bashir for his kindness. In DCU, there are simply too many people to thank properly; all those who have had valuable conversations with me over many coffees and all my colleagues in the School of Computing. In particular, Dimitri Perrin, Fabrice Camous, Claire Whelan, Colm Ó hÉigeartaigh, Joachim Wagner, Caroline Sheedy, Gavin O'Gorman, Dalen Kambur, Atid Shamaie, Saba Sharifi, Adel Sharkasi among, it seems, so many others. A dedicated historian should consult the list of postgraduate students enrolled in the School of Computing from 2002. Deirdre D'Arcy in Trinity for her help, chats and always interesting ideas.

It is impossible to convey how much the love and support given to me by my, now expanding, family has meant; my parents Deirdre and Michael, my sister Ciara, my brothers Simon and Aidan, Gladys and Tommy Rowe and their children and grandchildren, and others in Dublin, Limerick and my new family in *New Europe*. Finally, I want to thank my wife, Maggie, whose love, patience and understanding have made all the difference to me.

– Niall M. McMahon, September 2008.

Contents

Abstract

The aim of this work was to increase understanding of drug dissolution in a pharmaceutical test device. The thesis that simulation *is* useful for pharmaceutics is developed and argued on the basis of three main investigations. These three distinct studies are each inspired by the original problem of tablet dissolution in the type two United States Pharmacopeia (USP) dissolution test apparatus, *the USP apparatus*. In the first study, a new finite-difference approximation to the initial drug mass transfer rate from dissolving cylindrical *tablets*, consisting of alternating layers of drug and inert material, is presented. Among other things, the primary reasons for error in previous studies are shown to be the assumption of a constant mainstream flow velocity in the USP apparatus and the differing implementation of a surface boundary condition. Extensions to this earlier work are presented. The second study relates to the flow around the top of a cylinder using a commercial fluid dynamics code. Applied to a complementary problem in wind energy, where it is recommended that wind-speed measurements are taken at least five diameters above the top of meteorological towers for accuracy, the solution techniques are relevant to the flow around a cylindrical drug compact. The third study considers one possible end-state of a dissolving tablet: fragmentation with dissolution continuing from the disintegrated solid masses. Indications are that, for particles of diameter 100 microns and smaller, forced convection effects are negligible in the USP apparatus. It is intended that the reader is left convinced of the usefulness of simulation for investigating pharmaceutical processes.

Chapter 1

Introduction

Pharmaceutics is about delivering drugs with precision [3]. Recently, a need to reduce risk[1] is motivating a shift towards the computer simulation of biological systems and pharmaceutical processes [4; 5]. Simulation in drug development will potentially lead to more successful products, fewer failures and faster time to market [6].

The dissolving compact, or *tablet*, is the most widely used method of drug delivery[2] [7]. Tablets typically consist of mixtures of the active ingredient(s) and various other components, known as *excipients*. Excipients are generally biologically inert materials used to modify some aspect of tablet performance. Dissolution tests are used to ensure consistency during tablet manufacture, to assess the dissolution characteristics of a particular tablet design, to establish *in vitro/in vivo* correlations, and to predict how the drug will perform in the body [8; 7; 9]. Dissolution tests also form a part of the drug approval process. The United States Pharmacopeia (USP) Type 2 Paddle Dissolution Apparatus, from here on referred to as *the USP apparatus*, is a standard dissolution test device, used by the Food and Drug Administration (FDA) and the pharmaceutical industry [10]. Although the USP apparatus is much used,

[1] *Risk* in the broadest sense, which includes the risk and associated financial costs of uncertainty in data, risk to the well-being of animals and humans and so forth.

[2] Tablets are normally taken orally and are designed to dissolve at specific points in the gastrointestinal (GI) tract. Other types of delivery systems targeting the GI tract exist [7].

detailed theoretical descriptions of its characteristics are still not well developed.

1.1 Mathematical and Numerical Models of Dissolution in the USP Apparatus

Higuchi's model of dissolution was developed as part of a study of the dissolution rates of polyphase, or *multi-component*, tablets[3] [11]. Recent work, carried out with two-component tablets (i.e. consisting of one drug and one excipient, dissolving in the USP apparatus), has shown that the theoretical dissolution rates predicted using this model do not always agree well with observed dissolution rates [12]. Using experiments and computer simulation, researchers have identified three examples of dissolution physics that are not captured by Higuchi's model; these are: (1) pH changes close to the surface of the dissolving tablet [13; 14], (2) the effect of excipient particle size [12], and (3) the effect of complex hydrodynamics, such as those found in the USP apparatus [15; 16; 17; 18; 19].

In 1998, the PSUDO project was launched [20]. PSUDO was a proof of concept study, designed to demonstrate how computer simulation can be used to model tablets dissolving in the USP apparatus. Healy and Corrigan's observation that increasing excipient particle size increases the drug dissolution rate [12] suggested a sensible starting point for the investigation. Could a code be developed to model diffusion and advection from a surface composed of isolated areas of an excipient and a drug, i.e. from the surface of a two-component tablet in the USP apparatus? To answer this, the project considered simple one- and two-component tablets, constructing successful (semi-)analytical and numerical solutions for drug dissolution rates.

Results from the PSUDO project have been published in two tracks: (1) studies of USP apparatus hydrodynamics and (2) mathematical and computational models

[3]Polyphase tablets consist of more than one chemical component.

of diffusion and advection. Taking as our starting point results from the second track, described in [21; 17], the initial research question arrived at was, *how can we build on this work and improve our understanding of tablet dissolution in the USP apparatus?*

1.2 Thesis Aims

The aim of this work was to make progress in understanding drug dissolution in a pharmaceutical test device. *In vitro* tests are critical to pharmaceutical development yet their physics are not well understood. In what follows, the thesis that simulation *is* useful for pharmaceutics is developed and argued through the presentation of three main, separate investigations. These three distinct studies are connected to one another in that they are inspired by the original problem of tablet dissolution in the USP apparatus. Simulations of aspects of drug dissolution are of utility, not only as isolated studies, but also as part of the development of a broader framework, which includes previous and future work, for the simulation of pharmaceutical processes.

1.3 Thesis Structure

1.3.1 Study 1

In the first study, the starting point and core of the thesis, a Crank-Nicolson finite-difference approximation to the drug mass transfer rate from dissolving cylindrical *tablets*, consisting of alternating layers of drug and inert material, is presented. Results are compared with recent solutions to the same problem and with previous experimental results produced using the USP apparatus. This first study is presented in Chapters 2 (literature review), 3 (theory and methods) and 6 (results and discussion).

1.3.2 Study 2

The second study investigated the flow around the top of a cylinder using a commercial fluid dynamics code. A specific application to a complementary problem in wind energy is considered. In addition to other sources of error, accelerated airflow, or *speed-up*, around the top of cylindrical meteorological (*met*) towers can cause incorrect wind-speed measurements. A particular configuration is considered where an anemometer, a device used to measure wind-speed, was located only 2 tower diameters above a met tower.

The second study is presented in Chapters 4 (literature review, theory and methods) and 7 (results and discussion).

1.3.3 Study 3

The third part of this work considers one possible end state of a dissolving tablet: fragmentation into small particles with dissolution continuing from the disintegrated solid masses. A framework for calculating the motion of and dissolution from a drug particle moving through the USP apparatus is outlined, beginning with a review of the classical work of Taylor and Glauert, who considered the motion of raindrops in airflows [22; 23].

The third study is presented in Chapters 5 (literature review, theory and methods) and 8 (results and discussion).

1.4 Summary

In the conclusion, this work is placed in context and the possibility of a complete treatment of drug dissolution in the USP apparatus is discussed. The aim of this work was to increase understanding of drug dissolution in the USP apparatus and the three studies presented each represent an aspect of an overall solution. Most importantly, however, the thesis presented is that simulation has significant potential

for pharmaceutics. The purpose of what follows is to demonstrate this to the reader.

1.5 Collaborators and Professional Acknowledgements

The work on flow about a cylindrical meteorological tower was completed in close collaboration with Dimitri Perrin at the School of Computing in DCU and in partnership with INCA, the Institute for Numerical Computation and Analysis. Dimitri deserves credit for much of the computational work completed for flows about hollow towers of various configurations. Professor Michael Ryan of the School of Computing at DCU provided useful suggestions about how to proceed with the extension of the Pohlhausen solution outlined. Susan Lazarus and Aongus Ó Cairbre at DIT were also instrumental in arriving at extensions to the solution for exponents of positive integers. Anne-Marie Healy and Deirdre D'Arcy of the School of Pharmacy at Trinity College Dublin provided us with grid and velocity vector data from their fluid dynamics simulation of the USP dissolution apparatus. Dr. Audrey Glauert of Cambridge University kindly provided useful insight into the work of her mother, Muriel Glauert.

1.6 Publications

1.6.1 Peer Reviewed Journals

Published papers produced from the work presented in this thesis are:

- **N. McMahon**, M. Crane, H. J. Ruskin and L. Crane, The Importance of Boundary Conditions in the Simulation of Dissolution in the USP Apparatus. Simulation Modelling Practice and Theory, Volume 15, Issue 3, March 2007, Pages 247-255.

- D. Perrin, **N. McMahon**, M. Crane, H. J. Ruskin, L. Crane and B. Hurley, The Effect of a Meteorological Tower on its Top-Mounted Anemometer.

Applied Energy, Volume 84, Issue 4, April 2007, Pages 413-424.

- **N. McMahon**, M. Crane, H. J. Ruskin and L. Crane, The Mechanics of Drug Dissolution. 2003. Proceedings in Applied Mathematics and Mechanics (PAMM), Volume 3, Issue 1, Pages 392 - 393.

1.6.2 Conference Oral Presentations

Work from this thesis was presented orally at two international conferences:

- Particle Tracking: from Raindrops in 1940 to Drug Dissolution in 2005. June 2005. Third M.I.T. Conference on Computational Fluid and Solid Mechanics. MIT, Cambridge, MA.

- The Mechanics of Drug Dissolution. GAMM 2003. Abano-Terme (Padua), Italy.

1.6.3 Conference Poster Presentations

Poster presentations of work from this thesis were prepared for two international conferences:

- D. Perrin, L. Crane, N. McMahon and B. Hurley. The Influence of Mounting Booms and Towers on Wind-Speed Measurements by Anemometers. December 2004. European Wind Energy Conference (EWEC), London.

- N. McMahon, M. Crane, H.J. Ruskin and L. Crane. Investigations into Tablet Dissolution in a Paddle Type Apparatus. Polymers in Diffusion and Drug Delivery 2003. Institute of Physics, London.

Chapter 2

Literature Review, Study 1

2.1 Introduction

A *drug* is a therapeutic or diagnostic entity and a *drug delivery system* (DDS) is a system for delivering drugs into the body [24]. *Pharmaceutics* is concerned with designing drugs *and* their delivery systems [7]. Two decades ago, the disciplines that contributed to pharmaceutics included chemistry (analytical, medicinal and biological), pharmacology (the study of the effect of drugs on organisms), toxicology and clinical medicine [25]. Today, new technologies and better theoretical understanding, drawing from disciplines such as applied mathematics, engineering and especially computing, have broadened the scope of pharmaceutics to include *bioengineering*, *computer simulation*, *computational biology* and *bioinformatics*, *genomics* and *structural genomics*, all of which can be classed as *biotechnologies* [26; 27; 28; 29]. Small biotechnology companies, many of them 21st century start-ups, have rapidly established themselves as the innovators of the pharmaceutical industry, bringing ideas from academia to the factory [27].

2.1.1 Drug Delivery Systems

Controlled Drug Delivery Systems

Drug delivery systems, specifially *controlled* drug delivery systems, are designed to deliver a drug with precision [30]. There are three main categories of controlled drug delivery systems, (i) controlled release delivery systems, (ii) localised delivery systems and (iii) targeted delivery systems [31]. Localised systems attempt to confine the drug to an organ or space in the body, while targeted systems affect only particular cell types, e.g. cancer cells.

Controlled-release systems deliver drugs at a predetermined rate appropriate to the disease, maximising the drug's effectiveness while minimising the risk of overdose and toxic effects [32; 28]. Controlled-release systems are important for treating illnesses such as diabetes, where precise delivery with time is critical and undesirable effects[1] can be fatal. Controlled-release systems can also eliminate unpleasant administration methods such as parenteral delivery (injections) and increase patient compliance and comfort [33].

In the 1950s, Smith Kline & French introduced the first controlled-release medicine, Dexedrine, in a device the company called a *Spansule* [34]. It quickly released the required initial dose and then slowly and gradually released many extremely small doses to maintain a therapeutic level lasting from 10 to 12 hours [35]. This was achieved by using between two and eight groups of drug pellets, each group coated with a different thickness of slowly dissolving inert material. The spansule used the dissolution characteristics of the drug and coating to control the drug release.

Diffusion- and dissolution-controlled systems can be classified broadly as primarily subject to either *bulk erosion* or *surface erosion*, although other advanced devices also exist including implantable microchips with onboard drug reservoirs [28]. By bulk erosion is meant that drug mass is lost uniformly throughout the system. Ero-

[1] Such effects include *dose dumping*, the rapid release of drug at a rate that quickly leads to toxic levels of drug in the bloodstream [3].

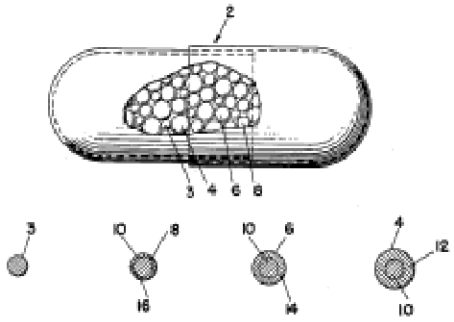

Figure 2.1: Smith Kline & French's controlled release *Spansule* delivery system. Drug delivery is regulated with pellets coated with varying thicknesses of a slowly dissolving material. Reproduced from [35].

sion rates depend on the volume of the compact. Surface eroding systems erode from the outside to the inside of the system and the erosion rate depends on the surface area of drug exposed [32]. The spansule system depended on surface erosion (Figure 2.2).

The dissolution rate of drug from a delivery system can be classed as [7]:

- *Zero Order*: $\frac{dc}{dt} = -k$. In this case, the dissolution rate of a drug is constant, k, and independent of its concentration in the solution, c. The solution to this equation is the linear equation, $c = C_0 - kt$, where C_0 is the concentration at time $t = 0$.

- *First Order*: $\frac{dc}{dt} = -kc$; where the dissolution rate depends linearly on c. The solution can be written as a linear equation in the form $\ln c = \ln C_0 - kt$.

- *Second Order*: $\frac{dc}{dt} = -kc^2$; where the dissolution rate depends on c^2. The solution to the second order release equation can be written as a linear equation in the form $\frac{1}{c} = \frac{1}{C_0} + kt$.

With zero order, or constant rate, delivery systems, a uniform concentration of drug is always available for absorption within a defined therapeutic window [36]. A zero order drug release profile is the primary aim when designing controlled release

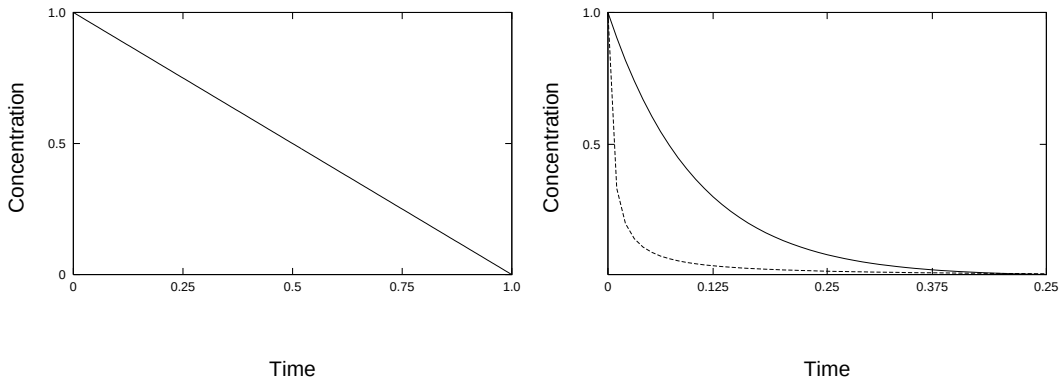

Figure 2.2: (a) Zero, (b) first (solid line) and second (dashed line) order release rates from a tablet with normalised variables.

systems [33]. Surface eroding systems have an advantage in that they can potentially achieve zero order drug release if the surface area of drug does not change during erosion. Surface eroding systems also minimise the risk of *dose dumping* [3]. When surface erosion is the primary mechanism, the drug release rate can be modified with excipients of known dissolution properties. Excipients are generally biologically inert materials that, together with the drug(s), form the delivery system [7]. Tablets, or compacts, often consist of uniform, compressed mixtures of drug and excipient. Recent investigations of dissolution from surface eroding systems has involved considering simple 1- or 2-component cylindrical compacts [12; 21]. These 2-component, or *binary*, compacts consist of equally spaced, alternating layers, of one drug and one excipient [21] (Section 2.1.1). These are referred to in this thesis as *multi-layer* compacts.

Multi-layered Tablets

In pharmaceutics, a multi-layered matrix tablet is a drug delivery device which consists of a matrix core containing the active solute, or the drug, and one or more barrier layers on one or both sides of the tablet [33]. These barriers take the form of *modulating layers* of excipient, formed during tablet manufacture. The modulating

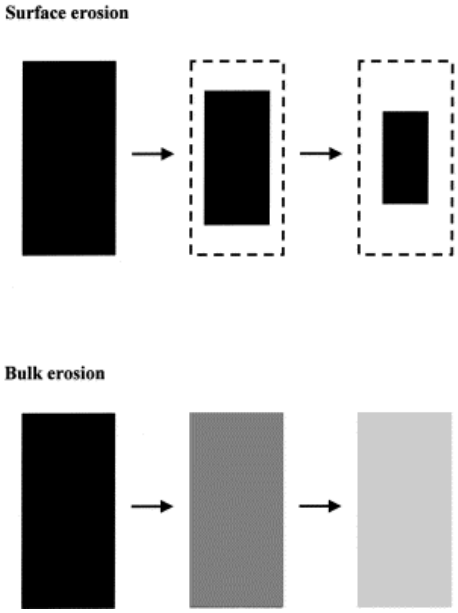

Figure 2.3: The difference between surface and bulk erosion. Black denotes a high concentration of drug. Reprinted from [37], Copyright (2001), with permission from Elsevier.

layers slow the interaction of the drug and the solvent by (i) limiting the surface area of solute exposed to the solvent and (ii) controlling the penetration rate of solvent into the matrix core. Modulation layers extend the time it takes for the drug to dissolve, preventing dose dumping, and lead to linear, or zero-order, dissolution rates [38; 39; 36; 33].

Layered compacts are uncommon in practice, though similar devices have been proposed as viable delivery systems. Conventional matrix tablets containing drugs are generally not zero-order, the release rate falls continuously with time [38]. Although multi-layer systems usually attempt to achieve a zero-order release rate, some multi-layer systems have been designed to achieve bimodal release [38]. *Bimodal release* consists of an initial rapid release of drug followed by a constant release phase and a second period of rapid release [38].

The state of the art in multi-layered tablet design includes zero-order release sustained systems, quick/slow systems, time-programmed systems and bimodal sys-

tems [33]. A 3-layer tablet architecture that achieves near zero-order release is outlined by Qiu et al. [40]. The middle layer contains the active drug. This is sandwiched between water-soluble or water-insoluble barrier layers. *Geomatrix* is a well known patented multi-layer delivery system [41]. Based on work carried out at the University of Pavia in the 1980s, Geomatrix is licensed by SkyePharma and is used by companies including Sanofi-Aventis [42]. Geomatrix is designed to deliver a constant rate of drug when in the stomach and the intestines. In addition to achieving near zero-order performance, multi-layer systems have the advantage of low-cost and ease of manufacture [33].

2.1.2 Dissolution Testing

Dissolution testing has evolved over the past three decades to become a critical component of pharmaceutical R&D and manufacturing [7; 9]. Broadly speaking, there are three main reasons for carrying out dissolution tests: (i) to ensure consistency of output during manufacture, (ii) to assess the factors affecting the bioavailability of the drug and (iii) to make predictions about the performance of the delivery system *in vivo*. It is thus an important test from a clinical perspective [9].

In general, a drug must be in the form of a solution for absorption across the membranes of the gastrointestinal tract into the circulatory system [43; 7]; this means that the design of new formulations and specifications are often guided by *in vitro* dissolution tests which mimic conditions in the GI tract, e.g. USP dissolution apparatus [44; 18]. The effect of changing formulation and manufacturing process variables can be assessed with dissolution testing [7].

In making *in vivo* claims based on *in vitro* data, it is important that an *in vitro in vivo* correlation (or IVIVC) is clearly established [8]. *In vitro in vivo* correlation in this sense refers to the relationship between the *in vitro* dissolution of the drug in the test apparatus and the release or absorption of the drug *in vivo*, in a patient [7]. *In vitro* dissolution tests certainly capture some of the physics of *in vivo* ab-

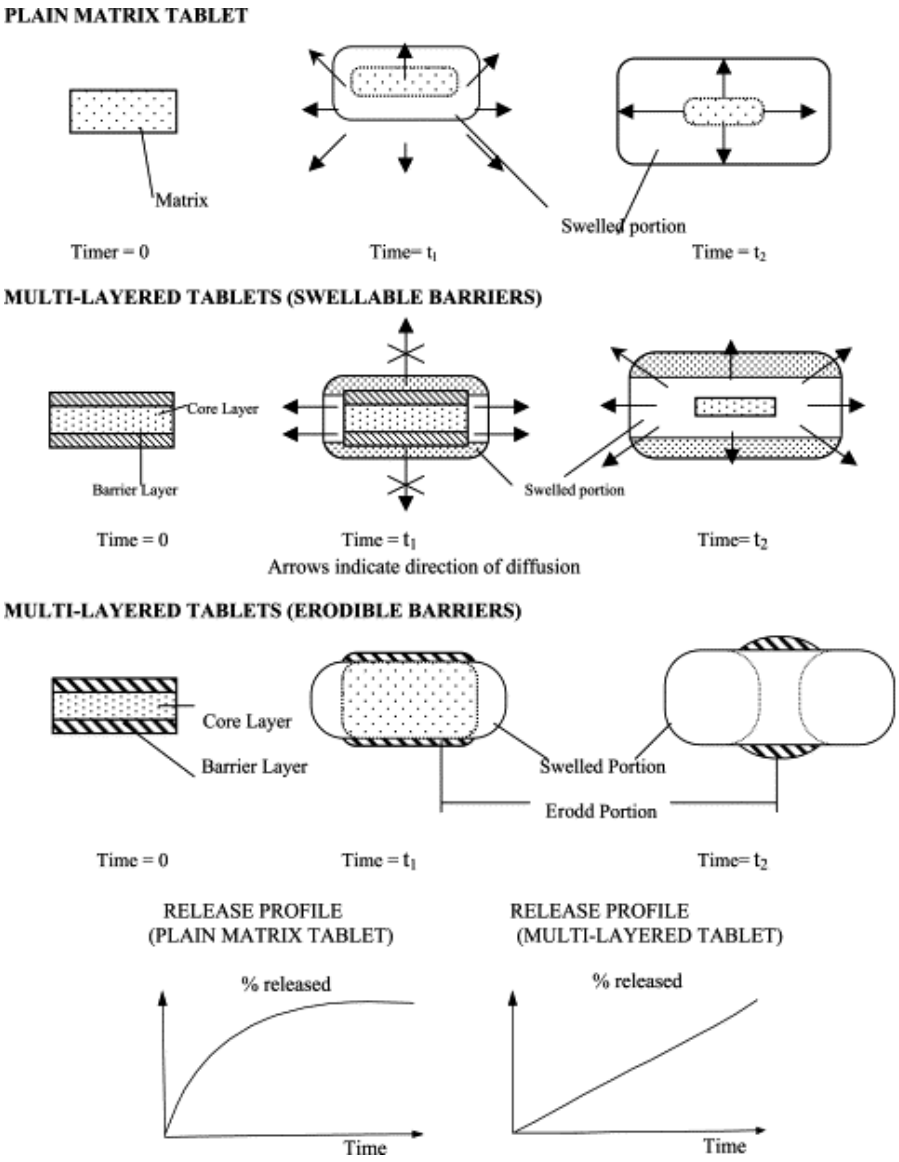

Figure 2.4: Multi-layered matrix tablets. Reprinted from [33], Copyright (2004), with permission from Elsevier.

sorption, in that, for example, the USP defined dissolution apparatus can contain a stirred solution of 0.1M HCl, approximating stomach conditions. Although dissolution tests have developed primarily as manufacturing quality controls and to guide the development of new delivery systems, not as simulations of *in vivo* delivery [7], it is possible to state with confidence that dissolution tests do indicate if the delivery system disintegrates correctly [9]. In addition, the availability of a drug for gastrointestinal absorption from solid dosage forms is often reflected by the *in vitro* dissolution rate [45]. However, dissolution tests can only be used to generate *in vitro /in vivo* correlations (and possibly as *in vivo* surrogates) under strictly defined conditions [8].

Recent analyses of the USP standard dissolution apparatus have indicated intrinsic variability in its operation: the extent to which *in vivo* absorption can be correlated with *in vitro* drug dissolution standard testing devices is not at all certain [15; 18] and it can therefore be difficult to build consistent correlations.

This variability also has serious implications for quality assurance on pharmaceutical production lines. One of the more common dissolution testing devices is the USP Type 2 Paddle Dissolution Apparatus [10], i.e. the USP apparatus referred to throughout this document. This consists of a covered transparent vessel, made of an inert material and filled with a dissolution medium (Figure 2.5). The compact is placed at the bottom of the device. Water is generally used as the dissolution medium but other media may be used as specified by the pharmacopeia, e.g. dilute HCl. The vessel is cylindrical with a hemispherical bottom and a paddle is used to stir the dissolution medium at constant rate as specified by the USP. The temperature inside the vessel is maintained at $37^{\circ} \pm 0.5\ ^{\circ}$ by placing the vessel in a water bath or using a heating jacket.

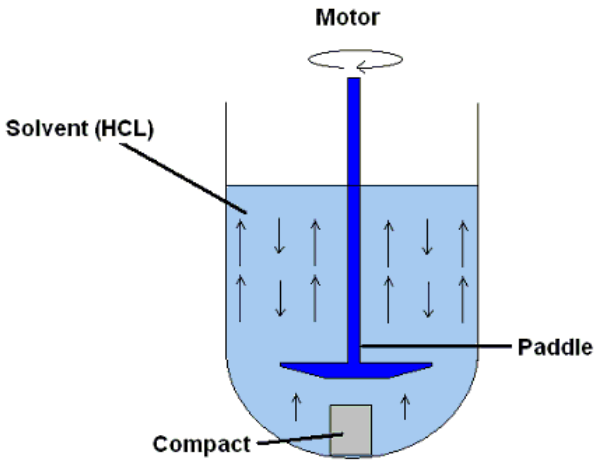

Figure 2.5: Schematic of the USP Type 2 Paddle Dissolution Apparatus.

2.1.3 The Cost of Drug Development

The total costs involved in developing a new drug (or *new chemical entity, NCE*) and its delivery system are significant and continuing to increase. Estimates, corrected for inflation, range from $138 million in 1976 to $802 million in 2003 [46; 47; 48], or even higher [49; 50]. Interpreting these figures is outside the scope of this thesis but it is clear that the major contribution to development costs is the increasingly low probability of success of any one NCE [51; 52; 53]. Only about five in every 10,000 compounds *developed* gets as far as human trials and of those that do, about one in 5 makes it to market as a drug [51; 52; 53]. Thus we can say that in developing NCEs, the pharmaceutical industry is facing significant challenges [54; 5].

As drugs have become more specialised and sophisticated in their therapeutic goals, with personally tailored drugs not far off, their construction, discovery and development have become correspondingly more difficult. Increasingly stringent regulations [55] together with correspondingly sophisticated mandatory clinical trials have increased cost and development time [47; 52] and the risk of failure [54; 56]. In the USA, the average time taken from the start of clinical testing to approval is still more than 7 years and there has been an upward trend in the total development

time from NCE discovery to DDS approval since the 1960s [47]. In 2005, it was between 12 and 15 years [53]. Problems that appear at the end of clinical testing can seriously damage a company's finances [54] [e.g. GTC Biotherapeutics's Atryn and Elan's Tysabri 57; 58; 59; 60].

The increasing financial cost of drug development is a function of (1) technical uncertainty, (2) regulatory uncertainty and (3) market uncertainty [47][2]. The promising NCE must be discovered, understood and developed into an effective DDS, it must be safe and, most importantly, it must be in demand.

Aspects of the pharmaceutical development process are also costed using ethical rather than economic measures. *In vivo* animal trials are presently necessary but undesirable [61] and provoke controversy [62]. There is a consensus that the refinement, reduction and eventual replacement of animals in pharmaceutical research are pursuits of critical importance [63; 64]. Indeed, they are central tenets of the health strand of the EU's Seventh Framework Programme for Research [65].

The priority for modern pharmaceutical companies is therefore to control costs, measured both economically and ethically, while maintaining standards [46; 54].

2.1.4 Simulation and Pharmaceutics

In 1975, Chapman, Mark and Pirtle [66; 67] laid down three practical aspirations for simulation in aerospace, namely to provide flow simulations that are impossible to produce using wind tunnel tests or other experiments, to cut the time and cost of building flow simulations and to provide more accurate flight simulations than wind tunnels can. Since then, the aerospace industry has embraced simulation [68]. Adapting the motivations for adopting computational fluid dynamics [66; 69; 70] to pharmaceutics, we can write that computer simulation: (1) reduces research and development lead-times, (2) can investigate pharmacokinetic mechanisms not easily reproducible in experimental models, (3) can provide more detailed and compre-

[2]In recent years, litigation costs have also added to the overall cost of drug development. The failure of prospective drugs during clinical trials, however, remains the single biggest factor.

hensive information, (4) could reduce all costs and (5) could be more efficient than experimental testing. The use of simulation in drug development has the potential to yield more successful products, fewer failures and faster time to market [6].

Computer simulation may have an impact on all aspects of pharmaceutics, from discovery through to final clinical testing [71]. With the completion of the human genome project and the explosion in bioinformatics technology, the number of molecular targets for drugs is expected to jump from approximately 500, in 2003, to many thousands within a few years; in addition, the analysis of the human genome is expected to eventually speed drug development [72; 4]. With better understanding, the number of drug candidates for a particular target can be optimised *in silico* for high-throughput physical screening. Multivariate statistical computer simulations can help in the design of clinical tests, to predict the results of clinical studies and identify those with a satisfactory probability of success [73]. Simulations of drug delivery devices could predict the effect of changing process or formulation variables on the resulting drug release profile [37; 74].

Although many simulation companies have concentrated efforts on drug *discovery* tools, there are some working on *physiologically based pharmacokinetic* (PBPK) simulation [75; 76; 77]. An example of this is the Israeli firm Optimata which has conducted clinical trials at Nottingham City Hospital in Britain and Soroka Medical Center in Negev of a simulation tool used to optimise therapeutic regimes for cancer patients [78]. Optimata has already successfully modelled protocols for drug delivery in animals [79].

The convergence of computing and engineering capability, the need for pharmaceutical companies to reduce R&D risks, and an acceptance of the interdisciplinary nature of pharmaceutics by pharmacists and biologists are all contributing to the growing importance of simulation [80; 81]. About half of the top 40 pharmaceutical companies are using simulation and modelling tools [4]. According to extrapolated possible scenarios, by 2015 computer modelling and simulation will be core to drug

development [4; 5].

Russell and Burch outlined benchmarks for the ethical, legal and scientific use of animals in research and development, introducing the idea of the 3 Rs: replacement, reduction and refinement [61; 82; 83; 64]. Our understanding of the body at all levels is improving continuously [6]. At one extreme of our understanding are results from the human genome sequencing project [84]. At the other extreme, researchers are constructing models of complete organs [85]. IBM's Blue Gene project has as one of its main objectives the application of Blue Gene's computational resources to significant scientific problems and the project has identified protein folding as its first challenge [86]. The combination of constantly improving theoretical understanding and computing technology is allowing an increasingly large number of processes to be simulated at all levels of biological organisation; this may culminate in models of the human body that, for all required purposes, are *in silico* human systems. At the very least, computer simulation has the potential to reduce the need for experimental testing, both *in vitro* and *in vivo* testing.

2.2 Drug Dissolution Modelling

The theory of dissolution has been studied for over a century and it is a century since it was established that dissolution takes place in two stages [87; 88]. The first is the separation of drug molecules from the surface of the solid to form a solution saturated with drug at the solid-liquid interface. In practice, this is achieved by maintaining the concentration of drug in the solid to be very much higher than the drug solubility [32]. The second stage is the mass transport of the drug from this saturated layer into the bulk solution [88]. This second stage has most influence on the dissolution process. In general, the mass transport is the result of two mechanisms, diffusion and convection, described by the *concentration boundary-layer equations*[3].

[3]The concentration boundary-layer is a thin layer of fluid in the immediate vicinity of a diffusing surface where the concentration gradient normal to the surface is very large [89].

2.2.1 Classical Work

Noyes and Whitney

The original and most famous model was developed over a century ago by Noyes and Whitney [87]. Based on observation of two quite different materials dissolving in distilled water, Noyes and Whitney deduced the general law:

$$\frac{\partial c}{\partial t} = k(C_s - c) \tag{2.1}$$

where C_s is the solubility of the substance, or the concentration of its saturated solution; c is the concentration after a time t, and k is a constant of proportionality. Integrating this equation with appropriate assumptions gives:

$$k = \frac{1}{t} ln \frac{C_s}{(C_s - c)} \tag{2.2}$$

Noyes and Whitney obtained values for the solubility C_s and the concentration c for several values of t. With these values and Equation (2.1), values for the constant k were determined for benzoic acid and lead chloride dissolving in distilled water.

As they revealed, k remains constant for a particular binary system of a solute A and solvent B.

Nernst and Brunner

The work of Noyes and Whitney was later modified by Nernst and Brunner [90; 91]. Nernst and Brunner proposed the two-stage dissolution process that still has currency today [88; 20]. They observed that during dissolution, (i) the layer of solution at the solid-liquid interface reaches saturation concentration almost immediately, after which (ii) diffusion takes place across the diffusion layer. In addition, Nernst and Brunner assumed that the fluid in this diffusion layer was stagnant. Although this model is very useful, later work showed that these assumptions are not necessary

[92]. The processes at the solid-liquid interface do not need to be instantaneous, only rapid relative to the processes in the diffusion layer. In addition, the fluid in the diffusion layer does not need to be stagnant. Under many practical conditions, such as those found in the USP dissolution apparatus, this assumption is unrealistic. The diffusion layer can have both velocity and concentration profiles normal to the surface. This is an expression of the concept of the boundary-layer [93; 89]. Nevertheless, the models of Noyes and Whitney and Nernst and Brunner do yield useful results for *sink* conditions, i.e. if the concentration of the solute never exceeds 10% of C_s [87; 92; 88].

The Noyes-Whitney equation for sink conditions is generally written in the form:

$$\frac{dm}{dt} = \frac{DAC_s}{h} \tag{2.3}$$

where $\frac{dm}{dt}$ is the mass transfer rate, and the constant of proportionality C is replaced with DA where D is the *diffusion coefficient*, generally defined as a quantity having the units $[\mathrm{m}]^2[\mathrm{s}]^{-1}$, h is the effective diffusion layer thickness and A is the surface area available for dissolution [94; 7].

Higuchi

Higuchi's model was developed as part of a study of the dissolution rates of multi-component, or *polyphase*, tablets where the dissolving crystalline components A and B form an intimate, uniform, non-disintegrating mixture and are assumed not to interact with one another [11].

Higuchi observed that, when exposed to a solvent, the dissolution rates of the two components can be described in the initial stages by the Noyes-Whitney model. After a short period of time, however, one of the phases will be depleted *at* the solid-liquid interface. This is because the ratio of the diffusion-controlled dissolution rates of the two components ($D_A C_A^0 / D_B C_B^0$) is not proportional to the ratio of the amount, or mass, of each component (N_A/N_B) originally in the mixture at the

surface, i.e. one component may dissolve faster than the other. D_A and D_B are the dissolution coefficients of A and B in the solvent respectively and C_A^0 and C_B^0 are the solubilities of A and B. After a time t_1, a thin layer extending to just below the surface will consist of only one of the components. Aside from the exceptional critical situation (when $N_A/N_B = D_A C_A^0 / D_B C_B^0$), the thin layer will consist entirely of either A or B after a time t_1; these, Higuchi called situations A and B respectively.

Taking situation A, when the surface is purely made up of component A after a time t_1, Higuchi defines two important positions, S_1 and S_2. S_1 is the solid-liquid interface at the surface, while S_2 is the interface between the bulk solid mixture and the solid phase A layer just inside the surface. $\Delta S = S_2 - S_1$. Since A is at the surface, the dissolution rate of A is given as:

$$G_A = \frac{D_A C_A^0}{h} \tag{2.4}$$

where h is the effective diffusion layer thickness. What Higuchi calls the *mass dissolution rate* G_A, therefore, is in fact the dissolution rate *per unit surface area* or the *mass flux*.

Molecules of B, however, must pass through not only the diffusion layer thickness h, but also through the solid layer of phase A, of thickness ΔS. Higuchi then writes the mass flux of component B from the surface as

$$G_B = \frac{D_B C_B^0}{h + \frac{\tau}{\epsilon}\Delta S} = \frac{N_B}{N_A} G_A \tag{2.5}$$

where τ and ϵ are the *tortuosity* and *porosity* of the solid phase A respectively. The porosity is a measure of how well packed the solid is or how much empty space between component particles exists[4] while the tortuosity is a measure of the increase in distance a diffusing molecule travels due to bending and branching of

[4]In pharmacy, porosity can be defined as a function of the ratio between the apparent and true densities of a tablet, i.e. $\epsilon = 1 - \frac{\epsilon_{\text{apparent}}}{\epsilon_{\text{true}}}$ [95].

pores between voids in the solid components [95; 96][5]. τ and ϵ are usually expressed as dimensionless ratios or percentages [7].

Equations (2.4) and (2.5) are valid for steady-state sink conditions and when no phase B remains in solution within the pores of the thin A phase layer. This is true for most practical situations. These equations, along with similar equations for the reverse situation when A dissolves faster than B, were used by Higuchi to predict the dissolution from discs of benzoic and salicylic acid dissolving in 0.1M HCl. His results matched well for many systems and Higuchi's model is still relevant and useful today.

2.2.2 Contemporary Work

Recent work, carried out with two-component tablets, i.e. consisting of one drug and one excipient, dissolving in the USP apparatus, has shown that the theoretical dissolution rates predicted using Higuchi's model do not always agree well with observed dissolution rates. Researchers, using experiments and computer simulation, have identified three examples of dissolution physics that are not captured by Higuchi's model. These are: (1) pH changes close to the surface of the dissolving tablet [13; 14], (2) the effect of excipient particle size [12; 97; 98], (3) complex hydrodynamics, such as those found in the USP apparatus [15; 16; 17; 18; 19]. The effect of particle size was particularly interesting; large particles of fast-dissolving excipient seem to increase the drug dissolution rate. One explanation is that, once dissolved, large particles leave behind large pores on the compact surface, increasing the effective surface area of drug exposed to the solvent for all values of drug loading. This mechanism is, however, not well understood.

Nevertheless, this explanation suggested theoretical and experimental investigations of how drug and excipient dissolution properties affect the surface area of drug

[5]Tortuosity is normally defined as the ratio of the actual path length through the pores to the Euclidean, or shortest, distance, i.e. $\tau = \frac{E_{\text{actual}}}{E_{\text{Euclid.}}}$. A straight pore has a tortuosity of exactly one, expressed as a ratio [96].

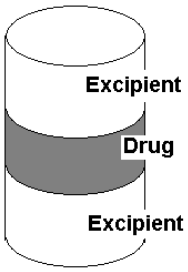

Figure 2.6: An idealised multi-layer compact.

and its delivery rate during dissolution [21]. To this end, recent work has involved modelling simple one or two component cylindrical compacts, dissolving in the USP dissolution apparatus. The two component compacts consist of equally spaced alternating layers of one drug and one excipient. These idealised multi-layer compacts are referred to as simply *multi-layer* compacts in the remainder of this thesis.

Researchers chose the multi-layer configuration for reasons including: (i) it is a simple starting point, with well-defined regions of drug and excipient [21], (ii) techniques used to model this system may be applied to uniformly mixed multi-component compacts [20] and (iii) a multi-layer code had already been written [99].

The PSUDO Project

The PSUDO[6] proof of concept project, initiated in 1998, demonstrated how computer simulation can be used to model compacts dissolving in the USP apparatus [100; 20]. This project followed on from earlier investigations in Trinity College Dublin into the validity of Higuchi's Model [14; 99; 12].

The PSUDO project focused on understanding and modelling multi-component compacts dissolving in the USP apparatus. The numerical code was based on a finite element model [99]. During the course of the project, experiments showed that the hydrodynamic conditions in the device were complex, confirming work from the

[6]Parallel SimUlation of Drug release cOde. Funded by the European Union Fourth Framework Programme for Research. PSUDO was a collaboration between Hitachi, Elan and the Schools of Pharmacy and Mathematics at Trinity.

1990s [14; 12]. The project concluded in 2000 and was considered a qualified success, falling short of its target to fully model two component dissolution but demonstrating reasonable agreement between *in silico* and *in vitro* results for single component compacts and initial multi-component investigations [20]. In the final report, pharmacists from Elan and Trinity noted that experimental and numerical results for a single component were in reasonable agreement but that there was still work to be done for two-component systems and in considering the complicated flow patterns in the USP apparatus [20]. The project concluded with a road-map for future work: to continue the development of the mathematical models (for application to more complicated systems) and to investigate the hydrodynamics of the test apparatus, eventually integrating the dissolution and hydrodynamic models to produce a model of the test apparatus.

The PSUDO Models of Dissolution Kenny's diffusion model, which describes dissolution from a multi-layered surface, forms the basis of the PSUDO code [99]. The surface is exposed to a solvent (which is at rest relative to the surface) and the different layers dissolve at different rates. The resulting one and two-dimensional finite-element code models diffusion from the layers and tracks the new position of the surfaces as they recede. The code was originally intended to model the drug dissolution from stent-based drugs into a patient's bloodstream[7].

A hybrid Galerkin finite-element and finite-difference moving grid scheme were used to estimate the time dependent diffusion from a two-dimensional section of a multi-layered surface, each layer containing a different component. The work is based on a scheme outlined by Vuik and Cuvelier for etching of a printed circuit board [101].

Kenny chose the multi-layered surface to represent a cylindrical medicinal implant consisting of alternating co-axial cylinders of drug and inert polymer. The

[7] A stent is a small cylinder that is inserted into a blood-vessel, often to provide support for the vessel walls and to prevent narrowing, but also often as a DDS.

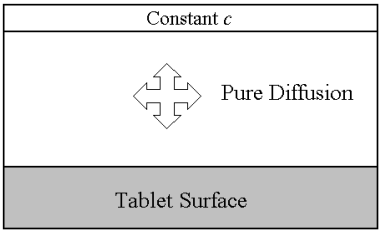

Figure 2.7: A schematic of Kenny's code. The code solves for the situation of pure diffusion in the region next to a dissolving surface.

core code was subsequently successfully adapted by the PSUDO project for diffusion from multi-layer compacts standing vertically in a USP apparatus with the aim of extending the solution to account for advective mass transfer, resulting in a code that captured diffusion, advection and the receding drug/fluid interface [20]. In order to achieve this, additional code was wrapped around the code from Kenny's work. Three different wrappers, or methods, were described and are outlined below.

The first solution outlined involved solving a simplified cylindrical formulation of the advection-diffusion equation [20; 102]

$$\frac{\partial c}{\partial t} = -v_z \frac{\partial c}{\partial z} + D\left(\frac{\partial^2 c}{\partial r^2} + \frac{1}{r}\frac{\partial c}{\partial r} + \frac{\partial^2 c}{\partial z^2}\right) \tag{2.6}$$

where c is the concentration, v_z is the velocity in the z direction, parallel to the surface, D is the dissolution coefficient and r is the displacement in the radial direction, i.e. normal to the surface. It can be read that the change in concentration with time in a given point volume in the fluid is equal to the net amount of material advected into the volume in unit time in the z (streamwise) direction plus the net amount of material diffused into the volume in both directions in unit time. This represents Kenny's original code with a simplified advection term added (see Figures 2.7 and 2.8).

In this instance, the fluid velocity v_z is assumed to be constant at all distances from the surface and mass is only advected parallel to the surface. At every point,

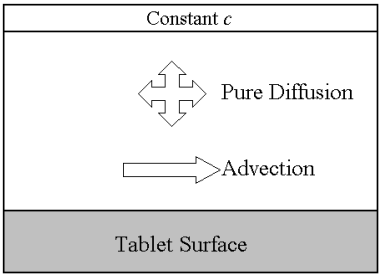

Figure 2.8: A schematic of Method 1 in the PSUDO code. The code solves for the situation of pure diffusion as well as simplified advection in the region next to a dissolving surface.

the change in concentration with time is assumed to consist of the net change in concentration due to diffusion plus the net change in concentration due to advection in the z-direction.

In the second model proposed by the PSUDO team, the problem is simulated as pure diffusion in the region next to the surface (Figure 2.9). To capture advection, a convective boundary condition is used on the boundary between the diffusion layer and the rest of the fluid. The convective boundary condition depends on the free-stream velocity and takes the form

$$D\frac{\partial c}{\partial n}\bigg|_{n=0} = -h_m(C_s - C_{\text{bulk}}) \tag{2.7}$$

where C_{bulk} is the concentration of the drug in the bulk fluid, h_m is the convection mass transfer coefficient and n is the displacement normal to the surface, with the other quantities already defined [20; 102]. As in Method 1, the free-stream velocity v_z is again assumed to be constant and is given as an input.

The mass of drug in the solution at $t = t + \Delta t$ is then calculated using the formula

$$m(t + \Delta t) = m(\Delta t) + \Delta t \int_\Gamma v_n(c - C_{\text{bulk}})d\Gamma + \int_\Omega c d\Omega \tag{2.8}$$

which can be read as the amount of drug in the simulation domain at time $t +$

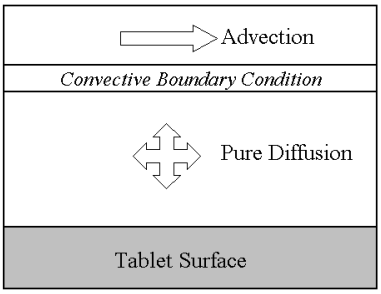

Figure 2.9: A schematic of Method 2 in the PSUDO code. The code solves for the situation of pure diffusion in the region next to a dissolving surface. Advection is captured by imposing a convective boundary condition on the upper boundary of the diffusion layer.

the amount of drug convected across the boundary Γ between the diffusion region and the bulk region + the amount of drug in the diffusion region (Ω). The steps in calculating the mass transfer rate are:

1. Set C_{boundary} = advective boundary condition
2. Run diffusion simulation and calculate flux from surface
3. Assume the advective flux is the same as the surface flux (because of mass continuity)
4. Calculate the amount of mass advected into fluid in Δt
5. Recalculate C_{bulk} and iterate

The third PSUDO method also assumes pure diffusion in the region close to the surface (Figure 2.10). It is assumed that the concentration c at the freestream boundary of this region is equal to c_{bulk}. The increase in mass of drug in the volume outside the layer in unit time is then set equal to

$$m(t + \Delta t) = m(t) + \Delta t \int_{\Gamma} v_z (c - C_{\text{bulk}}) d\Gamma \tag{2.9}$$

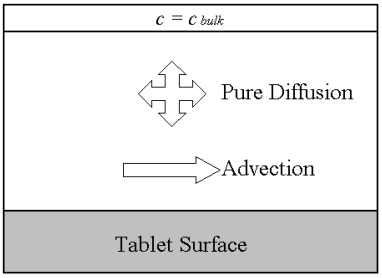

Figure 2.10: A schematic of Method 3 in the PSUDO code. The code solves for the situation of pure diffusion in the region next to a dissolving surface. Advection in this case is captured by imposing the Dirichlet boundary condition $c = c_{\text{bulk}}$ on the upper boundary of the diffusion layer.

$m(t + \Delta t)$ is equal to $m(t)+$ the net amount advected across the boundary Γ between the concentration boundary-layer and the bulk fluid. The advection term is equal to the characteristic time-step multiplied by the net flux of additional mass from the surface in time Δt.

C_{bulk} at t_0 is set to zero. After the characteristic time-step Δt, the amount of drug advected in that time is calculated. This is then the mass of drug in the system at $t_0 + \Delta t$, $m(t_0 + \Delta t)$. By dividing by the total volume this gives a new value for $C_{\text{bulk}}(t_0 + \Delta t)$ which then becomes the new boundary condition. The calculation steps are:

1. Set $c_{\text{boundary}} = C_{\text{bulk}}$
2. Run diffusion simulation and calculate flux from surface
3. Assume the advective flux is the same by considering mass continuity
4. Calculate the amount of mass advected into fluid in Δt
5. Recalculate C_{bulk} and iterate

The PSUDO team identified the use of dimensional variables when solving the governing equations as a source of error [20]. There are about six orders of magnitude between values for diffusivity and fluid velocity, a fact that could lead to instabilities

when fine grids or time-steps are used. Other problems included difficulty with the definition of boundary conditions, such as how to impose fixed conditions and how to implement moving boundary conditions, e.g. setting the bulk concentration. A new analysis carried out for this thesis, considering the effect of fluid velocity on the overall error, is presented in the Results and Discussion Section.

Outcomes of the Project Papers, based on work carried out during the PSUDO project, were subsequently published in two distinct tracks. These tracks have proceeded in parallel, but with collaboration, over the past five years.

Following on and adding to the work of experimenters in the 1990s, the PSUDO project prompted an investigation into the hydrodynamics of the USP apparatus [17]. Although the dissolution test is widely used, high variability in results have been reported and its fluid dynamics are for the most part not well understood [15]. Dissolution test failures have led to many product recalls and inconsistencies and variability in test results are a significant problem[8] [18]. The dissolution test *is* a highly variable technique; the major sources of variability are the geometric parameters of the device and the stirring mechanism, both leading to complex hydrodynamics [15]. Surface imperfections in the vessel can also lead to variability in the results [103].

Contemporary computational fluid dynamics (CFD) simulations [104; 105; 44; 16; 18; 19] have shown that the flow field in the device is fully three-dimensional and that small displacements of the compact can lead to significant changes in the dissolution rate of the dosage form. Increasing the stirring speed of the dissolution apparatus to about 200 rpm results in a higher, non-linear, drug release rate [98]. These studies strengthen the argument that it is the intrinsically complex hydrodynamics of the device that cause most of the variability in dissolution test results [18].

[8] 16 % of non-manufacturing recalls of solid oral dosage forms in the period 2000-02 were due to test failures .

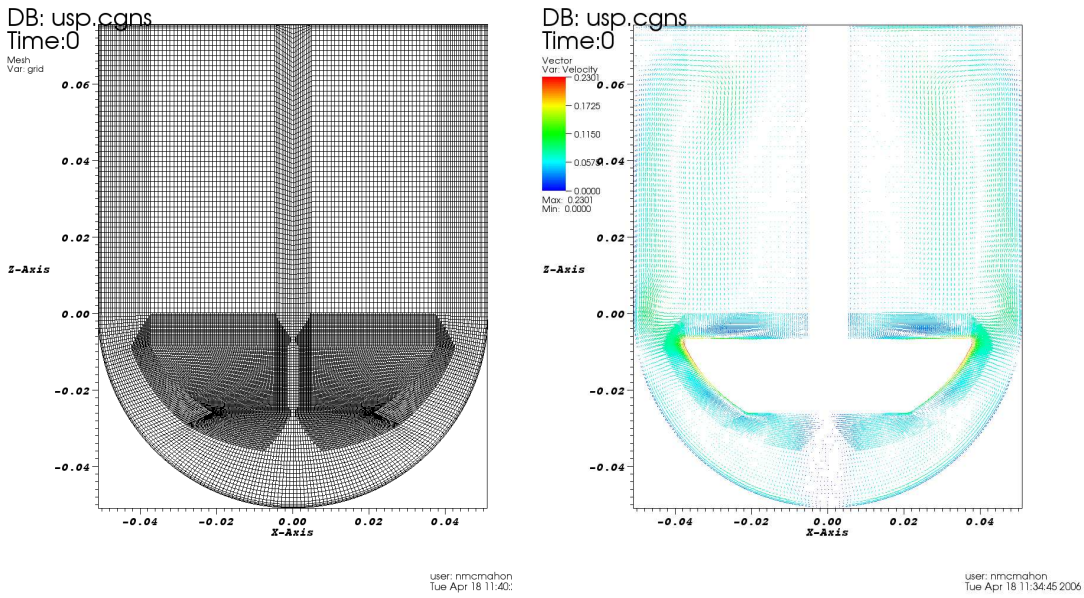

Figure 2.11: Section from the 3D USP hydrodynamic simulation built by [19] using the commercial code Fluent. The computational mesh is shown on the left with computed velocity magnitudes on the right.

Accepting, then, that much of the variability in results is attributable to the complex and heterogenous hydrodynamics of the device, an important question is raised: to what extent are these complex hydrodynamics a function of factors that we can control, and to what extent are they intrinsic to the design of the USP apparatus [17]? Two research teams have worked in the area of USP hydrodynamics over the past number of years. Healy, McCarthy, Corrigan, D'Arcy and others, following on from the PSUDO project, have built Fluent[9] CFD simulations of the USP apparatus, investigating the sensitivity of the results to the location of the compact in the device [104], comparing the simulated flow of the bulk fluid with laser doppler measurements [105], examining the flow patterns next to a compact placed centrally at the bottom of the device [44] and the dissolution from compacts at various positions on the bottom of the device [19]. Kukura, Baxter, Muzzio and others have completed simulations and experimental studies similar to those of

[9]The commercial computational fluid dynamics code [106].

Healy et al [e.g. 104]. These include studies of the hydrodynamics and shear within the device [16] and the variability of dissolution with position in the device [18]. All these studies conclude that the complex heterogeneous hydrodynamic environment within the USP apparatus leads to the observed variability in the test and that the hydrodynamics are intrinsic to the design of the USP Type 2 Dissolution Apparatus.

The second track, indicated by PSUDO, involves improving the analytical and numerical models of mass transfer [e.g. 21; 17]. The work presented in this thesis follows on from this track. As outlined in Chapter 1, the questions that are raised include: how can we build on this work and improve our understanding of tablet dissolution in the USP apparatus? Can we generalise the analytical solution described by Crane et al. [21]? Can we determine the validity of this analytical solution? Can we build a better numerical solution? Can we say anything about the end phase of tablet dissolution?

Crane, Hurley et al.

As one of the publications generated by the PSUDO project, Hurley and Crane present analytical and numerical solutions for the mass transfer from simple 1-layer tablets consisting entirely of either benzoic acid or salycilic acid (1-layer systems)[17]. Both models give reasonable agreement with experimental results [104]. The first is a semi-analytical model for a 1-layer compact consisting of only one substance (Figure 3.1). This model is based on the work of, among others, Lévêque [107] and Kestin and Persen [108], and is expressed by the equation:

$$\dot{m} = 4.26aD(C_s - c_\infty)\sqrt{\frac{U_0 L}{\nu}} S_c{}^{\frac{1}{3}} \left[1 + 0.42\frac{L}{a}\sqrt{\frac{\nu}{U_0 L}}\right] \tag{2.10}$$

where $\dot{m}$ is the mass transfer rate, a is the radius of the tablet, D is the diffusivity of the drug, C_s is the solubility of the drug in the fluid (solvent), c_∞ is the concentration of drug in the solvent far from the surface, U_0 is the freestream fluid velocity parallel to the surface, L is the length of the tablet, S_c is the Schmidt

Number[10] of the flow and ν is the kinematic viscosity of the fluid. The system state variables are assumed to remain constant.

An important feature of this analytical solution is its correction for the finite curvature of the tablet, using the variables suggested by Seban and Bond [109]. This is captured by the term in square brackets. If the correction for the curvature of the compact is dropped, the solution coincides with that of Kestin and Persen [108].

A Galerkin finite element solution to the problem is also presented. This numerical implementation is based on the work carried out during the PSUDO projects for the dissolution of multi-layer tablets over time [20]. The system is modelled by observing that a solution to the concentration boundary-layer equations can be closely approximated by splitting the system into two distinct sub-systems: (i) a thin region close to the surface in which only diffusion from the surface takes place, and (ii) an outer, bulk, region where advection dominates and mixing takes place. The Galerkin finite-element scheme described in this paper is then used to simulate the diffusion layer only. A suitable boundary condition at the interface between these two regions depends implicitly on the average mainstream fluid velocity, as with the third PSUDO model, and some characteristic, known, *mixing time*, T.

T can be related to v_z by assuming that drug released from the compact will become fully mixed when it has been carried throughout the dissolution apparatus by the upwards advection current [20]. If the apparatus has a fluid depth of L cm, a particle of drug will be carried from the bottom to the top of the apparatus in $T = L{v_z}^{-1}$ s. For the particular vessel considered by the project, and for an estimated average v_z of 1.2 cm s^{-1}, T is calculated to be 10.5 s.

The authors conclude by stating clearly the two recommendations for building improved models that came out of the PSUDO project: (i) to incorporate the three dimensional fluid motion of the USP apparatus, and (ii) to develop the analytical

[10]The Schmidt number is defined as the ratio of kinematic viscosity to diffusivity, i.e. $Sc = \frac{\nu}{D}$.

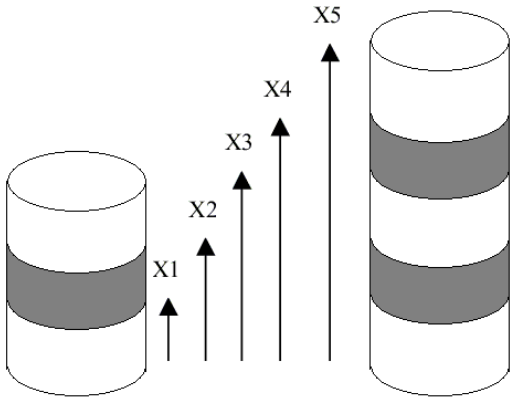

Figure 2.12: A schematic of 3- and 5-layer compacts with key streamwise x positions indicated.

model to take account of the compact's finite size and its curvature as it dissolves.

In a more recent paper, Crane et al. [21] outline an improved semi-analytical model, derived using a simpler method and agreeing to within 5% of the previous analytical result [21]. Importantly, despite neglecting the axial curvature and finite volume of the compact, this model has a significant advantage in that it tackles the surface boundary conditions necessary to model multi-layer (as opposed to single-layer) compacts. As in previous work [i.e. 20; 17], the problem is simplified to that of seeking a solution to the concentration boundary-layer equation on a flat surface consisting of alternating diffusing and non-diffusing regions. They assume a *Pohlhausen*-type trigonometric representation of the concentration profile $\frac{c}{C_s} = 1 - sin\left(\frac{\pi}{2}\frac{y}{\delta_c}\right)$, where c is the concentration of drug in the fluid, C_s is the solubility of the drug, y is the normal displacement from the surface and δ_c is the concentration layer thickness. Mass transfer rates, computed using this improved model, agree quite well with experimental data for 1-, 3- and 5-layer systems.

For the 5-layer case, the derivative surface boundary condition between x_2 and x_3 (Figure 2.12) is implemented by observing that, for a steady state, the total amount of drug in the solution at x_3 must be the same as the total amount of drug in the solution upstream at x_2 [21]. The authors assume, in addition to the assumptions

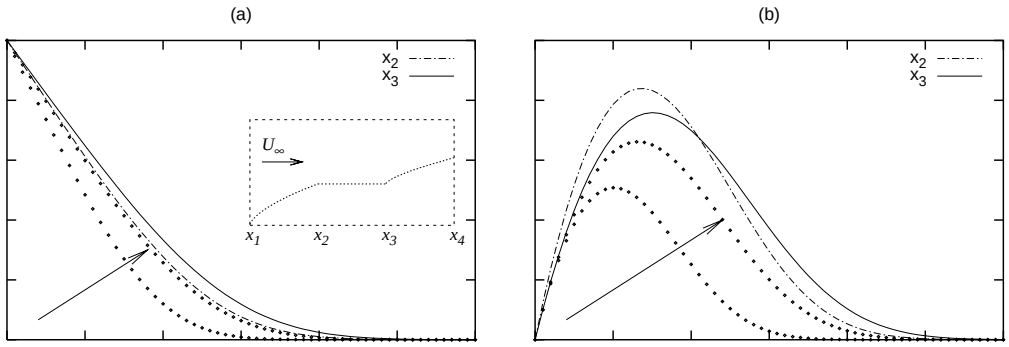

Figure 2.13: (a) Inset: the variation of drug content in the solution with x-position; (a) The concentration curve at x_3 is varied by increasing δ_{c_3} until (b) the areas under the *uc* curves at x_2 and x_3 are the same. The amount of drug in the solution is a function of this area.

previously outlined, that the *shape* of the concentration-distance curves at x_2 and x_3 are the same and, importantly, that δ_{c_3}, the concentration boundary-layer thickness at x_3, is the only quantity that can be varied to maintain the mass balance between x_2 and x_3 (Figure 2.13).

These additional assumptions allow the two separate layers of drug to be treated as one continuous layer and lead to an expression for the total mass transfer from a 5-layer compact

$$\dot{m} \;=\; \left[2\pi a(0.332U_0)\sqrt{\frac{U_0}{\nu}}C_s\alpha\right](2K)^{\frac{2}{3}}\left(x_4^{\frac{3}{4}} - \; x_3^{\frac{3}{4}} + x_2^{\frac{3}{4}} - \; x_1^{\frac{3}{4}}\right)^{\frac{2}{3}} \tag{2.11}$$

where $\dot{m}$ is the mass transfer rate, a is the radius of the compact, ν is the kinematic viscosity of the solvent, α is a constant equal to $\left(\frac{1}{2} - \frac{4}{\pi^2}\right)$ and

$$K = \frac{D\pi\nu^{\frac{1}{2}}}{2\alpha 0.332U_0^{\frac{3}{2}}} \tag{2.12}$$

with notation as described previously.

Barat, Ruskin and Crane

Following the PSUDO project, and in parallel with the work presented in this thesis, Barat et al. investigated the use of direct *Monte Carlo* (MC) integration techniques[11], together with cellular automata (CA) to model the dissolution of drug from a two-component matrix tablet [112; 113].

The aim of these studies was to explore (i) the advantages of using modern probabilistic methods to simulate drug dissolution and (ii) how these methods can complement conventional applied mathematical and numerical approaches.

As a starting point, the team used experimental data for matrix tablets consisting of ibuprofen and a wide range of acidic excipients. As outlined earlier, the dissolution of the acidic excipients and the resulting change in pH of the dissolution medium close to the surface is reported to have the effect of suppressing the dissolution of the ibuprofen [12]. A two-dimensional *lattice* or cellular-automata grid was used to represent the tablet and this was coupled with a Monte Carlo algorithm which determined the diffusion and advection of the tablet components into the dissolution medium (Figure 2.14).

The two-dimensional lattice represents a longitudinal slice through the centre of the tablet, with solvent flowing from bottom to top. The state of each cell, or *site*, in the lattice, $\psi(i, j)$, was initialised to be one of the following types: (i) a site containing drug particles only, (ii) a diffusing site containing drug particles at the solid-liquid interface, (iii) a site containing excipient particles only, (iv) a diffusing site containing excipient particles at the solid-liquid interface, (v) a site within the concentration boundary-layer containing only solution, (vi) a site within

[11]Monte Carlo methods are a family of techniques which balance the probability of finding the actual solution with the probability of finding a solution in a specified time [110]. In essence, MC methods amount to the direct calculation of the integrals involved in *canonical averages* [110]. The scientific method for the study of a physical system can be considered to consist of three stages [111], (1) identifying the smallest number of model parameters which can practically describe the system, (2) discovering the physical laws governing the system and which allow us to predict the future values of key parameters, (3) using physical measurements to infer the actual values of the model parameters. This last stage is deductive; logic and probability theory can be applied [111]. This is the purpose of *inverse* MC methods.

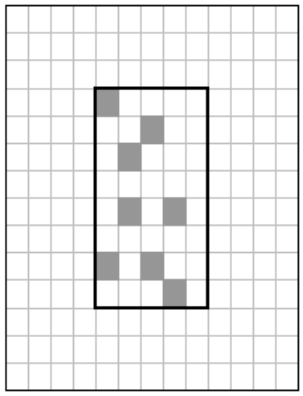

Figure 2.14: A cellular automata lattice, similar to the one used by Barat, Ruskin and Crane with a two-dimensional representation of drug dispersed in a matrix tablet.

the concentration boundary-layer containing diffusing particles, (vii) a site in the bulk fluid, outside the concentration boundary-layer.

The sites within the tablet were randomly initialised to consist of either drug or excipient while maintaining the overall pre-defined proportion of drug to excipient. Sites at solid-liquid interfaces, between the solid and the concentration boundary-layer, were designated as diffusing sites. Since the drug and excipient have, in general, different solubilities, or rates of dissolution in the dissolution medium, a different number of particles will move from a drug site to a solution site than from an excipient site to a solution site [c.f. 11]. This is also true of the movement of drug and excipient particles between solution sites, i.e. between sites within the concentration boundary-layer. The solubilities also impose an upper limit on the number of particles of drug and excipient that can occupy a particular site at a particular time.

In the case of a drug, particles are allowed to move from one site to another through consideration of two concentration gradient dependent probabilities. The first depends on the drug concentration in the target solution site and the other depends on the sum of the excipient concentrations in the n solution sites surrounding

the starting site.

Diffusion was modelled by using these probabilities to calculate the number of drug particles that will move to each of the adjacent solution sites. The number of excipient particles moving from one site to another is defined in terms of a variable that takes a value between 1 and M, where M represents the number of drug particles already present in the solution site.

The probability that particles will move, together with the maximum number of particles that the adjacent site can accommodate, were used to give the number of particles that actually move. The number of particles at each site is then summed to arrive at new concentration levels after each time-step. The total number of particles is not constant, as any particles that exit from the concentration boundary-layer into the bulk fluid are discarded, advected out of the computational domain.

This advection process is implemented using the Pohlhausen concentration boundary-layer profile described by Crane et al. [21]. All sites within the defined concentration boundary-layer, i.e. between the surface, $y = 0$, and $y = \delta_c$[12], have a maximum concentration which is defined by the Pohlhausen curve. If any cells have more than this number of particles, the excess particles are *advected* away.

Between time-steps, the state of each site is also updated according to set rules, e.g. if a site consisting only of drug is adjacent to a boundary-layer site at $t = 0$, then this becomes a site within the concentration boundary-layer containing diffusing particles at $t = 1$.

This model responds well to changes in drug and excipient solubilities, with behaviour qualitatively similar to the results of experimentation [12; 113]. The second paper by Barat et al. also presents investigations of the effect of drug loading and initial porosity and cellular-automata behaviour on the simulation [113].

[12] δ_c is the concentration boundary-layer thickness.

2.3 Heat Transfer

2.3.1 Applying Heat Transfer Solutions to Mass Transfer Problems

Many textbooks and papers contain solutions to problems in heat transfer and specifically the thermal boundary-layer equations [e.g. 94; 114; 102]. The mechanisms of heat and mass transfer are mathematically equivalent and thermal solutions can be applied with some minor modifications to problems in mass transfer [94].

As discussed by Crank [94], many technical workers experience difficulty in translating solutions of the heat transfer equations to mass transfer. Following Crank's discussion, we take the example of two simple geometrically similar 1-dimensional heat and mass diffusion systems with constant properties, briefly discussing the correspondence between the physical equations, parameters, variables and boundary conditions.

After Kestin and Persen [108], the thermal boundary-layer or thermal energy equation can be written as

$$u\frac{\partial T}{\partial x} + v\frac{\partial T}{\partial y} = \alpha_T \frac{\partial^2 T}{\partial y^2} \tag{2.13}$$

for all cases of sub-sonic or low speed fluid flow. The equivalent mass transfer equation is

$$u\frac{\partial c_A}{\partial x} + v\frac{\partial c_A}{\partial y} = D_{AB} \frac{\partial^2 c_A}{\partial y^2} \tag{2.14}$$

where α_T is the thermal diffusivity and D_{AB} is the mass diffusivity, defined previously. Diffusivities link fluxes with gradients. For low speed flows with constant properties, the correspondence between the thermal and mass transfer equations (Equations (2.13) and (2.14)) is clear.

As discussed by Crank [94], we identify the temperature T with concentration c. The thermal diffusivity α_T is identified with the mass diffusivity D_{AB}.

2.3.2 Classical Work

Lévêque

Lévêque was the first to observe that when the transition from surface to freestream temperature takes place across a very thin region close to the surface, the most important fluid velocities, those inside this very thin region, change linearly with normal distance from the surface, i.e. $u = \beta y$, where β is the normal velocity gradient, the *wall tangent*, and x and y are the streamwise and normal directions respectively (Figure 2.15)[107]. Schuh showed how to apply this idea to boundary-layers, with the modification that the normal velocity gradient is a function of x, $u = \beta(x)y$ [115; 116]. Kestin and Persen [108] came to this idea independently, outlining with clarity the solution that Schlichting describes in Boundary-Layer Theory [117]. This solution, of the thermal boundary-layer equation for flows of large Pr[13], is Kestin and Persen's, not Lévêque's. Kestin and Persen's simplifications work for large Pr or in any situation when the momentum boundary-layer thickness is much greater than the thermal boundary-layer thickness. Perhaps surprisingly, $u = \beta(x)y$ results in a very good approximation, even for low Pr numbers, so that only liquid metals with Pr much less than 1 cannot be treated this way [118].

In summary, **Lévêque** proposed that $u = \beta y$. **Schuh** extended Lévêque's observation with $u = \beta(x)y$ and a thermal boundary-layer solution for high Pr flow with a wall temperature that varies as a fixed power of x. **Kestin and Persen**, like Schuh, found an approximation of the form $u = \beta(x)y$ and arrived at the thermal boundary-layer solution presented by Schlichting [107].

Kestin and Persen

Kestin and Persen's paper [108] describes solutions for heat transfer when the thermal boundary-layer is contained entirely within the momentum boundary-layer, for

[13] Pr, the *Prandtl* number is the ratio of the momentum and mass diffusivities, i.e. $\frac{\nu}{\alpha}$.

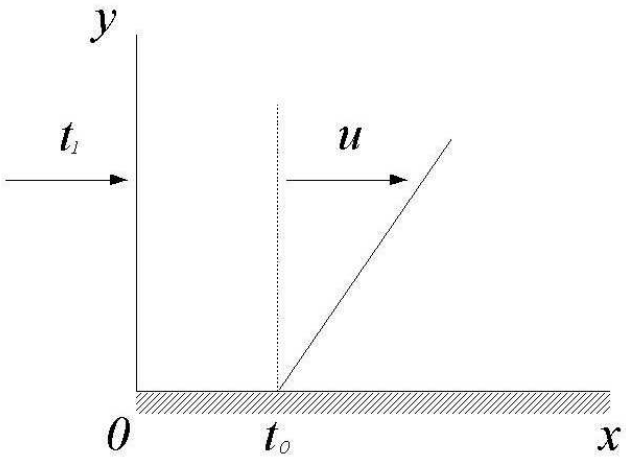

Figure 2.15: Lévêque's linear velocity approximation. Quantities as defined in the text.

various wall temperature distributions. For the problem of a flat plate with a temperature jump at $x = x_0$, they propose a substitution that reduces the parabolic thermal boundary-layer equation (Equation (2.13)) to an ordinary differential equation. The solution to this equation, the temperature at any point in the fluid, can be expressed as an incomplete gamma function. With the modifications outlined above, this thermal solution can be adapted for application to the mathematically equivalent problem of mass transfer from a flat plate. The resulting solution is

$$c = 1 - \frac{1}{\Gamma\left(\frac{1}{3}\right)} \int_0^{\eta^3} e^{-t} t^{-\frac{2}{3}} dt \tag{2.15}$$

where c is the concentration of solute at x and y, $\Gamma\left(1/3\right) \approx 2.68$ [119], $t = \eta^3$ and η is given as

$$\eta = \frac{y\sqrt{\frac{\tau_0}{\mu}}}{\left[9a \int_{x_0}^{x} \sqrt{\frac{\tau_0}{\mu}} dx\right]^{\frac{1}{3}}} \tag{2.16}$$

2.4 Numerical Methods

2.4.1 Finite Difference Methods

Introduction

As discussed by Dehghan [120], the main point of finite difference methods is to obtain a solution to a PDE of a function by approximating the derivatives in the equation using only values of the function at discrete points in space and time. Taylor series expansions are most often used to obtain these approximations. It is possible to classify Taylor series by their theoretical order of accuracy, allowing the performance of different finite difference methods in terms of accuracy to be easily compared. The *modified equivalent partial differential equation method* is a formal methodology used for simple and direct comparison of finite difference schemes and to identify and generate the most efficient schemes [121; 120; 122; 123].

There are three methods for approximating a continuous derivative using points on a finite difference grid : forward or upwind differencing, backward or downwind differencing and central differencing [121; 114]. When a PDE is discretised using these methods, its derivatives at a point are calculated in terms of a combination of the values of nearby nodes. For a given x, y position, forward differencing uses function values at the previous x step on the grid, $i - 1$, to approximate derivatives in y. Backward differencing uses function values at the next x step, $i + 1$, to approximate derivatives in y. Central differencing at a grid position i, j uses function values at the current i position to approximate derivatives in y. The use of forward or backward differencing introduces a second order error termed *numerical dispersion* or *numerical diffusion* which acts as an additional artificial diffusion or viscosity term [121].

Artificial or *numerical* diffusion is an effect of solving continuous equations (including the Navier-Stokes equations and the boundary-layer equations) discretely on a fixed grid. Numerical diffusion is a smoothing of gradients that affects ad-

vected fluid properties, including momentum and other scalar quantities [124]. It results from the spatial averaging that occurs between grid points. More specifically, the approximation of the differential equations with discrete equations introduces a truncation error[14] which includes numerical diffusion as a component [125]. In general, the discrete equations are more diffusive than the original differential equations and so the discrete solution differs from the continuous solution. Numerical codes are usually chosen so as to avoid numerical diffusion (especially when modelling shock waves and similar phenomena which involve steep gradients), but in some cases numerical diffusion helps to reduce problematic effects, such as singularities; when viscous (physical) diffusion is not enough to ensure a stable solution, numerical diffusion can be used as a stabilising measure [126]. The *effective viscosity* is a combination of both viscous and numerical diffusion [126]. The quantification of the effects of numerical diffusion, especially when physical viscosity plays a major role is important, such as in boundary-layer flows and mixing problems [126]. Numerical diffusion was quantified as a second-order error term (by Lantz and Chaudhari, both in 1971) through the examination of a simple Taylor series expansion of the original fluid property around a point, e.g. concentration, $c(y)$. The modified partial differential equation method, developed by Warming and Hyett, is a popular method used to investigate the stability and accuracy of linear partial differential equations [127]. A truncated version of the modified equation can be used to gain insight into the nature of both dissipative and dispersive errors, a method used by Dehghan in his review of various finite difference codes [120]. Dehghan's modified version of the one-dimensional advection-diffusion equation, $\frac{\partial c}{\partial t} + u\frac{\partial c}{\partial x} - \mu\frac{\partial^2 c}{\partial x^2}$, is $\frac{\partial c}{\partial t} + u\frac{\partial c}{\partial x} - \mu\frac{\partial^2 c}{\partial x^2} = \frac{u\Delta x}{2}(\omega - \lambda)\frac{\partial^2 c}{\partial x^2} - \frac{u\Delta x^2}{6}(2\lambda^2 - 3\omega\lambda + 1 - 6k)\frac{\partial^3 c}{\partial x^3} + O[\Delta x^3]$, where w is a weight which controls the upwind bias, λ is the Courant number, $\lambda = u\Delta t/\Delta x$, and k is the dimensionless diffusion number, $k = \mu\Delta t/\Delta x^2$. The right hand side of this equation represents the truncation error. The first term, the

[14] See Section 2.4.1.

lowest order term, contains the numerical diffusion component. As detailed by Dehghan, the modified version of the Crank-Nicolson scheme used in this thesis does not contain numerical diffusion [120].

Finite difference methods are straightforward and well suited to problems involving regularly shaped regions or regions that can be transformed into regular regions [121].

Explicit and Implicit Schemes

Finite-difference schemes can be *explicit* or *implicit* [114; 121] (Figure 2.4.1). An explicit scheme is one where the downstream variables, $u(x + \Delta x, y)$, $v(x + \Delta x, y)$, depend only on upstream values $u(x, y)$, $v(x, y)$. An implicit method, on the other hand, is one where $u(x + \Delta x, y)$ and $v(x + \Delta x, y)$ depend also on u and v values at the same x-step and where $u(x + \Delta x, y)$ and $v(x + \Delta x, y)$ must be solved simultaneously with all u,v values at $x + \Delta x$. Although explicit schemes are susceptible to instability and errors can propagate rapidly if Δx is too big (see Figure 2.4.1), they are attractive for their simplicity. Maintaining solution stability by keeping Δx small, however, can lead to excessive computation. Implicit schemes, although more computationally intensive per step, are generally unconditionally stable and allow large Δx, subject only to truncation errors [114]. In addition to having generally better accuracy, implicit methods can be more efficient overall [121]. Understanding when an implicit scheme ought to be used instead of an explicit scheme is therefore an important study.

There are many examples of both explicit and implicit finite difference schemes, all fit for different purposes and many texts and papers have been written on the subject [e.g. 128; 121; 120]).

(a) (b)

Figure 2.16: In explicit schemes (a) small errors can rapidly propagate, rendering the solution useless. Implicit schemes (b) on the other hand, damp out errors, preventing them from saturating the calculation. This diagram is for illustration only.

Finite Difference Schemes

Dehghan's recent collection of papers on the subject of finite difference methods [e.g. 120; 122; 123; 129] provides a comprehensive overview of the strengths and weaknesses of different explicit and implicit finite difference schemes when used to solve variations of the advection-diffusion equation (see Table 2.1 and Figure 2.18). Overviews of the advantages and disadvantages of various finite difference schemes are also given by [130; 131; 128; 121; 94; 114; 102]. These methods include the Forward Time Centred Space (FTCS) explicit method, the upwind explicit method, the Lax-Wendroff explicit method, the Crank-Nicolson semi-implicit method, the Backward Time Centred Space (BTCS) implicit method, the upwind or backwards implicit method, the Siemieniuch Gladwell implicit method, the Richtmyer modification or backward differentiation implicit method, the Dufort-Frankel (or FQEFD, Fast Quasi-Explicit Finite Difference) explicit method [121], the Hopscotch explicit method, the Alternating Direction Implicit (ADI) method and the Strongly Implicit Procedure (SIP) among others. Several common schemes are outlined in Figure 2.17. Finite difference schemes are relatively simple, yet effective and widely used to solve diffusion problems [e.g. 132].

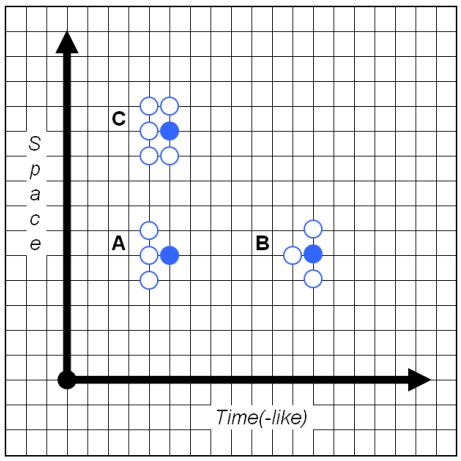

Figure 2.17: Three finite difference schemes: (A) Forward Time Centre Space (FTCS) explicit scheme. The quantity of interest (at the blue dot) is calculated using known information from the previous time-step, (B) Backward Time Centre Space (BTCS) implicit scheme. The quantity of interest is calculated using known information from the previous time-step as well as unknown information at the current time-step, (C) Crank-Nicolson (semi-)implicit scheme. The quantity of interest is calculated using known information from the previous time-step as well as information at the current time-step.

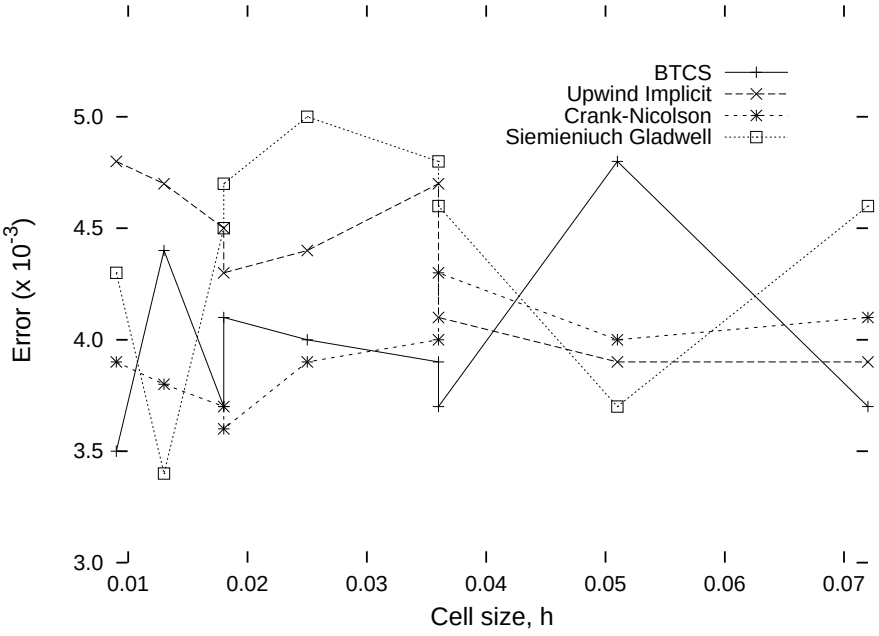

Figure 2.18: From [120], the Crank-Nicolson scheme provides the consistently lowest error for a range of cell sizes h.

Δt	Δx	h	Error ($\times 10^{-3}$) BTCS Type	Upwind Implicit	Crank-Nicolson Type	Siemieniuch Gladwell
0.004	0.02	0.009	3.5	4.8	3.9	4.3
0.008	0.02	0.013	4.4	4.7	3.8	3.4
0.016	0.02	0.018	3.7	4.5	3.7	4.5
0.008	0.04	0.018	4.1	4.3	3.6	4.7
0.016	0.04	0.025	4.0	4.4	3.9	5.0
0.032	0.04	0.036	3.9	4.7	4.0	4.8
0.016	0.08	0.036	3.7	4.1	4.3	4.6
0.032	0.08	0.051	4.8	3.9	4.0	3.7
0.064	0.08	0.072	3.7	3.9	4.1	4.6
		Average	**4.0**	**4.4**	**3.9**	**4.4**

Table 2.1: A comparison of the results of several finite-difference schemes with the analytical solution of a specific instance of the advection-diffusion equation [120]. The Crank-Nicolson scheme provides the consistently lowest error for a range of cell sizes h.

Stability and Accuracy

The small errors, of interest to us, that can give rise to instabilities are caused by (i) truncation and (ii) round-off errors. Other sources of error include among others (iii) incomplete convergence of solutions and (iv) mistakes in the input data [131].

Finite-difference approximations to derivatives are generally produced using truncated Taylor series. The *truncation* error associated with a finite-difference scheme is due to the neglected higher-order terms in the series approximation of a derivative. As more of the higher order terms are included in the approximation, the truncation error should decrease and the scheme is said to be compatible with the partial differential equation it solves [94]. In addition, as the grid cell size Δh decreases, the truncation error should also decrease. In this case the scheme is said to converge on the solution [94]. In practice, however, the higher order terms in the Taylor series are unknown and there are limitations on how small Δh can be. As Δh decreases, the computation required becomes excessive and the effect of *round-off* error begins

to become important. Round-off error is a result of the representation to a finite number of decimal places of irrational numbers. As $\Delta h \rightarrow 0$, the difference between variable values at adjacent grid points becomes very small and the finite difference representation of derivatives results in one small value (i.e. Δh) being divided into another small value and the potential for significant losses due to round-off error increases. As the number of grid points increases with decreasing Δh, the effect of round-off errors can accumulate rapidly leading to *unstable* behaviour, i.e. the *total* error becomes significant. The total error is a combination of truncation and round-off errors. The best balance between error and computational performance is generally found through trial and error [131].

Stability is concerned with situations where the build-up of the total error causes the finite-difference solution to deviate significantly, and often catastrophically for the computer program, from the actual solution of the underlying PDE [94]. In a *stable* solution, the effect of rounding errors is negligible while the opposite is true of an unstable solution. Error estimates are more often conservative, over-estimating the effect of numerical errors on the solution.

Procedures for investigating the stability of a model are formalised in the subject of code verification.

Stating the order of accuracy based on a Taylor series expansion is the conventional measure of a numerical scheme's formal accuracy in computational fluid dynamics and applied mathematics literature. Schemes should generally be at least *second order accurate* in space [133]. Essentially, if the concentration at h is treated as a continuous function $c(y)$, it can be written as a Taylor expansion of the form [134]

$$c(h) = c(0) + h(\partial c/\partial y)_{y=0} + (h^2/2!)(\partial^2 c/\partial y^2)_{y=0} + ... \tag{2.17}$$

Where h is an interval in the y-direction, normal to the surface. By neglecting terms containing derivatives of exponent 2 and higher, we can write $c(h) =$

$c(0) + h(\partial c/\partial y)_{y=0}$. This truncated Taylor expansion approximation to $c(h)$ has a truncation error of at most $O(h)$ using Landau's notation [135][15], the contributions from all the terms containing derivatives of exponent two and higher sum to a term of order h, at most. It is first order accurate. By re-arranging this expression in terms of $(\partial c/\partial y)_{y=0}$, we can write

$$\left.\frac{\partial c}{\partial y}\right|_{y=0} = \frac{c(h) - c(0)}{h} + O(h) \tag{2.18}$$

Similarly, through simple rearrangements and retaining the term containing the second order derivative in Equation (2.17), we can write down an expression for $(\partial c/\partial y)_{y=0}$ that has a truncation error of order h^2, $O(h^2)$.

When we state that the derivative (Neumann) boundary condition and numerical scheme are second order accurate in space, what we mean is that the maximum error in our approximation of the concentration at a point is at most of the order of $(\Delta y)^2$ where Δy is the grid step-size normal to the surface.

The second order three-point approximation, outlined above, is the most appropriate finite difference approximation to the concentration gradient at the surface [136; 134].

Boundary Conditions

There are several possible boundary conditions that can be imposed at the boundaries or surfaces of systems involving both thermal and mass transfer [94; 102]. These are: (i) Dirichlet, or first order, conditions where the temperature or mass concentration at a boundary or surface is explicitly defined, e.g. $T = 0$ or $c = 0$, or (ii) some form of Neumann boundary condition, where are temperature or concentration gradient is defined at the surface, i.e. $\dfrac{\partial T}{\partial x}$ or $\dfrac{\partial c}{\partial x}$ are known. Neumann, or second order, conditions include situations where the heat flux across the boundary is known or is zero (in the case of a thermally insulated or impermeable surface).

[15] Knuth's article provides a definitive discussion of O, Ω and Θ [135].

When the heat or mass flux is known, it may take the form of a *radiation* boundary condition. This is when the flux is proportional to the difference between the temperatures at the surface and in the medium far from the surface. A convective boundary condition is similar to a radiation boundary condition except that the flux at the surface is not only related to the difference in temperatures or concentrations between the surface and far-field, but also on the flow velocity of the fluid. Other types of Neumann condition are described in textbooks [e.g. 94; 114; 102].

The derivative boundary conditions are implemented as forward-difference second order, 3-point approximations, namely [136]

$$\frac{\partial c}{\partial y} = \frac{-c_2 + 4c_1 - 3c_0}{2\Delta y} = 0 \tag{2.19}$$

$$\Rightarrow c_0 = \frac{4c_1 - c_2}{3} \tag{2.20}$$

where c_0 is the unknown concentration value at the surface at grid position i, while c_1 and c_2 are the concentration values at Δy and $2\Delta y$ from the surface respectively, also calculated at i. The error associated with this boundary condition, based on a Taylor series expansion, is of the order of at most $(\Delta y)^2$ [134].

Solution of Linear Systems of Equations

The Tridiagonal Matrix Algorithm (TDMA), or Thomas Algorithm, is a computationally efficient technique for solving tridiagonal linear simultaneous equations [121]. According to [137], it was first proposed by [138] and subsequently applied to systems of parabolic equations by [139]. The technique described [137] is a simplified version of the Gaussian elimination method that works for tridiagonal matrices (see also [140], [141], [114], and [131]).

2.4.2 Verification and Validation

Uncertainty is the estimated percentage by which an observation or calculation differs from reality [142]. Uncertainty can be classified into three broad sub-categories: (1) uncertainty in the input data, boundary conditions and so forth; (2) uncertainty in the model used and (3) uncertainty arising from numerical error. Uncertainty ultimately results from a lack of information [143][16]. Numerical simulation hinges on the assumption that as the grid size $h \rightarrow 0$, the numerical solution converges to the continuum differential equation and the exact solution [142]. The objective of verification and validation is to demonstrate that this assumption is true for each implementation. Verification is about *solving the equations correctly* and validation is about *solving the correct model equations with the correct methods* [142]. Stated simply, verification is about mathematics while validation is about physics [145].

Verification

Verification, taken as being synonymous with *code verification*, is concerned with ensuring that the numerical methods chosen solve the chosen equations correctly, to within an acceptable accuracy [146; 147; 145; 143; 68; 148]. Celik's [149] methodology for estimating and reporting the discretisation error of a numerical scheme[17] is important and worth reviewing. The key points are (i) that the computer code must be referenced and previous verification studies relating to it must be described, (ii) the theoretical or formal order of accuracy of the numerical scheme in each di-

[16] The Journal of Fluids Engineering acknowledges that there is no standard method for evaluating the uncertainty in numerical simulation [144]. It does, however, outline criteria to be considered for publication in the journal. These include: (1) precise description of the numerical method including a formal assessment of the truncation error introduced by individual terms in the governing equations; (2) the numerical method must be at least formally second-order accurate in space (based on a Taylor series expansion) for nodes in the interior of the grid; (3) solutions over a range of significantly different grid resolutions should be presented to demonstrate grid independence or grid-convergent results; (4) boundary and initial condition implementations must be clearly described; (5) while the numerical method must be carefully described, all pertinent references must be cited within the paper to allow proper evaluation of the code; (6) comparison to appropriate analytical benchmark solutions may be used to demonstrate accuracy under certain conditions; (7) comparison with reliable experimental results is appropriate, provided experimental uncertainty is established.

[17] Adopted as a requirement for submitted work by the J. Fluid. Eng. [144].

mension for each equation solved must be stated, (iii) for iterative schemes, there should be at least a three orders of magnitude decrease in the normalised residuals for each equation solved, (iv) for time dependent schemes, the convergence of the solution at each time-step should be checked and (v) a variation of the Richardson Extrapolation (RE) method [150; 151], known as the Grid Convergence Index (GCI) method [149; 152], is recommended for assessing the discretisation error. *Systematic grid refinements* using variations of the RE method are the most common way of estimating the actual discretisation error associated with a simulation [142]. An implementation of the GCI method is outlined in the next chapter.

Validation

Validation is the comparison of computational results with experiment [142; 153]. The difficulty with validation, however, is determining (i) how exactly to validate and (ii) what we can say about the correspondence of our model's predictions with reality once a validation procedure has been completed. Oberkampf and Trucano tackle the second point by observing that validation says nothing about prediction, only about the correspondence of model results for known situations [153]. Validation equips us to *infer* how the model will perform in situations for which it has not been validated [153]. The first point can be captured by asking three questions: (1) how can a validation be expressed quantitatively? (2) Can we develop a useful methodology for determining what validation is required? (3) What are the important features of a validation experiment? The authors proceed to define six guidelines for carrying out validations of simulations. These are, essentially, that validation experiments should: (i) be defined by a team comprising experimentalists, modellers, coders, and users; (ii) capture the essential physics of the system under investigation; (iii) attempt to emphasise the complementarity of simulation and physical experiment; (iv) maintain independence between data acquisition from simulation and physical experiment; (v) proceed from simple to complex and from

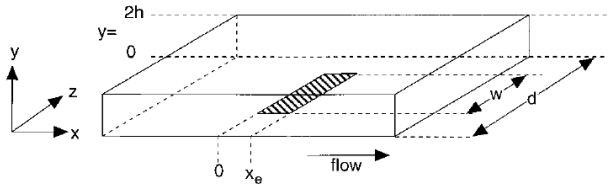

Figure 2.19: A standard channel electrode. Reprinted from [158], Copyright (1998), with permission from Elsevier.

general processes to specific processes; (vi) control experimental error.

2.5 Additional Studies Related to Surface Electrodes

2.5.1 Microelectrodes and the Drug Dissolution Problem

A review of the literature on the stability and accuracy of finite difference schemes [e.g. 149; 144; 133; 145; 153; 154; 134; 155; 156; 157] included a paper discussing the accuracy of numerical solutions in the simulation of diffusion processes at the surface of electrodes and microelectrodes [136]. This problem, of diffusion to electrodes, is very similar to the problem of mass transfer from multi-layer compacts. Much work on this problem has been completed [e.g. 136; 132; 158].

Microelectrodes can be used for many purposes [159; 136; 132], including the study of electrode kinetics, and for use in electrochemical measurement devices or electroanalysis. Microelectrodes of different configurations are often embedded in the walls of chemical reactors and are used to probe the electro-kinetics (electron transfers) of fast chemical reactions [160].

Hydrodynamic voltammetry is a technique used to make very sensitive measurements of electochemical reactions; a microband electrode positioned flush with the wall in a rectangular duct, in contact with a fast-moving flow of electrolyte, can measure electrochemical events over a time-scale of the order of nanoseconds [161] (Figure 2.19). This configuration is generally known as a channel electrode. Channel electrodes have many uses and advantages over other electrode configurations,

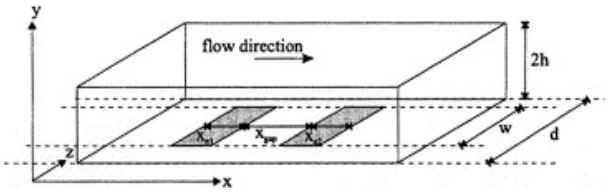

Figure 2.20: Two microband electrodes positioned in a channel flow. Reprinted from [132], Copyright (2005), with permission from Elsevier.

including increased sensitivity and range of measurement [141; 158].

A recent paper describes a problem very similar to that of drug dissolution from multi-layer compacts, the diffusion to two microband electrodes in a channel flow (Figure 2.20) [132]. Studies have shown that this double-electrode configuration allows experimental access to additional mechanistic information about the electrochemical processes [141]. Instead of electrodes and insulators, however, we have diffusing regions of drug and impermeable surfaces. The mathematical descriptions almost coincide.

As with our problem, the diffusion process is described by a simplified version of the time-dependent advection-diffusion equation, which is written as

$$\frac{\partial c}{\partial t} + u\frac{\partial c}{\partial x} + v\frac{\partial c}{\partial y} = D\frac{\partial^2 c}{\partial y^2} \tag{2.21}$$

where c is the concentration of the *electroactive* species, x and y are the streamwise and normal directions, as usual, and u and v are their corresponding velocity components. D $[m^2 s^{-1}]$ is the diffusion coefficient of the process. In addition, it is assumed that mass transfer is dominated by convection in the axial, x, direction and diffusion in the normal, y-direction [162]. In a recent paper [132], the Lévêque approximation to the velocity profile close to the electrode surfaces is given as

$$u(y) = u_0\left(1 - \frac{(h-y)^2}{h^2}\right) \tag{2.22}$$

where u_0 is the velocity at the centre of the channel, y the distance normal to

the surface, and h is the half-height of the channel. An implicit finite difference solution to Equation (2.21) is implemented [163; 164; 165].

2.5.2 Singularities in the Numerical Solutions

A significant portion of the microelectrode literature is given to the consideration of singularities in the numerical solutions. Standard numerical methods (such as finite difference schemes) can have poor accuracy when used to model the mass transfer to electrodes, especially close to the edge of the electrode, where it meets the surrounding insulator [136]. This is mainly due to the presence of a boundary singularity at the interface between the two surfaces. The singularity normally takes the form of a discontinuity in the first derivative of the concentration values at the point where the electrode meets the insulator [136]; two conflicting boundary conditions are imposed on the same point, a Dirichlet condition on the electrode surface and a Neumann (derivative) condition at the insulator surface [159]. Lines of constant concentration are parallel to the surface close to the electrode surface, where the Dirichlet condition is imposed, and perpendicular to the surface of the insulator where the zero-flux Neumann condition pertains. At the interface between the electrode and the insulator, these conditions cause a discontinuity in the normal derivative of concentration and lead to a singular solution to the local current density at the edge of the electrode.

This can be stated as follows - for a disk-shaped electrode in a steady state, where r and z represent the radial and axial spatial coordinates respectively and c is the normalised concentration in the electrolyte, mass transport to the electrode can be described by the steady-state two-dimensional cylindrical diffusion equation [166; 136; 167]:

$$\frac{\partial^2 c}{\partial r^2} + \frac{1}{r}\frac{\partial c}{\partial r} + \frac{\partial^2 c}{\partial z^2} = 0 \tag{2.23}$$

with the following boundary conditions

(1)	$z = 0$	$r > a$	$\dfrac{\partial c}{\partial z} = 0$
(2)	$z = 0$	$r \leq a$	$u = 0$
(3)	$z = 0$	$r = 0$	$\dfrac{\partial c}{\partial r} = 0$
(4)	$z \to \infty$	$r \geq 0$	$c = 1$
(5)	$z = 0$	$r \to \infty$	$c = 1$

where a is the radius of the circular insulator. A singularity then arises at $r = a$, $z = 0$, where boundary conditions (1) and (2) are inconsistent.

Although, as Gavaghan [168; 136] notes, this is a well known problem [169; 170; 171; 94], there is no consensus in the literature about the seriousness of the effect of this boundary singularity on the accuracy of solutions to related problems. Fox and Sankar [171] state that for some elliptic problems, the presence of a discontinuity may not be serious since the solution remains *well behaved* in the solution region and most of the error is confined to the neighbourhood of the singularity. At sufficient distances from the singularity, the numerical results are still accurate. For the diffusion equation, difference solutions quickly approach the analytical solution after a few time-steps [94]. This is true of the steady-state advection-diffusion equation with the streamwise step instead of time-steps. Surveying recent mathematical investigations of the mass transfer to electrodes, [134; 172; 173; 141; 174; 164; 165; 155; 160; 161; 175; 176; 132], the authors make no mention of the boundary singularity as being important to the accuracy of their solutions. Gavaghan [136], however, argues that an accurate solution to this problem is only possible if special techniques are used to handle the singularity; [168], [166], [128], [136], [177], [159], [178], [179] [167] consider the effect of the boundary singularity on the current flux values.

In his PhD thesis, Alden reviews the problem of boundary singularities in electrochemistry and lists the two main examples: the spatial discontinuity that occurs at the boundary between an electrode and an insulator, and the temporal discontinuity that occurs when the electrode potential is stepped [121]. In both situations,

the current flux tends to infinity at a point. Alden [121] describes three methods for dealing with boundary singularities (as outlined by [168; 180; 136; 178; 179]). These are to: (1) increase the mesh density close to the singularity or across the whole computational region, limiting the extent to which the errors can spread (for example [159; 181]), (2) subtract the effects of the singularity by compensating for it [180], (3) use a conformal mapping to transform the computational region, eliminating the singularity altogether (for example [173]).

Modelling diffusion to and from these microband electrodes has many similarities to the work presented in the first study of this thesis, i.e. there are similar system configurations and governing equations. Indeed, the original drug delivery problem tackled by Kenny [99] owed much to earlier work on mass transfer to and from microband electrodes [101]. The mathematical and numerical challenges facing workers in this area are similar to the challenges facing those modelling mass transfer in pharmaceutical devices and the volume of work already completed in modelling electrodes serves to underscore how much there is to be done in modelling drug dissolution.

2.6 Software

2.6.1 Commercial Code

Fluent

The Fluent solver is a C-based computer program for modelling fluid flow and heat transfer involving three-dimensional complex geometries [106]. It uses a finite volume method to solve the Navier-Stokes equations and includes several turbulence models. The finite volume method is commonly used to solve partial differential equations by calculating the value of a conserved variable averaged across a volume. The solver allows the user to set a range of parameters, including specification of the boundary conditions, the material properties and the type of flow model. Gambit is

a pre-processor for CFD analysis, bundled with the Fluent solver [106]. Gambit is used to build model geometries and generate meshes. It can also import, modify and mesh geometries created by third-party computer aided design or computer aided engineering packages. Boundary conditions are then specified and the resulting mesh file exported to the solver.

2.6.2 Open Code

Python

Python is a general purpose, object-oriented, open-source, interpreted programming language. Since the 1990s, Python has grown in popularity and is now used by hundreds of thousands of programmers in fields as diverse as bioinformatics and computer-generated imagery [182; 183; 184]. Python was designed to appeal to Unix/C programmers and to be reusable and readable with minimal coding time [185]. It tends to be used mainly by engineers and scientists.

Python is a scripting language. Advantages of scripting include typeless datatypes to simplify interaction between components and to accelerate application build times [186]. Python has operating system interfaces, a large standard library, and is extensible in C and C++. Other advantages of Python include its wide range of features (datatypes, modules), stability, syntax, small core and modules, widely available documentation, and the available support. It is also free [187; 183]. Python has a large number of libraries including NumPy, its extensive numerical library. Application development is generally faster with Python than with C or Fortran and takes less code to express an algorithm. It is modular and easily extendible. It can be used interactively like MATLAB. Python can also be used to glue existing C/C++ etc. modules together. Python's popularity means that tools exist for many applications where C and Fortran dominate, e.g. a Python binding exists for the *CGNS*[18] (the other CGNS bindings are for C, C++ and Fortran77/Fortran90)[188].

[18]Computational Fluid Dynamics General Notation System.

Python is available for almost every platform including Windows, Linux/Unix, Mac OS X, OS/2, Amiga, Palm OS, WinCE, Java and .NET. It may also run on other system configurations once there is a C compiler available.

Gnuplot

One visualisation tool used to produce many of the graphs in this thesis is Gnuplot. Originally developed in 1986, Gnuplot is a free, command-driven interactive plotting program; it is a powerful tool for plotting mathematical functions and numerical data [189; 190]. Gnuplot is extremely robust and can produce graphs in several formats, including even plaintext [191]. In addition to its interactive functions, Gnuplot can be used in batch mode with text scripts saved as *plot* (.plt) files. Batch mode is particularly useful when producing many similar graphs from a series of experiments [192]. Gnuplot is available for most operating systems.

2.7 Chapter Summary and Conclusions

This chapter began with a review of the drug industry and explained with examples why simulation is important for pharmaceutics. The ideas in this thesis draw most heavily on the results of the PSUDO project. This project and other important contributions to the development of mathematical simulation of multi-layered systems were reviewed. Some of the key ideas discovered in the course of researching this work were discussed and placed in context. Finite-difference schemes and related numerical methods, together with the importance of verification and validation, were introduced. The work reviewed in this chapter forms the basis for much of the further development presented in this thesis and leads on to the related studies which are described in Chapters 4 and 5.

Chapter 3

Theory and Methods, Study 1

This chapter introduces the theory and methods associated with the core investigation of the initial drug dissolution rate from a cylindrical tablet in the USP apparatus. The aim of this work was to make progress in understanding drug dissolution in the USP apparatus; to investigate different problems inspired by aspects of tablet dissolution in the USP apparatus and to build several components of a complete model. The individual investigations each contribute to the argument that simulation is useful for pharmaceutics. Central to this thesis was an investigation of the tablet's initial dissolution rate. This involved the development of a robust finite-difference solution and a study of the differences between existing solutions and a new numerical solution. This first study was followed by a second in which the flow about a cylinder in cross-flow was considered, with a specific investigation of the flow around a meteorological mast. This has utility for the wind energy industry. The third and final part of the thesis was a study of particle dissolution in the USP apparatus. Theory and methods related to the first investigation follow.

3.1 Motivations for Modelling Multi-Layered Tablets

As with previous work, the multi-layer configuration was chosen as the topic for this study for reasons including: (i) it is a simple starting point, with well-defined regions of drug and excipient [21], (ii) techniques used to model this system may be applied to uniformly mixed multi-component compacts [20].

3.2 Model Set-Up

The drug component was taken to be benzoic acid with a diffusion coefficient of 1.236×10^{-5} cm^2 s^{-1} and a solubility in the solvent (0.1M HCl at 37^o) of 4.55 mg cm^{-3} [104]. The viscosity of the fluid was assumed to be that of the solvent, 0.0078$\dot{6}$ cm^2 s^{-1} . The axial freestream velocity past the compact was set as 1.83 cm s^{-1} [17]. The compacts were 0.85 cm in height and of radius $a = 0.65$ cm. Quantity values are detailed in Tables 3.1, 3.2 and 3.3. Experiments, used to validate the results presented in this thesis, were carried out for compacts consisting of [17]:

1. A single layer of benzoic acid (BA).
2. A 3-layer system of benzoic acid and salicylic acid (SA): BA/SA/BA.
3. A 5-layer system of benzoic acid and salicylic acid (SA): BA/SA/BA/SA/BA.

Quantity	**Symbol**	**Value**	
Solubility	C_s	4.55	mg cm^{-3}
Diffusivity	D	1.236×10^{-5}	cm^2 s^{-1}
Schmidt Number	S_c	637	

Table 3.1: Important quantities for benzoic acid systems.

Quantity	**Symbol**	**Value**	
Solubility	C_s	2.58×10^{-3}	mg cm^{-3}
Diffusivity	D	1.13167×10^{-5}	cm^2 s^{-1}
Schmidt Number	S_c	695	

Table 3.2: Important quantities for salicylic acid systems.

Quantity	**Symbol**	**Value**	
Advection Velocity	U_∞	1.83	cm s^{-1}
Kinematic Viscosity (HCl)	ν	$0.00786\dot{}$	cm^2 s^{-1}
Tablet Length	L	0.85	cm
Tablet Radius	a	0.65	cm

Table 3.3: Important quantities common to all systems considered. Kinematic viscosity is given for 0.1M HCl at 37°C.

3.3 Governing Equations

The two-dimensional velocity and concentration boundary-layer equations for steady, incompressible, viscous flow are central to this thesis and their solution forms the basis of much of the work described. We show how the general form of the convection transfer, or boundary-layer, equations can be simplified for the problem under consideration in this thesis.

3.3.1 Boundary-Layer Equations

The Navier-Stokes equations for two-dimensional incompressible flow with constant material properties are [102]

$$\rho\left(u\frac{\partial u}{\partial x} + v\frac{\partial u}{\partial y}\right) = \rho X - \frac{\partial p}{\partial x} + \mu\Delta u \tag{3.1}$$

$$\rho\left(u\frac{\partial v}{\partial x}+v\frac{\partial v}{\partial y}\right)=\rho Y-\frac{\partial p}{\partial y}+\mu\Delta v \tag{3.2}$$

where ρ is the density of the fluid, assumed constant, μ is the viscosity, u and v are the velocity components in the streamwise (x) and normal (y) directions respectively, X and Y are components of the resultant mass force vector $\tilde{K}$, p is the fluid pressure, and $\Delta=\left(\frac{\partial^2}{\partial x^2}+\frac{\partial^2}{\partial y^2}\right)$. The mass continuity equation is

$$\frac{\partial u}{\partial x}+\frac{\partial v}{\partial y}=0 \tag{3.3}$$

with the variables just defined. Simplified from the Navier-Stokes equations, the *advection-diffusion equation* is used to model the drug mass transfer from the surface of the compacts. In its general two-dimensional form, this is written

$$\frac{\partial c}{\partial t}+u\frac{\partial c}{\partial x}+v\frac{\partial c}{\partial y}=\frac{\partial}{\partial x}\left(D_{AB}\frac{\partial c}{\partial x}\right)+\frac{\partial}{\partial y}\left(D_{AB}\frac{\partial c}{\partial y}\right)+\dot{n}_A \tag{3.4}$$

where c is the concentration of drug, D_{AB} is its concentration-independent diffusion coefficient and $\dot{n}_A$ is the net rate increase of concentration as a result of chemical reaction. Derivations of this equation, arrived at by physical considerations, can be found in textbooks [e.g. 193; 102].

Simplifications

For the problem under consideration, we can make significant simplifications to the convection transfer equations. We assume saturation concentration, C_s, at the solid-liquid interface. This is achieved by ensuring that the concentration of drug in the tablet is very much higher than the drug solubility in the liquid solvent; as long as drug is available, this will maintain the concentration of drug as C_s at the dissolution front and the release rate from the surface will be constant [32]. In addition, if the Schmidt number (S_c, defined in a footnote in the last chapter) is large, the surface curvature may be neglected and the problem reduces to steady two-dimensional

dissolution from a flat plate (see Figure 3.1). In liquids, the mass diffusion process is very slow, whereas momentum diffusion due to collisions is relatively large. A large Sc number reflects this. Consequently, the momentum boundary-layer is much thicker than the concentration boundary-layer, implying that the thickness of the concentration boundary-layer is small with respect to the radius of the tablet [21]. Since we assume a steady, axial free-stream velocity and the flux of drug is constant across the solid-liquid interface, the problem reduces to a two-dimensional steady-state and we can write $\frac{\partial c}{\partial t} = 0$ (see also [21] for an order of magnitude analysis). Given that the dimensions of the dissolution apparatus are large compared with the dimensions of the tablet, it is assumed that sink conditions pertain, i.e. the concentration of the solute in the bulk dissolution medium never exceeds 10% of C_s [87; 92; 88].

Also, since the concentration boundary-layer is thin with respect to the momentum boundary-layer, it is sufficient to replace the axial velocity profile u by its tangent at the surface [108] so that

$$u = \frac{\tau_0}{\mu} y \tag{3.5}$$

where τ_0 is the shear stress at the surface and μ is the viscosity of the fluid. The diffusion term in the x-direction may be neglected as for sufficiently fast flows the convection term masks the streamwise diffusion.

Surface erosion is assumed to be the primary release mechanism [37]; this is supported by the linearity of the release rate data from experiments carried out on similar tablets [194; 104]. In addition, we assume that there are no chemical reactions and we neglect the effects of pH changes. We also assume that all material properties are constant, in particular the solubility of the drug and excipient [102]. We also assume that the dissolution medium is isotropic [94].

With these assumptions and simplifications, the velocity boundary-layer equations can be written [89; 195] :

$$u\frac{\partial u}{\partial x} + v\frac{\partial u}{\partial y} = \nu\frac{\partial^2 u}{\partial y^2} \tag{3.6}$$

$$\frac{\partial u}{\partial x} + \frac{\partial v}{\partial y} = 0 \tag{3.7}$$

While the concentration boundary-layer equation, Equation (3.4), can be written in its simplified form as

$$u\frac{\partial c}{\partial x} + v\frac{\partial c}{\partial y} = D\frac{\partial^2 c}{\partial y^2} \tag{3.8}$$

The boundary-layer equations are second order, linear, homogeneous and parabolic as opposed to the Navier-Stokes equations which are elliptic [131; 130]. The simplified thermal and concentration boundary-layer equations are characterised by advection terms on the left-hand side and a diffusion term on the right-hand side. These equations describe low-speed forced convection flows.

Non-Dimensional Form

We take the concentration boundary-layer equation. The dimensionless parameters x' and y' are defined as

$$x' = \frac{x}{L} \quad \text{and} \quad y' = \frac{y}{L}$$

Where L is some *characteristic length* of the system of interest. For a flat plate, for example, this would usually be the length of the plate, while for a cylinder, the characteristic length is normally taken as its diameter. The velocity components u and v can be non-dimensionalised by defining

$$u' = \frac{u}{U} \quad \text{and} \quad v' = \frac{v}{U}$$

Where U is the free-stream fluid velocity. Finally, concentration can be non-dimensionalised by writing

$$c' = \frac{c - C_s}{C_\infty - C_s}$$

Substituting these expressions into the simplified concentration boundary-layer equation, Equation (3.8), yields the dimensionless concentration boundary-layer equation, which we can write

$$u' \frac{\partial c'}{\partial x'} + v' \frac{\partial c'}{\partial y'} = \frac{D}{UL} \frac{\partial^2 c'}{\partial y'^2} \tag{3.9}$$

with the boundary conditions $c'|_{y=0} = 0$, $c'|_{y=\infty} = 0$. The equation can also be written in terms of the dimensionless Re and Sc numbers,

$$u' \frac{\partial c'}{\partial x'} + v' \frac{\partial c'}{\partial y'} = \frac{1}{Re_L Sc} \frac{\partial^2 c'}{\partial y'^2} \tag{3.10}$$

where Re_L is the Reynolds number associated with the characteristic length L[1]. Writing the boundary-layer equations and the associated boundary conditions in a dimensionless form is the most efficient and useful presentation, allowing us to see the important parameters in their correct context [114]. Dimensionless equations allow us to apply the results for one particular system to another system that is geometrically similar [102].

3.3.2 Boundary and Initial Conditions

We are concerned only with the drug mass transfer rate and assume no interaction between the two components, so the boundary conditions are

[1]See the Glossary for a brief discussion of this important parameter.

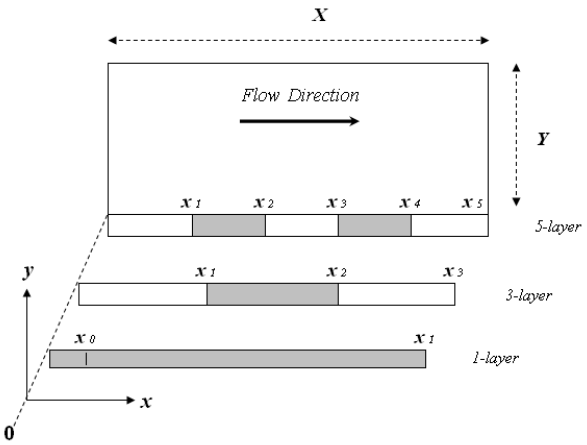

Figure 3.1: 1-/3-/5-layer configurations. The dimensions and coordinate system used to describe the computational domain are highlighted. The drug layers are coloured grey and the inert layers of excipient are coloured white.

		1−Layer	3−Layer	5−Layer
$y = 0$	$0 \leq x \leq x_1$	$c = C_s$	$c = 0$	$c = 0$
$y = 0$	$x_1 \leq x \leq x_2$	–	$c = C_s$	$c = C_s$
$y = 0$	$x_2 \leq x \leq x_3$	–	–	$\left.\frac{\partial c}{\partial y}\right\|_{y=0} = 0$
$y = 0$	$x_3 \leq x \leq x_4$	–	–	$c = C_s$
$y = 0$	$x_4 \leq x \leq x_5$	–	–	–
$y = Y$	$x \geq 0$	$c = 0$	$c = 0$	$c = 0$

where x_1 etc. are defined in Figure 3.1. The rectangular region of interest for a compact consisting entirely of drug extends from $x = x_0$ to $x = x_1 = X$, the end of the compact. x_0 is a point away from the leading edge, where the finite difference scheme is initialised using the Kestin-Persen analytical solution. The computational domain for the 3- and 5-layer configurations extends from $x = x_3 = X$ in the 3-layer case and $x = x_5 = X$ in the 5-layer case (see Figure 3.1) The surface boundary condition is undefined for the last layer of both the 3- and 5-layer configurations. This is because the drug mass transfer can be calculated at the end of the last drug layer.

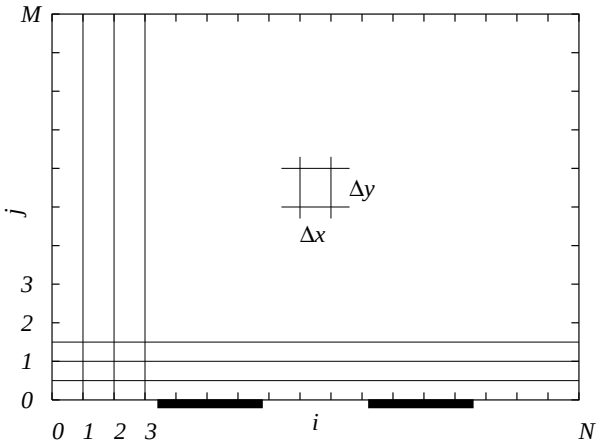

Figure 3.2: Finite difference grid; flow from left to right, compact streamwise along the bottom. A 5-layer compact is illustrated with the diffusing drug layers highlighted as bold black lines.

3.4 Numerical Methods

3.4.1 Introduction

To obtain a finite difference solution, the region of interest is covered by a grid with solutions calculated at the intersection points [120]. For a two-dimensional grid, the grid intersection points or nodes are denoted by two indices, i and j, corresponding to the point's x and y location [102]. The grid spacing in the x direction is Δx and Δy in the y direction [94]. The indices run from 1 to M in the x direction and 1 to N in the y direction. We can write

- $x_i = i\Delta x,\ i = 0, 1, 2, ..., M$
- $y_j = j\Delta y,\ j = 0, 1, 2, ..., N$

parallel to the x and y coordinate axes [120]. The grid cell size is defined as $h = \sqrt{\Delta x \Delta y}$.

3.4.2 Crank-Nicolson Scheme Implementation

We used the Crank-Nicolson (CN) scheme (see e.g. [94]) because (i) it is convenient and relatively simple to implement (ii) it is well documented and (iii) and it performs well in Dehghan's 2004 comparison of numerical schemes being competitive in terms of error [120]. According to Britz [134] there is general agreement that the CN scheme has better accuracy, stability and computational efficiency. It is unconditionally stable except in unusual circumstances [c.f. 196; 157; 120]. It incorporates no numerical diffusion [157; 120; 129][2]. The CN method is equivalent to the *trapezium* method which is used to solve ordinary differential equations [157]. In the recent work completed on the problem of diffusion to channel electrodes [136; 132; 158], finite difference has been the method of choice. The CN scheme does have disadvantages, including extra computing overheads when compared with explicit methods and a tendency to respond to discontinuous jumps in initial conditions with persistent oscillations [198; 157] but for the relatively uncomplicated problems investigated in this thesis, the computational overhead is not a problem and the simple CN scheme seems to work well.

A rectangular $M \times N$ grid is imposed on the region of interest, i and j denoting the x and y indices respectively. Equation (3.8) is linear and parabolic and can be solved readily using the Crank-Nicolson implicit scheme, second order accurate in space and first order accurate in the time-like sense, based on primitive variables [120]. x is the time-like independent variable in this case while y is the space variable. Beginning with the finite difference *stencil*:

$$-(\epsilon + 2s)c_{j-1}^{i} + 4(1+s)c_{j}^{i} + (\epsilon - 2s)c_{j+1}^{i} = (2s+\epsilon)c_{j-1}^{i-1} + 4(1-s)c_{j}^{i-1} + (2s-\epsilon)c_{j+1}^{i-1} \tag{3.11}$$

[2]Although the Crank-Nicolson scheme is widely assumed to be free of numerical diffusion, this is not true under all circumstances. When used to solve the advection-diffusion-reaction equation, for example, numerical diffusion does affect the accuracy of the CN scheme [197].

where c_j^i is the concentration of drug at i, j and ϵ and s are defined as $\epsilon = \frac{v}{u}\frac{\Delta x}{\Delta y}$ and $s = \frac{D}{u}\frac{\Delta x}{(\Delta y)^2}$; Δx and Δy are the x and y grid spacings. Representing the right hand side of the equation by d_n,

$$d_j = (2s + \epsilon)c_{j-1}^{i-1} + 4(1 - s)c_j^{i-1} + (2s - \epsilon)c_{j+1}^{i-1} \tag{3.12}$$

we can write

$$-(\epsilon + 2s)c_{j-1}^{i} + 4(1 + s)c_j^i + (\epsilon - 2s)c_{j+1}^i = d_j \tag{3.13}$$

As outlined by White [114], if we assume that $j = 0$ is the wall and $j = N$ is the free-stream, Equation (3.11) yields $N - 2$ equations with three unknowns in each. With the boundary conditions described, the $N - 2$ simultaneous equations at every i-position are solved using the tridiagonal matrix algorithm [114] to give the concentration values at each grid point, i.e.:

$$\begin{pmatrix} 4(1+s) & -(\epsilon+2s) & & & & \\ \epsilon - 2s & 4(1+s) & -(\epsilon+2s) & & & \\ & . & . & . & & \\ & & \epsilon - 2s & 4(1+s) & -(\epsilon+2s) & \\ & & & \epsilon - 2s & 4(1+s) & \end{pmatrix} \begin{pmatrix} c_N \\ c_{N-1} \\ . \\ c_1 \\ c_0 \end{pmatrix} = \begin{pmatrix} d_N \\ d_{N-1} \\ . \\ d_1 \\ d_0 \end{pmatrix} \tag{3.14}$$

x is evaluated at the previous step, i.e. the last known value. From $j = 1$ to $j = N - 1$:

$$d_j = (2s + \epsilon)c_{j-1} + 4(1 - s)c_j + (2s - \epsilon)c_{j+1} \tag{3.15}$$

where u and v are calculated at $(i - 1,\ j)$. The derivative boundary conditions are implemented as forward-difference second order, 3-point approximations, namely

[136]

$$\Rightarrow c_0 = \frac{4c_1 - c_2}{3} \tag{3.16}$$

where c_0 is the unknown concentration value at the surface at grid position i, while c_1 and c_2 are the concentration values at Δy and $2\Delta y$ from the surface respectively, also calculated at i.

3.4.3 The Thomas Algorithm: Solving the Tridiagonal System

The vertical grid points are numbered from $j = 0$ to $j = N$, where $j = 0$ and $j = N$ are the surface and far-field boundary conditions respectively, and $j = 1$ to $j = N-1$ are internal grid points. Following the algorithm outlined by Ehrlich [137] and the approaches outlined by White [114] and Minkowycz [140], the process for solving the systems of linear simultaneous equations resulting from the Crank-Nicolson scheme at each i-position is described below using conventional nomenclature and with quantities defined in the preceding pages.

1. In regions with Dirichlet surface boundary conditions, that is with c defined at the surface

$$f_1 = \frac{2s_1 - c_1}{4(1 + s_1)} \tag{3.17}$$

$$u_1 = \frac{d_1 + (2s + c)C_0}{4(1 + s)} \tag{3.18}$$

This is the case across the entire surface of the 1-layer compact, across layers 1 and 2 of 3-layer compacts and layers 1,2 and 4 of 5-layer compacts. For the non-diffusing middle layer of the 5-layer compact, define:

$$f_1 = \frac{-4c_1 + 4s_1}{12 - 4c_1 + 4s_1} \tag{3.19}$$

$$u_1 = \frac{3d_j}{(12 - 4c + 4s)} \tag{3.20}$$

2. Calculate f_j and u_j for all y_j, $j > 1$, where:

$$f_j = \frac{2s_j - c_j}{4(1 + s_j) - (c_j + 2s_j)f_{j-1}} \tag{3.21}$$

$$u_j = \frac{d_j + (2s_j + c_j)u_{j-1}}{4(1 + s_j) - (c_j + 2s_j)f_{j-1}} \tag{3.22}$$

3. Using successive back-substitution, calculate $c_{i,j}$ from $j = N-2$ to $j = 1$ using

$$c_n = f_n - u_n c_{n+1} \tag{3.23}$$

c_{N-1} can be calculated by substituting in for f_{N-1} and u_{N-1} and observing that $c_N = 0$ (the far-field boundary condition)

$$c_{N-1} = \frac{d_{N-1} + (2s_{N-1} + c_{N-1})u_{N-1}}{4(1 + s_{N-1}) - (c_{N-1} + 2s_{N-1})f_{N-1}} \tag{3.24}$$

In regions with Dirichlet surface boundary conditions, c is defined at the surface. In regions where a Neumann boundary condition exists at the surface, i.e. inside regions where there is no flux of drug or $\left.\frac{\partial c}{\partial y}\right|_{y=0} = 0$, c_0 is calculated using the second order Neumann expression [134; 136].

$$c_0 = \frac{4c_1 - c_2}{3} \tag{3.25}$$

This process is repeated for each i position along the computational domain.

3.4.4 Mass Transfer Calculation

Since the fluid velocity u and the concentration c can be found at each grid point, the drug mass transfer rate from the compact is then estimated using

$$\dot{m}|_{level\ x} = 2\pi a \int_0^{\delta_c} uc\ dy \tag{3.26}$$

where δ_c is the concentration boundary-layer thickness at x, i.e. the distance from the surface at which the concentration of drug, c, is within 1% of the free-stream concentration (also called the bulk concentration). This can solved numerically using

$$\dot{m}|_x = 2\pi a \sum_{j=0}^{j=M-1} u_j^i c_j^i \Delta y. \tag{3.27}$$

Evaluated at the end of the last drug layer, this expression sums the amount of dissolved drug passing level x per second. i represents the normal position of node points while j represents the axial position of a node; Δy is the normal step between nodes. In practice M should be large enough so that Y, the extent of the computational domain normal to the surface, is larger than δ_c evaluated at the end of the last drug layer.

3.4.5 Tackling the Singularities in the Numerical Solution

Although our problem features discontinuities in the normal first derivative of concentration at the edges of the diffusing regions, these discontinuities do not lead to singular behaviour anywhere in our solution although they do initiate oscillatory behaviour in the Crank-Nicolson calculation of the normal first derivative of concentration. This is demonstrated in the results.

However, there is also a singularity inherent in the solution to the steady-state advection-diffusion equation for a 1-layer system at $x = 0$, the leading edge of the surface. This inconsistency is caused by a normal velocity profile which changes increasingly rapidly approaching $x = 0$. We employed a recommended work-around

[94; 169; 170; 171]: the singularity was avoided by using an analytical solution that incorporates the singularity in the region around the troublesome point. Initial concentration values are provided by using the Kestin-Persen solution [108] to initialise the numerical solution far away from $x = 0$ at x_0. x_0 must be far enough away from the leading edge to have a reasonably well-developed drug concentration profile and so ensure that there is enough information to initialise the finite difference calculation.

This technique was only used for the 1-layer compact since we do not need to calculate concentration values close to $x = 0$ for 3 and 5-layer compacts.

3.4.6 Verification

The GCI method requires that at least solutions from two differently spaced grids are used [149; 142]. Results from the two (or more) calculations are then used to assess the formal order of accuracy of the solution (if this is not known) and to obtain an estimate of the actual discretisation error(s). The GCI method is outlined in detail by Celik [149] but in summary the error calculated for a 2D numerical solution proceeds as follows.

The first step is to define a *representative cell size*, h. For a uniformly spaced grid, this quantity is $h = \sqrt{\Delta x \Delta y}$ (see Section 2.4.1). Otherwise, it is defined as the square root of the total area of the grid divided by the number of cells.

Selecting three very different grids (defined by h_1, h_2 and h_3 with h_3 the most coarse and h_1 the finest), we determine the value of the important resulting variable from each. These values are used in the error estimation calculation. In our case, the important variable is $\dot{m}$, the total mass transfer rate from the system. As defined, $h_1 < h_2 < h_3$; we introduce $r_{21} = h_2/h_1$ and $r_{32} = h_3/h_2$.

We then calculate the *apparent order of accuracy*[3] p of the scheme using the ex-

[3]The apparent order of accuracy is the accuracy of the scheme as determined using the GCI method. The formal order of accuracy is generally determined using Taylor series expansion. p is *apparent* rather than *formal* because it is arrived at by observation of the scheme's behaviour rather than by theoretical derivation.

pression $p = \frac{1}{\ln(r_{21})}|\ln|\epsilon_{32}/\epsilon_{21}| + q(p)|$ where $q(p) = \ln\left(\frac{r_{21}^p - s}{r_{32}^p - s}\right)$, $s = 1.sign(\epsilon_{32}/\epsilon_{21})$ and $\epsilon_{32} = \dot{m}_3 - \dot{m}_2$ and $\epsilon_{21} = \dot{m}_2 - \dot{m}_1$, $\dot{m}_k$ is the mass transfer rate on grid k. The intermediate variables ϵ_{21} and ϵ_{32} yield useful information about the scheme; for example, if $\epsilon_{32}/\epsilon_{21} < 0$ then the convergence of the scheme as $\Delta h \to 0$ is *oscillatory*. See [e.g 146; 152] for a more detailed discussion of the modes of convergence on a solution as Δh decreases.

The *extrapolated* variables $\dot{m}_{\text{ext}}^{32}$ and $\dot{m}_{\text{ext}}^{21}$ are then calculated as $\dot{m}_{\text{ext}}^{21} = (r_{21}^p \dot{m}_1 - \dot{m}_2)/(r_{21}^p - 1)$ and $\dot{m}_{\text{ext}}^{32} = (r_{32}^p \dot{m}_2 - \dot{m}_3)/(r_{32}^p - 1)$. These are estimates of the converged values of the mass transfer rates.

Finally, the error estimates for a scheme of *apparent* order p are (i) the *approximate* relative error $e_a^{21} = \left|\frac{\dot{m}_1 - \dot{m}_2}{\dot{m}_1}\right|$, (ii) the *extrapolated* relative error $e_{\text{ext}}^{21} = \left|\frac{\dot{m}_{\text{ext}}^{12} - \dot{m}_1}{\dot{m}_{\text{ext}}^{12}}\right|$ and (iii) the *grid convergence index* $\text{GCI}_{\text{fine}}^{21} = \frac{1.25 e_a^{21}}{r_{21}^p - 1}$.

The GCI is uncertainty in the finest grid solution (defined by h_1) and along with the apparent order p is a measure of the confidence that we can place on the value of $\dot{m}_1$. The Journal of Fluids Engineering requires that measures such as these are provided with any numerical studies submitted to the journal [144].

The Crank-Nicolson finite difference scheme employed in this thesis was verified using the GCI method to demonstrate that the drug mass transfer rate estimated with the 5-layer finite-difference model will converge to a single value as the x and y grid spacing decreases. In addition, the 1-, 3- and 5-layer numerical simulations were run for a wide range of Δx and Δy interval sizes in order to investigate the effect on the result. The mass transfer rates at the start and the end of the inert region, as well as the overall mass transfer rate from the system, were recorded.

3.4.7 Validation

Our choice and use of the Crank-Nicolson finite difference scheme was informed by the literature and validated against (i) physical experiments carried out in Trinity College Dublin [104; 21] and (ii) analytical solutions, two of which were produced as

part of the PSUDO project [108; 21; 17], and following the guidelines set out in [142; 153]. The physical experiments and the analytical and numerical models defined as part of the PSUDO project and extended in this thesis were designed by a cross-disciplinary research team comprising pharmacists, mathematicians and engineers [20]. The multi-layer delivery systems under consideration were chosen to emphasise the physics of interest (the effect of surface area and freestream fluid velocity on drug mass transfer rates). Although the models were originally developed and run by the PSUDO team, results from the models presented in this thesis were acquired quite independently of the corresponding physical experiments [104; 19]. The processes studied in the first part of the thesis were relatively straightforward and relatively well-defined. The validation proceeded from the simple 1-layer system to the 5-layer system, which was complicated by the Neumann boundary condition. Validation of the code involved a comparison of the estimates for the overall mass transfer rates and of the experimental and simulated concentration profiles at different locations for different tablet types. These results are presented and discussed in Chapter 6.

3.5 Computing Platforms

Python was chosen as the main development platform for the numerical work because of its ease of use and set-up, its flexibility, its extensive range tools and libraries, and its clear syntax. All the Python based models presented in this thesis were run on a Wintel P4 2.4GHz machine with 512 MB RAM while the Fluent simulations were run on a Linux/AMD 2400 (Intel P4 equivalent) with 1 GB RAM.

3.6 Chapter Summary and Conclusions

This chapter introduced the theory and methods associated with the core investigation of the initial drug dissolution rate from a multi-layer cylindrical tablet in the USP apparatus. This included descriptions of the model set-up, the governing

equations, the boundary and initial conditions, the numerical methods, including the finite-difference method, and the verification and validation methodologies used. The utility of the methods presented here and their relevance to the thesis, that mathematical and numerical methods are useful for pharmaceutics, is discussed in Chapter 6. Chapter 4 continues with a description of literature, theory and methods related to the second of the three studies presented in this thesis.

Chapter 4

Literature Review, Theory and Methods, Study 2

This chapter describes the literature, theory and methods related to the second of the three studies that contribute to this thesis, an investigation of the flow around the top of a cylinder using a commercial computational fluid dynamics code. A specific application to a complementary, topical, problem for the wind energy industry was considered. The techniques employed could be applied to the problem of flow about a cylindrical tablet in cross-flow in the USP apparatus.

4.1 Introduction

4.1.1 Wind-speed Measurement

Worldwide, wind energy is currently experiencing unprecedented growth, with total installed generating capacity growing from 14 gigawatts (GW) in 1999 to 48 GW in 2004 [199]. Since the energy density and power output of a wind turbine depend strongly on the cube of the wind-speed at hub height [200], and since the accepted overall uncertainty in the determination of the energy density and power output is between 4 and 6% for a turbine sited on level ground [201], accurate wind

measurements are vital when assessing the economic viability of a proposed wind project.

The wind-speed at a site is measured by installing an anemometer on top of a meteorological mast. The anemometer is ideally located at the same height as the hub height of the turbines proposed for the site [202].

According to recommended guidelines [203], bad practice in anemometer mounting and meteorological mast design can potentially introduce an uncertainty in wind speed measurement. This uncertainty has significant financial implications for any wind energy project. It follows that careful consideration must be given to anemometer mounting, specifically to the effect of the airflow distortion around the anemometer and the tower to which it is attached. For the tubular meteorological towers, the generally assumed obstacles to the flow include lightning rods, the directional vanes and mounting booms. Top-mounted anemometers were previously considered by many to be in unperturbed wind flow (Figure 4.1).

Although the flow pattern around a tower is horizontal for most of its height, it becomes three-dimensional close to the top, where the air is accelerated over the free end [204]. This accelerated airflow is often called *speed-up*. Recently, evidence has been found to show that such speed-up can significantly affect measurements made by top-mounted anemometers on tubular towers [205].

4.1.2 The Effect of Nearby Obstacles on Wind-speed Measurements

Understanding the flow around bluff bodies is important for many reasons, e.g. pedestrian comfort in the wake of buildings and pollutant dispersion [206]. Additionally, understanding the effect of buildings and other structures on wind-speed measurements is an important reason for understanding such flows. It is well known that airflows accelerating around obstacles can lead to inaccurate wind-speed measurements if the anemometer is placed in this accelerated airflow, e.g. Durgin et

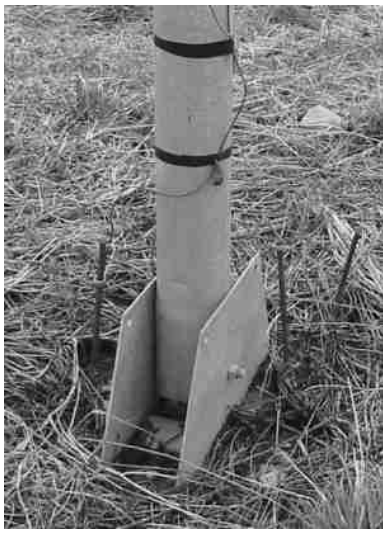

(a)

(b)

Figure 4.1: (a) The base of a typical hollow tower. The gap between the bottom of the tower and the base-plate is clearly visible. (b) Typical mounting with vertical boom.

al. consider corrections to the data recorded by an anemometer located on a tower above a tall building in downtown Boston [207]. Shin et al. consider the measurement errors associated with the main meteorological tower at a nuclear power plant in New York [208]. Following an experimental programme using a scale model in a wind-tunnel, important findings include that the effect of the structure on the data is *independent of the wind-speed*. These papers highlight the importance of correcting wind speed measurements for flow distortion effects.

Most importantly for this thesis, Kline investigated the magnitude and nature of the error in wind-speed measurements from top-mounted anemometers due to interference from tubular meteorological towers [205]. Kline considered data from five 50 m towers with anemometers placed on top-mounted booms 30 cm above the top of the tower. The study concluded that the airflow is accelerated over the top of the tower, causing the anemometers to record wind-speeds up to 3% in excess of the mean wind-speed and that the use of top-mounted anemometers should be discouraged [205].

Despite this evidence, poor practice in anemometer design, mounting and calibration persists and published information on the subject is relatively scarce [209]. An informal comparison of contemporary commercial anemometer specifications with the international best practice [203] reveals some discrepancies between recommended and actual practices.

4.2 Flow Around Infinite Cylinders

The writings of most relevance to this study are those concerned with both two- and three-dimensional flow around circular cylinders. As a starting point, the classic texts of Prandtl [193; 210] and Batchelor [211] as well as the more recent textbook by White [114] have been invaluable. The state of the art as regards understanding of the flow about a cylinder of infinite extent is summarised in Coutanceau and Defaye's illustrated review article [212]. The NACA archive has many high quality papers from years spanning 1917 to 1958.

Papers from the archive, including those by Lindsey [213], Wieselsberger [214] and Zahm [215] are useful and together with the textbooks, serve as good introductions to cylinders in cross-flows. Wieselsberger's 1922 discussion introduces the concept of the *drag coefficient*, C_d, a measure of the resistance a body experiences when moving in a fluid [214]. C_d is defined in the equation

$$F_d = \frac{1}{2} C_d \rho v^2 A \tag{4.1}$$

where F_d is the drag force experienced by the body, ρ is the density of the fluid, v is the translation velocity and A is the frontal area of the body. Before the 1900s, it was thought, after Newton, that C_d was constant for all velocities and absolute dimensions of the body. In the early part of the last century, however, it was demonstrated that C_d in reality depends on the absolute dimensions of the body and its velocity relative to the fluid and on the viscosity of the fluid. C_d remains

constant only for geometrically similar flows. As described by Reynolds, two flows can be considered geometrically similar only when the quotient $\frac{UD}{\nu}$, where U is the free-stream fluid velocity, D is any linear dimension (which must be the same in both cases considered; usually the diameter for flows around cylinders) and ν is the viscosity of the fluid, is the same for both flows [214; 210]. This quotient is called the Reynolds number, Re[1]. C_d is, therefore, a function of Re, the Reynolds number associated with a cylinder of diameter D, i.e. $C_d = f(Re)$

Zahm [215] presents formulae for calculating C_d and F_d on simple quadric shapes on a two-dimensional plane, i.e. a sphere, a round cylinder, an elliptic cylinder and prolate and oblate spheroids. Other workers, including Stokes, Oseen, Relf and Lamb, had previously generated analytical and empirical formulae relating C_d to Re for certain ranges of Re [210; 114]. For a flow of $Re_D < 200,000$, Zahm [215] gives the empirical formula

$$C_d = 9.4Re^{-0.8} + 1.2 \tag{4.2}$$

where C_d is the drag coefficient and Re is the Reynolds number associated with two-dimensional (2D) flow about a cylinder. 2D plane flow about a cylinder is sometimes referred to as flow about an infinite cylinder, since a cylinder with no ends will produce a flow pattern equivalent to 2D flow. Equation (4.2) agrees well with measurements of and other approximations to C_d around a cylinder (Figure 4.2).

As discussed in great detail in textbooks and papers [e.g 210; 114; 102], the range of Reynolds numbers of practical interest is very wide, up to about 8×10^5 for an infinite cylinder and plotting using a logarithmic scale becomes necessary in order to identify detail at smaller Reynolds numbers. Wieselsberger produced the well-known C_d vs. Re_D curve plotted on logarithmic paper [214] (reproduced by Zahm [215] in Figure 4.2). The fact that the drag coefficients of cylinders of various

[1] Again, see the Glossary for a brief discussion of this important parameter.

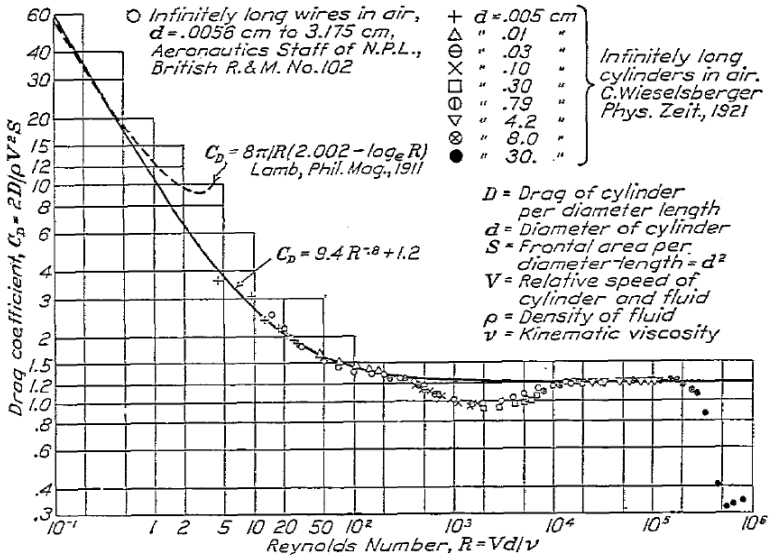

Figure 4.2: *Drag coefficient for a smooth endless cylinder in steady translation through a viscous fluid.* Reproduced from [215].

diameter all fall on a single curve was taken as a verification of Reynolds' law of similarity [210].

In addition to the classic texts, modern studies are still providing new results about two-dimensional flows about a cylinder. Franke and Frank [206] describe a numerical model which uses and assesses large eddy simulation (LES) finite-volume techniques in the simulation of the transition to turbulence of the flow around a two-dimensional cylinder. The paper reports results from the authors' simulations and validations with experiment and previous simulations, all for a critical Reynolds number of 3,900. Apelt's 1958 finite difference treatment of low Reynolds number flow around a cylinder is useful [216]. In general, however, excepting the effects of turbulence, this problem is well understood and covered extensively in the literature and textbooks [e.g. 114].

4.3 Flow Around Finite Cylinders

The problem of a finite circular cylinder[2] in cross-flow has also been extensively studied because of the interesting complex flow phenomena it produces and because of its importance in practical engineering [217; 218]. However, although the finite cylinder is much studied, it is less well understood and new work still appears [219].

The primary references for flows about finite cylinders used in this thesis include a paper by Park and Lee [204]. This is an experimental paper, and contains very useful measurements and images of the flow about finite cylinders, of aspect or height to diameter ratios (H/D) 6, 10 and 13, at a Reynolds number of 20,000. Complex three-dimensional flow structures are observed in the wake of finite cylinders; these structures are the result of quasi two-dimensional flow around the cylinder interacting with axial flows. Although many factors contribute to the three-dimensional behaviour of the wake flow, *free end or tip-flow effects*, resulting from flow over and around the free end of finite cylinders, make the most significant contribution to these axial flows [204]. The complexity of the wake structures is vividly demonstrated by some experimental observations due to Park and Lee. The complexity of the wake flow is corroborated and discussed in many other studies for various Reynolds numbers [e.g. 220; 217].

The vortex formation length is defined as the distance from the lee-side of the cylinder to the region of maximum velocity fluctuation in the cylinder wake and has a value of about 2 for short cylinders[3] of $H/D < 10$ and 1 for taller cylinders $H/D > 10$ [220; 204]. The longer vortex formation region for cylinders of small aspect ratio may be a result of the additional influence of the *necklace* vortex that forms around the base section of a finite cylinder and which also contributes to the three-dimensionality of the flow behind a finite cylinder [217]. For cylinders of small aspect ratio ($H/D < 6$), the effect of flow around the free-end influences the wake

[2] i.e. a cylinder that does have ends.

[3] Normalised with respect to the vortex formation length of a two-dimensional cylinder.

flow over the entire length of the cylinder, while for relatively long cylinders, the free-end influence is confined to a region close to the free-end [220]. The tip-flow effect on the base pressure coefficient[4] increases with H/D for $H/D < 7$, and then remaining constant for $H/D \geq 7$ [218]. A particularly important observation is that, aside from the wake region, the flow is essentially two-dimensional at a level two diameters below the top of the cylinder [204].

This wake flow structure[5] is observed at all Reynolds numbers [217]. The influence of the free-end and the base effects increases along the cylinder with increasing Reynolds number and with decreasing aspect ratio.

Several experimental descriptions of the flow around a finite cylinder are instructive [204; 217]. When a flow approaches the free-end of a finite cylinder, the flow moves upwards, accelerating around the free-end before separating from the cylinder at the free end and forming a *trailing vortex*. This trailing vortex is pushed downwards, influencing the wake behind the top half of the finite cylinder. The wake behind the lower half of the cylinder is practically two-dimensional and not influenced by the downwash.

4.4 Flow Around a Meteorological Tower

The meteorological mast studied was a 50 m high thin-walled tubular tower with an outside diameter of 0.15 m. The tower was hollow, with a gap between its base and the ground (Figure 4.1 (a)). The anemometer was located only 0.30 m (two diameters) above than the top of the tower, close enough that wind-speed measurements were likely to be affected by speed-up. In assessing the effect of the tower on the anemometer, we studied various configurations of wind-speed,

[4]The base pressure coefficient C_{p_b} can be derived from Bernoulli's equation, $p + \frac{1}{2}\rho V^2 = \text{const}$, where ρ is the fluid density. This can be re-written as $p_s = p_\infty + \frac{1}{2}\rho U_\infty^2(1 - 4\sin^2\theta)$ for flow about a cylinder. C_{p_b} can then be written, $C_{p_b} = \frac{p_s - p_\infty}{\frac{1}{2}\rho U_\infty^2}\ C_{p_b}$. See also Glossary.

[5]Suppressed two-dimensional flow around the mid-regions of the cylinder with significant three-dimensional effects at the free-end and close to the base.

turbulence and the slope of the local terrain. We also took into account the fact that the tower was hollow. This model was built using the commercial computational fluid dynamics (CFD) code Fluent [106], coupled with a simple analytical analysis.

Our objectives in this study were (i) to validate Fluent as a useful tool, in the context of this work, and (ii) to approximate the velocity distortion at the top of a finite cylinder using Fluent.

4.4.1 Validation

The purpose of our validation was to demonstrate that the results from Fluent compare well with the experimentally observed flow structures and associated effects of two dimensional laminar, steady and unsteady flow. The validation was both qualitative and quantitative. Quantitatively, our aim was to approximate the drag coefficient C_d and the pressure distribution C_p[6].

We began by looking at the flow about an infinite, or two-dimensional, cylinder. The validation consisted of running simulations for various Re and comparing the results with experiment and theory [e.g. 212].

For the finite cylinder, the aim was to qualitatively replicate the flow pattern above and around the cylinder as well as calculating C_d, and C_p at various heights along the cylinder.

4.4.2 Meshing the Computational Domain

We experimented with various different grid geometries for both the two-dimensional and three-dimensional simulations. In the two-dimensional case, three domain types were tested, of rectangular, semi-circular and circular shape respectively. As described earlier, these were inspired by reports, tutorials and papers from several sources [e.g 106; 131; 221]. Various grid configurations were tested within each of these three main domain types.

[6]See the Glossary for a brief discussion of this parameter.

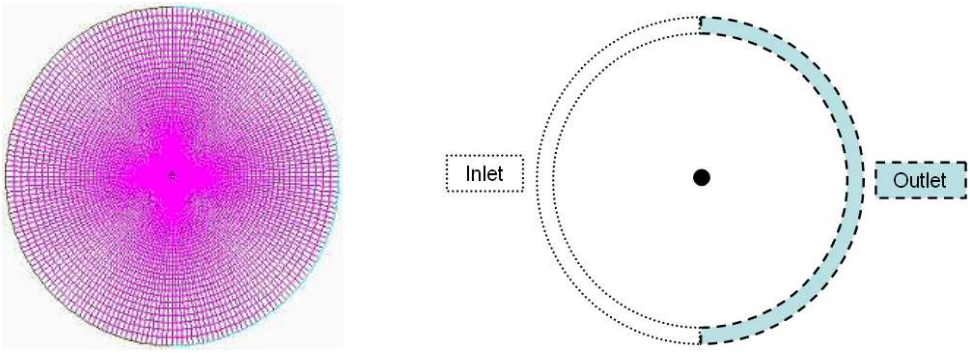

Figure 4.3: The dense two-dimensional computational domain with the cylinder located in the very centre. The left edge is the inlet; the right edge is the outlet.

We considered an infinite cylinder of diameter, D = 2.0 m placed in a uniform crossflow with a free-stream velocity of 1.0 m s^{-1}. The inlet and outlet are 6.25D m and 11.25D m respectively from the centre of the cylinder. The top and bottom of the computational domain are equidistant from the cylinder centre and 8D m apart. Semi-circular and circular domains most closely approximated the flow features of interest to us (the circumferential pressure distribution and separation points, wake configurations and drag coefficients).

In three dimensions, we again tested several domain types, each with more than one internal grid configuration. Similar to the two-dimensional case, the three main domain forms we considered were : a rectangular prism (a brick shape), a semi-spherical domain, and a quarter-spherical domain. The quarter- and semi-spherical domains were found to work best.

The Fluent model consisted of a quarter-sphere with a diameter 40 times that of the cylinder. The cylinder represented the topmost ten diameters ($H/D = 10$) of our met tower ($H/D > 300$). By considering the axial symmetry of flow around cylinders, it was only necessary to model half the tower: this permitted use of a dense mesh without leading to excessive computation time. The mesh for our model contains approximately 650,000 tetrahedral cells, most of them close to the tower. The half-cylinder was placed centrally.

4.4.3 Boundary and Initial Conditions

The properties of the fluid were assumed constant. In the two-dimensional simulations, a no-slip[7] wall condition is applied to the cylinder wall. Uniform free stream conditions with varying degrees of turbulence are applied at the inlet (velocity inlet) and lateral boundaries (symmetry). The flow exit is treated as a pressure outlet.

In the case of a solid three-dimensional tower, there are five boundary conditions. At the bottom of the domain the flow is two-dimensional. The use of a *symmetry* condition as the bottom face enforced this constraint. The flow symmetry about the centre line of the cylinder allowed us to use another symmetry condition on the single vertical surface. The tower itself was assigned a *wall* condition, implying zero wind-speed at the surface. The upstream curved surface was defined as a *velocity inlet*. This allowed us to specify the free-stream wind-speed and a turbulence intensity. We defined the downstream face as a *pressure outlet* with atmospheric pressure. The resulting model is shown in Figure 4.4.

A Fluent case file contains all the necessary inputs required by Fluent to specify a particular problem. This includes the computational domain geometry (including the grid), the boundary and initial conditions, the fluid properties, and the settings of the various solution parameters (for example which turbulence model to use). The fluid properties were set as constant with the boundary conditions described. Fluent's first-order discretisation scheme was used to model unsteady flows for $Re > 50$. It is important to note that the drag coefficient (C_d), is conventionally calculated per diameter length of cylinder, as opposed to per unit length, for convenience.

4.4.4 Dimensional Analysis

Take axes centred at the top of the tower and define D (tower diameter), H (tower height) and U (incident airspeed). Then, if we define $u(z)$ to be the horizontal

[7]The no-slip wall condition is a central, simplifying observation used in boundary-layer theory. It states that there is no relative motion between a surface and that part of the fluid flow which is in contact with the surface.

velocity at a height z above the cylinder:

$$\frac{u(z)}{U} = f(z[\text{m}], D[\text{m}], H[\text{m}], \nu[\text{m}^2\ \text{s}^{-1}], \epsilon[\text{m}], U[\text{m s}^{-1}]) \tag{4.3}$$

where ν and ϵ are the kinematic viscosity of air and the turbulence length scale of the incoming airstream respectively. With some consideration, dimensional analysis then gives us:

$$\frac{u(z)}{U} = F\left(\frac{z}{D}, \frac{UD}{\nu}, \frac{H}{D}, \frac{\epsilon}{U}\right) \tag{4.4}$$

That is, $\frac{u(z)}{U}$ is some function, F, of four dimensionless groups. The dimensionless group $\frac{UD}{\nu}$ is the Reynolds number (Re) of the flow and takes values in the range of 10,000 to 100,000. $\frac{H}{D}$ can be taken as approximately equal to 300. Since the Reynolds number and $\frac{H}{D}$ are both $>> 1$, it is anticipated that $\frac{u(z)}{U}$ is independent of both these numbers. Flows become independent of Reynolds number when Re is large. Similarly, for structures of $H/D > 5$, additional height does not affect flow patterns about the free end(s). So,

$$\frac{u(z)}{U} = F\left(\frac{z}{D}, \frac{\epsilon}{U}\right) \tag{4.5}$$

4.4.5 Modelling Turbulence

The turbulence intensity I is the ratio of the root-mean-square of the velocity fluctuations, u_{rms}, to the mean flow velocity, $\bar{u}$ [117], thus:

$$I = \frac{u_{rms}}{\bar{u}} \tag{4.6}$$

This is the definition adopted by Fluent [106]. There is no one turbulence model that is the best choice for all types of problem; the choice of turbulence model depends on factors including the physics of the flow, conventions for dealing with

particular types of problem, the accuracy required and the resources available [106]. A careful weighing of these factors is required when choosing a turbulence model.

The Spalart-Allmaras (S-A) model was chosen for the wind energy work carried out as part of the work presented in this thesis. This turbulence model is a good choice where speedy results are required and accurate turbulent flow computations are not required [106]. The S-A model is also suitable for relatively coarse grids since it uses *wall functions* when the mesh resolution is not sufficiently fine. In the Fluent implementation of the S-A model, the user is required to provide inlet boundary conditions by setting the turbulence intensity and a turbulence length scale, based on a representative dimension such as the diameter of a cylinder.

4.5 Modelling a Solid Tower

4.5.1 Some Considerations

In a previous study, it was shown that the flow around a finite cylinder at a height of one diameter below the free-end is approximately two-dimensional; the speed-up is not influenced by the airflow far below the top of the tower [204]. For this reason, even though our tower had an aspect ratio of more than 300 ($H/D > 300$), it was necessary only to model the topmost 1.5 m, or a cylinder of height to diameter ratio 10 ($H/D = 10$).

4.5.2 Calculating the Speed-up

On completion of a simulation run[8], we recorded wind-speed values at specified positions close to the free-end of the tower. These were located at 30° intervals, on a circle congruent and concentric with the circumference and at a height of two diameters above the top of the tower (Figure 7.8). These correspond to positions at which the centre of the anemometer may be located. An actual anemometer consists

[8]One run comprises approximately 2,000 0.1 s time-steps, with 50 iterative computing steps in each of them.

of three cups rotating on a fixed circular path around the centre of the device and so the wind-speed is not measured exactly at the centre of the device but rather on the path followed by the cups. From our simulations, however, we concluded that the difference between the speed-up estimated at the centre of the anemometer and the speed-up estimated on the circle followed by the cups is always less than 0.08% of the free-stream wind-speed. The wind-speed estimated at the centre of the anemometer, therefore, represents an acceptable approximation to the values recorded by an actual cup-device for the purposes of this study.

4.6 Modelling a Hollow Tower

4.6.1 Additional Considerations

The accelerating airflow around the top of the tower is at a lower pressure than the still air at the bottom of the tower, next to the ground, where the pressure is atmospheric. This sets up a pressure drop from the bottom to the top and gives rise to an airflow up through the hollow centre of the tower. The velocity of this internal airflow can be computed using the empirical Darcy-Weisbach equation [222], which can be written

$$\omega = \sqrt{\frac{2D\Delta p}{\lambda H \rho}} \tag{4.7}$$

where ω is the speed of the airflow exiting through the top of the tower, Δp is the pressure drop from the bottom of the tower to the top, D is the diameter of the tower, H its height, λ the pipe friction coefficient, calculated iteratively using the Colebrook-White equation [222], and ρ is the air density.

4.6.2 Calculating the Speed-up

The internal airflow through the hollow tower can be captured by changing the top surface of the tower from a wall boundary to a velocity inlet. The air velocity

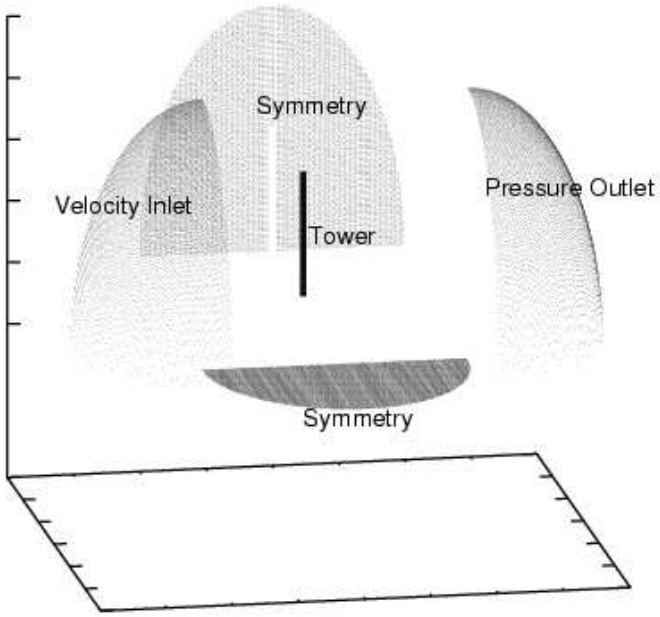

Figure 4.4: The computational domain with exploded surfaces for illustration.

assigned to this inlet is computed using an iterative process (Figure 4.5). Essentially: (1) an initial run of the solid tower simulation provides a pressure value at the top of the tower; (2) using this value to calculate Δp in Equation (4.7), we then estimate the internal airflow speed ω at the top of the tower; (3) we use this value for ω as the top boundary condition for the next simulation run in order to get a new estimate for the pressure drop; (4) this process is repeated until ω converges to a fixed value.

4.7 Modelling a Tower on Sloped Terrain

4.7.1 Additional Considerations

We assumed that in the vicinity of the free-end of a tower positioned vertically on a hill, the airflow is parallel to the slope of the hill and has a turbulence intensity close to that of flat terrain. Turbulence intensity is defined as the ratio of the root-mean-square of the velocity fluctuations, u', to the mean flow velocity, u [117]. Although

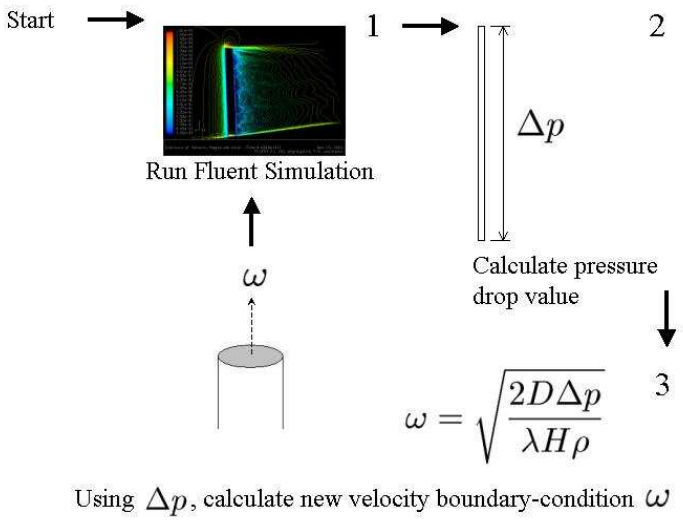

Figure 4.5: The iterative process used to calculate the speed-up over a hollow tower. The process is repeated until ω converges to a fixed value.

the vertical component of turbulence intensity does change on encountering the windward side of a hill [223; 224; 225], this mechanism is not relevant to our study. In addition, as we report later in this thesis, speed-up is not sensitive to changes in turbulence intensity.

4.7.2 Calculating the Speed-up

We need only change the inlet and bottom face boundary conditions. Airflow now enters through the inlet and bottom faces, inclined at an angle to the horizontal equal to the terrain slope.

In addition to speed-up, there are other sources of measurement error associated with anemometers. One source of error, relevant to this thesis, results from the fact that anemometers only measure the wind velocity component perpendicular to the main axis of the device, which is almost always vertical; this has implications for a met tower sited vertically on the windward side of a hill, subject to an uphill wind that is parallel to the slope. In this thesis, the speed-up error can be understood as

both the speed-up error in the actual absolute flow velocity above the vertical tower *and* the speed-up error in the velocity reported by the anemometer.

4.8 Chapter Summary and Conclusions

In this chapter describes the literature, theory and methods related to the second of the three studies that contribute to this thesis were presented. The results from this work are presented in Chapter 7 with a discussion of their utility and how they contribute to the thesis that simulation is useful. Chapter 5 continues with a description of the third of the three studies presented in this thesis.

Chapter 5

Literature Review, Theory and Methods, Study 3

The third part of the work presented in this thesis concerns one possible end state for a dissolving tablet: fragmentation into small particles with dissolution continuing from the disintegrated solid masses. A framework for calculating the motion of, and dissolution from, a drug particle moving through the USP apparatus is outlined, beginning with a review of the classical work of Taylor and Glauert [22; 23], who considered the motion of raindrops in airflows. This chapter presents the literature, theory and methods relevant to this third study.

5.1 Describing Particle Motion in a Fluid

In 1940, G.I. Taylor outlined, with great clarity of thought, a methodology for determining the two-dimensional equations of motion of raindrops moving in curved airstreams [22]. This work was to facilitate the design of a suitable wind tunnel for carrying out de-icing experiments. In this paper, Taylor presented the exact solution for the paths of raindrops moving in a jet impinging on a flat plate, the flow close

to a stagnation point[1], when Stokes' law of resistance[2] is assumed to apply. Taylor defines the two-dimensional equations of motion for a raindrop in a fluid which is moving with velocity components u and v as:

$$\frac{4}{3}\pi\varrho a^3\frac{du_1}{dt} = \frac{1}{2}\pi C_d\rho a^2 q(u-u_1)$$

$$\frac{4}{3}\pi\varrho a^3\frac{dv_1}{dt} = \frac{1}{2}\pi C_d\rho a^2 q(v-v_1)$$

where C_d is the drag coefficient of a sphere,
$q = \left((u-u_1)^2+(v-v_1)^2\right)^{\frac{1}{2}}$, u_1 and v_1 are the velocity components of the drop, $2a$ its diameter, ϱ its density and ρ the density of air. With the assumption of Stokes flow, these equations can be written in a simplified form. In general, the equations of motion must be solved numerically. In 1940, before the advent of modern computing, Glauert calculated the paths of the particles using an unspecified *step-by-step*, or numerical, integration method [23].

Glauert further applied Taylor's technique to the problem of ice accumulation on a two-dimensional circular cylinder and an airfoil. Using the equations of motion for Stokes flow developed by Taylor, Glauert hand-computed two-dimensional paths for raindrops of different sizes moving around various simple shapes. The combined work of Taylor [22] and Glauert [23] forms an excellent introduction to particle tracking in a fluid, i.e. simple *two-phase* flow.

Several related NACA papers were also published at that time and a subsequent paper by Bergrun provides a very useful expansion on the techniques described by Glauert, applied to a NACA airfoil [226]. In particular, Bergrun discusses the case when the raindrop departs from Stokes flow. In this case, the equations of

[1]When a fluid flow impinges on a surface, e.g. perpendicularly onto a flat plate, the middle stream-line will come to rest at a point on the surface. This is a stagnation point [see e.g. 193].

[2]Stokes flow or *creeping flow* assumes that the density, or inertia, terms are all negligible in the equations of motion. It can be shown by non-dimensionalising the *Navier-Stokes* momentum equation that this assumption is valid only for very small Reynolds numbers [193; 210; 114].

motion solved by Glauert must be modified to account for a continuously variable drag coefficient, C_d. Assuming that the acceleration of the particle is constant over the time-step, Bergrun outlines an integration method using a linear first order approximation for velocity and a second order approximation for position; taking the x-direction:

$$u^p_{n+1} = u^p_n + a^p_n \Delta t + O(h)$$

$$x^p_{n+1} = x^p_n + u^p_n \Delta t + a^p_n \Delta t^2 + O(h^2)$$

This amounts to using the *Euler* integration method to calculate new velocities and positions. Since the velocity values are only $O(h)$ accurate, the accuracy in the calculation of positions is not as good as the theoretical $O(h^2)$. Bergrun also presents a method of estimating the initial relative difference, or *differentials* between the particle and flow velocities which are required to initiate the calculations. A later paper contains further useful derivations associated with particle motion about an airfoil [227].

In more recent years, refinements in computing and mathematical descriptions have led to significant progress in particle tracking capabilities. Nevertheless, the basic mathematical descriptions of and methodologies for Eulerian/Lagrangian[3] calculations of particle motion through an aerodynamic or hydrodynamic field have not changed very much in a broad sense [229]. The paths of the particles moving through the velocity field are calculated by numerical integration of variations of the equations of motion. For example, additional forces may need to be included [e.g. 230]. In the general case, the velocity field is too complex to be calculated

[3]Eulerian descriptions of two-phase flows consider effects relative to a fixed point in space while Lagrangian descriptions describe the effects relative to the reference frame of a particular particle moving through the fluid. In the Eulerian description of motion, the velocity $\mathbf{v}_i$ is defined in terms of x, y, z, t, i.e. $u(x, y, z, t)$, $v(x, y, z, t)$, $w(x, y, z, t)$ while in the Lagrangian system, $x_A(t)$, $y_A(t)$ and $z_A(t)$ are specified for each fluid particle. In general, Lagrangian computational models have grid points that move with the fluid, while Eulerian grid points remain fixed in space [228].

analytically and instead fluid velocity values at a finite number of discrete points are computed using a numerical computational fluid dynamics (CFD) code, such as the commercial code Fluent. The resulting structured or unstructured matrix of velocity data, associated with the CFD grid points, is then used to calculate the motion of the particle. For a steady velocity field, which is assumed to be unaffected by the motion of the particle, the particle position is first located in the grid. If the particle is not at a grid point, velocity information from surrounding grid points must be interpolated to find the fluid velocities at the particle location. Using this information, the equations of motion must be integrated to determine the position of the particle at the next time-step. This new position must then be located in the data set and the process starts over again.

5.2 Governing Equations

As outlined above, one version of the two-dimensional equations of motion for a spherical drop in a steady stream with velocity components u and v are [22]:

$$\frac{4}{3}\pi\varrho a^3\frac{du_1}{dt} = \frac{1}{2}\pi C_d\rho a^2 q(u-u_1) \tag{5.1}$$

$$\frac{4}{3}\pi\varrho a^3\frac{dv_1}{dt} = \frac{1}{2}\pi C_d\rho a^2 q(v-v_1) \tag{5.2}$$

where, as described above, C_d is the drag coefficient, $q = \left((u-u_1)^2+(v-v_1)^2\right)^{\frac{1}{2}}$, u_1 and v_1 are the velocity components of the drop, $2a$ its diameter, ϱ its density and ρ the density of the fluid. If x and y are the coordinates of the drop at time t, then

$$\frac{dx}{dt} = u_1, \frac{dy}{dt} = v_1$$

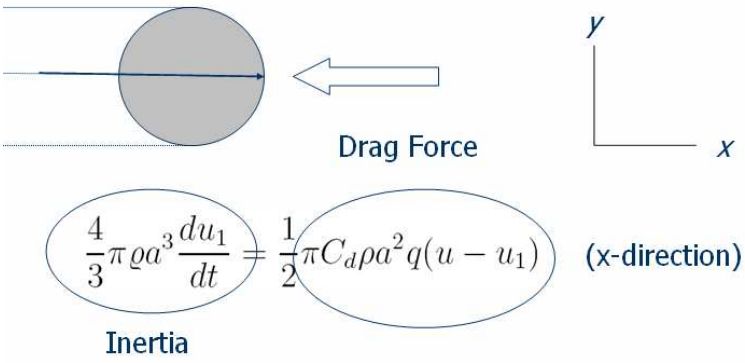

Figure 5.1: With the basic equations of motion, $F_{\text{Inertia}} = \frac{d}{dt}(mv)$ and $F_d = ma$, where m is the mass of the particle, v its velocity and a in this context its acceleration, there is a balance between the inertia and drag forces.

5.3 Forces

We can readily see that the left hand side of Equations (5.1) and (5.2), the inertial force, arise from Newton's Second Law (Figure 5.1). The right hand side of Equations (5.1) and (5.2) describe the drag force acting on a particle moving through a fluid. In reality, the drag coefficient C_d varies continuously with the Reynolds number Re_p of the particle in the flow[4]. Re_p is given by:

$$Re_p = \frac{2aq}{\nu} \tag{5.3}$$

[210]. C_d can be considered constant, however, in certain situations, such as when the Re_p is large. In other situations, e.g. when the Re_p is very small, the relationship between C_d and Re_p can be approximated as linear [see e.g. 210].

If the particles are assumed to be very small, Stokes' law of resistance can be applied[5]. In this case, the drag coefficient, $C_{d_{\text{Stokes}}}$:

$$C_{d_{\text{Stokes}}} = \frac{24}{Re_p}$$

[4]See the Glossary for a discussion of the Reynolds number.

[5]Strictly, Stokes' law only applies when a flow is very slow, very steady and when the boundary walls are very far away [231].

[210] and ν is the kinematic viscosity of the fluid. It follows that $C_{d_{\text{Stokes}}} = \dfrac{12\nu}{aq}$ and, in terms of u and v, Equations (5.1) and (5.2) then simplify to

$$K_0 \frac{d^2x}{dt^2} + \frac{dx}{dt} - u = 0 \tag{5.4}$$

$$K_0 \frac{d^2y}{dt^2} + \frac{dy}{dt} - v = 0 \tag{5.5}$$

where

$$K_0 = \frac{2}{9}\frac{\varrho}{\rho}\frac{a^2}{\nu} \tag{5.6}$$

Stokes flow pertains when $Re_p << 1$. In the majority of cases, Stokes' law does not apply, e.g. when the particle is relatively large. We observe that, in general [226]:

$$C_d = C_{d_{\text{Stokes}}} \times f(Re_p) \tag{5.7}$$

where C_d is the drag coefficient written in its most general form, $f()$ is a function of Re_p and is based on the empirical formulae given by Loth [232]. We can write that $C_d = C_{d_{\text{Stokes}}} \times f(Re_p) = \dfrac{12\nu}{aq} \times f(Re_p)$. Simplifying Equations (5.1) and (5.2) using C_d instead of $C_{d_{\text{Stokes}}}$ yields

$$C_f K_0 \frac{d^2x}{dt^2} + \frac{dx}{dt} - u = 0 \tag{5.8}$$

$$C_f K_0 \frac{d^2y}{dt^2} + \frac{dy}{dt} - v = 0 \tag{5.9}$$

with variables as defined previously and the correction factor, $C_f = \dfrac{1}{f(Re_p)}$. The correction to the Stokes flow solution for a continuously variable C_d is calculated using Loth's empirical formulas [232]:

- $Re_p <= 1$, $C_f = 1 + \frac{3}{16}(Re_p)$.
- $Re_p > 1$ and $Re_p <= 285$, $C_f = 1 + 0.1935{Re_p}^{0.6305}$.
- $Re_p > 285$ and $Re_p <= 2,000$, $C_f = 1 + 0.015Re_p + 0.2283{Re_p}^{0.43}$.
- $Re_p > 2,000$ and $Re_p <= 3,500,000$, $C_f = 0.44\frac{Re_p}{24}$.
- $Re_p >= 3,500,000$, $C_f = 0.44\frac{Re_p}{24}$.

Equations (5.1) and (5.2) represent a useful description of particle motion in a fluid. However, as outlined by other workers [e.g. 230], other forces act on a particle in a flow. For small Re_p, Equation (5.1) can be written in a more general way as:

$$(m_p + \frac{1}{2}m_f)\frac{du_1}{dt} = (m_p - m_f)g + \frac{3}{2}m_f\frac{du}{dt} + \frac{1}{2}\pi C_d \rho a^2 q(u - u_1) + F_{\text{History}} \quad (5.10)$$

where the m_f terms are *added mass* terms, used to capture the resistance of the fluid to acceleration. F_{History}, the history term, accounts for the effect the particle has on the velocity field. These additional forces, including the effect of gravity g, are ignored by Taylor since they are relatively small for particles the size of raindrops. For the same reasons, they are not included in the analysis presented here.

5.4 Computer Implementation of Particle Motion in a Two-Dimensional Flow Near the Stagnation Point

Taylor and Glauert's results for solution of the two-dimensional equations of motion of raindrops moving in curved airstreams [22; 23] provide a useful comparison for testing the various components of a numerical model of the motion of particles in flows. Taylor presents the exact solution for the case of particle motion close to a stagnation point when Stokes' law of resistance applies. This solution was

implemented numerically and extended in this thesis for the general case when Stokes' law does not apply.

5.4.1 Taylor's Exact Solution

As outlined by Taylor [22], the velocity field close to a stagnation point is given by $u = -cx$, $v = cy$. If these values for u and v are substituted into the general equations of motion, Equations (5.4) and (5.5), the resulting equation may be non-dimensionalised by substituting $z = t/K_0$, $\alpha = K_0 c$. This gives

$$\frac{d^2x}{dz^2} + \frac{dx}{dz} + \alpha x = 0 \tag{5.11}$$

$$\frac{d^2y}{dz^2} + \frac{dy}{dz} - \alpha y = 0 \tag{5.12}$$

Taylor presents exact solutions to Equations (5.4) and (5.5) for various values of α for a particle travelling with the stream at $z = t = 0$. These provide a useful benchmark for numerical implementations.

5.4.2 Review

To calculate the paths of the particles moving through the velocity field, the discrete versions of Equations (5.11) and (5.12) are integrated using a Runge-Kutta method. A generalised particle tracking process is: (1) Calculate the fluid velocities at time t at a finite number of grid points, (2) Search the grid to find the fluid velocities at the position of the particle, (3) Interpolate data from the grid points closest to the particle to determine the fluid velocities at its location, (4) Integrate the equations of motion using these velocities and determine the new particle position, and (5) Analyse and/or visualise the resulting data. For unsteady flows, this process must be completed for each time-step. For steady flows, it is necessary to perform step (1) only once.

For the case of a particle moving in a two-dimensional flow near the stagnation point, the algorithm is as follows: (1) Define the fluid flow as $u = -cx$ and $v = cy$, where x and y are the coordinates of the particle at time t; (2) Define the flow velocities $u = -cx_{t=0}$ and $v = cy_{t=0}$. This is the initial position of the particle. From the assignment on the previous page, at $t = 0$, $z = t = 0$; (3) define the Reynolds number $Re_{p,t=0}$ of a stationary particle at $x_{t=0}, y_{t=0}$ (this is discussed in more detail overleaf) ; (4) integrate the transformed equations of motion, Equations (5.11) and (5.12), using a fourth order Runge-Kutta method; (5) For the general case, C_d is calculated at each time-step.

5.4.3 Methods

G.I. Taylor's 1940 paper was the starting point for this research [22]. The technique described in this paper for the treatment of a particle motion in the case of a jet impinging on a flat plate, summarised above, was implemented on the computer[6] using step-by-step techniques, similar to those used by Glauert [23].

5.4.4 Evaluation of the Drag Force

The drag force is calculated at each time-like z-step and at the intermediate Runge-Kutta stages. When Stokes' law of resistance applies, the numerical solution of Equations (5.11) and (5.12) agrees well with Taylor's exact solution. In the general case where Stokes law does not apply, Equations (5.13) and (5.14) are modified following the procedure outlined in Section 5.3, giving:

$$C_f \frac{d^2x}{dz^2} + \frac{dx}{dz} + \alpha x = 0 \tag{5.13}$$

$$C_f \frac{d^2y}{dz^2} + \frac{dy}{dz} - \alpha y = 0 \tag{5.14}$$

[6] Using the Python scripting language.

with the C_f already defined.

5.4.5 Initial Conditions

Two extreme situations at $t = 0$ were considered: (1) the particle is moving with the flow and (2) the particle is at rest relative to the flow. Solutions were calculated: (i) for the special case when Stokes' law applies, using Equations (5.11) and (5.12) and (ii) for the general case when Stokes' law does not apply, using Equations (5.13) and (5.14).

5.4.6 Evaluation of the Relative Reynolds Number, Re_p

In terms of z, the initial relative Reynolds number of the particle with respect to the flow can be written

$$Re_p = \frac{2aq(z)}{K_0\nu} = \frac{2acq(z)_{z,t=0}}{\alpha\nu}$$

using Equations (5.3) and (5.6). As mentioned, the two extreme initial conditions are (1) the particle is moving with the flow at $z = t = 0$ and (2) the particle is at rest with respect to the flow at $z = t = 0$. For convenience, z and t are taken to be the same quantity in the following discussion; in Taylor's work, the calculations proceed in terms of z and a routine conversion is used to express them in terms of t. Taking initial condition (2) first, the particle is initially at rest and $q_{t=0} = 0$. $q_{t=0}$ is the relative or resultant velocity between the particle and the fluid at $t = 0$. Since α and $q_{t=0}$ are known, setting $Re_{p,t=0}$ to some reasonable value automatically defines a, the radius of the particle (from Equation (5.3) and the definition of K_0). From descriptions in the preceding pages, it can be understood that the definition of α and a automatically set c, the constant of proportionality between the flowspeed and the displacement along the x or y axis; a sets K_0 and α and K_0 together set c. $Re_{p,t=0}$ and α are, it follows, the defining quantities for this analysis. Once these values are set, the calculations can then proceed with C_d recalculated at each

time-step.The Reynolds number at each new time-step $t + \Delta t$ can calculated using $Re_p(t + \Delta t) = q(t + \Delta t)\dfrac{Re_p(t)}{q(t)}$. This arises from the definition of the Reynolds number, i.e. q is the only quantity that varies when a particle of constant size moves through a fluid of constant viscosity.

With initial condition (1), when the particle is moving with the fluid at $t = 0$, a similar consideration applies: if α and Re_p are both specified at $t = 0$, and given that $q(z)_{p,t=0}$ is a function of α only, a and c are automatically defined, again using Equation (5.3) and Section 5.4.1.

This presents a problem, however. At $t = 0$ there is no relative movement between the fragment and the fluid flow and $Re_{p,t=0} = 0$. There is not enough information to allow calculation of Re_p at subsequent time-steps using the procedure outlined above. In order to get around this problem and to kick-start the simulation, the Reynolds number for the same particle standing still relative to the fluid must be defined at $t = 0$; this is an additional input to the simulation. In addition, the initial resultant velocity $q_{t=0}$ between a stationary particle and the fluid is calculated. From the definition of the Re_p on the previous page, it can be seen that knowledge of $Re_{p,t=0}$, $q_{t=0}$ and α automatically defines the product ac, i.e. a measure of the product of particle size and flow velocity. A large $Re_{p,t=0}$ corresponds to a fast flow and/or a large raindrop. Conversely, a small $Re_{p,t=0}$ corresponds to a slow flow and/or a small raindrop. Using these values for $Re_{p,t=0}$ and $q_{t=0}$ allow initialisation of the simulation; calculations for subsequent time-steps are not affected.

5.4.7 Generating the Numerical Grid

A structured numerical grid for the 2D stagnation flow was generated using a simple code which calculated the velocity values u and v at a selected number of points x_0, y_0 to x_N, y_N using the exact solution ($u = -cx$ and $v = cy$). The evenly spaced $N \times N$ grid was written to a text file in the format shown in Table 5.1.

Additional text files were generated with node and element connectivity infor-

Node	x	y	u	v
N_1	0.0	0.0	0.0	0.0
N_2	0.0	1.4	0.0	0.7
N_3	0.0	2.9	0.0	1.4
...				
N_N	0.0	4.3	0.0	2.1

Table 5.1: The format of the structured numerical grid used in the numerical implementation of Taylor's work. N_1 to N_N are the node labels.

mation. For a 4×4 grid, nodes and elements were numbered from the bottom left hand corner to the top right hand corner.

5.4.8 Localisation and Interpolation

Review

Calculating a particle trajectory using Eulerian or Lagrangian methods involves localisation, i.e. finding the particle position x relative to the surrounding grid points. This is straightforward for a *structured cartesian grid*, where the grid is aligned with the reference frame [229]. Locating a particle in *unstructured grids*, however, is generally computationally intensive [229; 233]. Since unstructured grids are increasingly used by computational fluid dynamics codes to mesh complex geometries and since the particle-locating, or *localisation*, algorithm must be performed after each simulation time-step, an efficient algorithm is essential. This is particularly true for simulations of many particles featuring complex flow phenomena such as turbulence [229].

In an Eulerian description of a two-phase flow, the *carrier* velocity and other flow variables are known at a discrete number of grid points. The function of the localisation algorithm is to find the carrier velocity and other relevant flow variables at the particle position [229]. This involves two steps: (i) locating the particle in

the grid, identifying the grid cell that it belongs to at a particular time and (ii) *interpolating* information from the surrounding grid points to calculate the carrier velocity and flow variables of interest at the particle position [229].

Many localisation algorithms have been designed. The simplest general localisation method involves calculating and comparing the Euclidean distance between p and each node in the grid. The fluid $p(x, y)$ is assigned the velocity values of the closest node. This is known as *nearest neighbour interpolation*. Löhner outlines a simple brute-force search algorithm for a single particle in an unstructured grid consisting of either two-dimensional triangular elements or tetrahedral three-dimensional elements using *shape functions*[7] [234]. This technique can be applied to any cell shape by reorganising the cells into triangles or tetrahedra. Due to its simplicity, this algorithm is very fast. In addition, it is readily *vectorised* [8]. Other more advanced search and interpolation techniques are discussed by Zhou [229] and Chodrá [233].

Methods

In order to find the fluid velocities at any point $p(x_p, y_p)$, the point must be located in the numerical grid. Once located, the values for the fluid velocities at the point are estimated using one or more values associated with the surrounding grid points. The first search and interpolate method we used was the simple nearest neighbour scheme where the Euclidean distance between p and each node in the grid is calculated and compared. $p(x, y)$ is assigned the velocity values of the closest node, N_c. The 2D Euclidean separation δ_n is calculated as

$$\delta_n = \sqrt{(x_n - x_p)^2 + (y_n - y_p)^2}$$

[7] In the one-dimensional case, where a cell or element consists of a line joining two points, a and b, a variable u defined at a and b can be interpolated from its value at a and b. The expression is $u = \left(\frac{x_b - x}{x_b - x_a}\right) u_a + \left(\frac{x - x_a}{x_b - x_a}\right) u_b$. The quotients in brackets are referred to as shape functions. Similar expressions can be derived for two-dimensional and three-dimensional elements.

[8] Vectorising allows efficient, parallel operation on vector-like quantities.

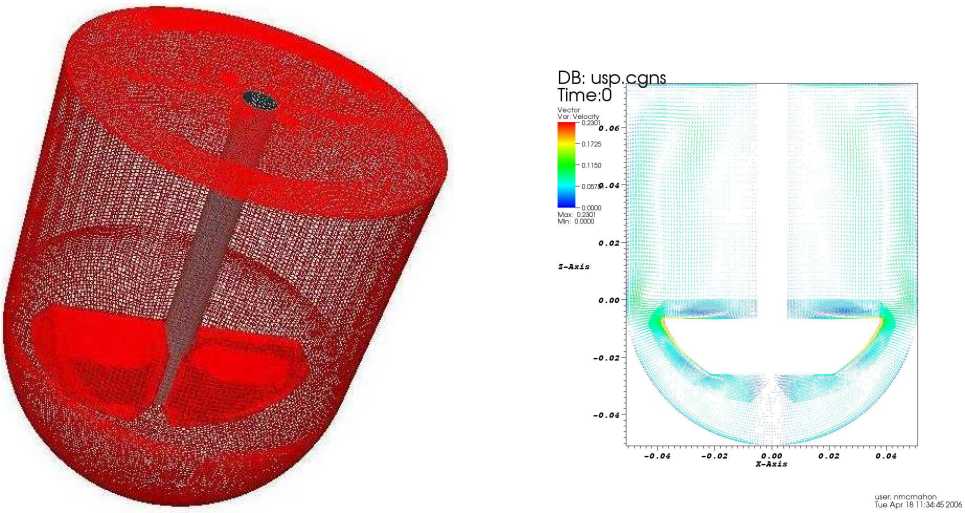

Figure 5.2: USP Dissolution Apparatus 2 generated from CGNS data provided by Deirdre D'Arcy at the School of Pharmacy in Trinity College Dublin [19]. Visualised for this thesis using VisIt [235].

where x_n and y_n are the x and y co-ordinates of the grid point under consideration.

5.5 Particle Motion in the USP Apparatus

The core work presented earlier in this thesis considered the initial drug dissolution from a dissolving compact using numerical techniques, providing good agreement with experimental results for relatively slowly dissolving systems over short dissolution times. One possible end state of a tablet is that, at some stage, it breaks up with dissolution occurring from the disintegrated solid masses. The end-point of the work begun in this thesis is to provide simulations for (i) longer time periods of dissolution and (ii) disintegrating and particulate systems. In addition to some of the techniques already discussed, a first step towards objective (ii) is to examine an existing CFD simulation of the USP apparatus.

5.5.1 USP Apparatus Data

The velocity field within the USP Dissolution Apparatus was produced by D'Arcy et al [19] using the commercial CFD code Fluent. The Fluent model is of the entire USP dissolution apparatus and does not make use of any device symmetries. It is certainly possible that some symmetry considerations could have been used to reduce computation; however, it is understood that the intention was to create a faithful representation of the device. The Fluent hydrodynamic simulation was exported in ASCII and ADF (Advanced Data Format) as specified by the CFD General Notation System (CGNS) [236; 237]. In order to reduce the large ASCII text file to a manageable size for plotting, a Python script was used to thin the data. The script steps through the data file, keeping only every nth line of data [238].

5.5.2 Integration of the Equations of Motion

Numerical integration of ordinary differential equations is concerned with solving *initial value* problems of the form $y' = f(x, y)$, $y(a) = y_0$ over $a \leq x \leq b$. Rather than providing a solution to $y' = f(x, y)$ at every x, numerical methods provide solutions at a finite, preselected set of x values [239], where x is the time-like variable. This results in tables of values for x and y. These tables of values, nowadays calculated by computer and potentially containing a very large amount of data, are generally graphed to facilitate interpretation of the results. Numerical solutions can provide information where algebraic expressions cannot [239].

There are very many integration methods including the (Fundamental) Euler Method or Point Slope Method and its variations, the Trapezoidal Method, the Leap-Frog or Half-Step Method (all linear approximations). Other methods include Adam's Interpolation and Extrapolation methods, the Runge-Kutta Method, Gill's Method, Predictor-Corrector Methods, the Feynman Method and the Verlet Method [see 240; 239; 241; 242]. The Runge-Kutta Method, strictly a family of methods which includes the *Heun Method*, is one of many *multi-stage* algorithms. Multi-stage

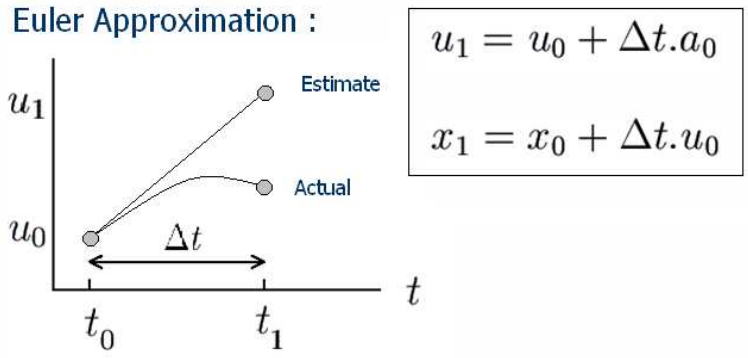

Figure 5.3: The Euler integration method is a simple linear approximation to the particle trajectory. Many time-steps are needed to ensure a basic level of accuracy. x, u and a represent the position, velocity and acceleration values at a point.

methods require calculations at intermediate steps in the time-like sense [243]. Many other methods and variations of existing methods have been devised [244; 242].

Numerical methods should provide accurate and stable solutions that can be performed in a reasonable time with reasonable resources. A series of informative educational papers published in the *American Journal of Physics* provided insight into various integration techniques [241; 244; 245; 246; 247; 248; 242]. Although discussed in detail in many textbooks [e.g. 240; 239], three of the most important methods are described here. Different methods are suitable for different problems; Runge-Kutta methods are commonly used when high accuracy is required. The Verlet method is popular and provides a compromise between accuracy and speed. Euler methods have a low accuracy but are very fast.

Euler or Point Slope Method

The simplest integration method for the solution of $\frac{dy}{dx} = f(x, y)$, $y(x_0) = y_0$ is the linear Point Slope or Euler Method [239]. Given a starting position $P(x_0, y_0)$ and a slope $f(x_0, y_0)$, the aim is to find y_0 ... y_n corresponding to x_0 ... x_n. Taking a tangent through the curve at P_0, the tangent may be a good approximation to the actual curve in a very small interval around x_0, say in the range $x_0 - h$ to $x_0 + h$,

where h is some small value. Moving along the curve from P_0 to P_1, it is possible then to write $x_1 = x_0 + h$ and $y_1 = y_0 + hf(x_0, y_0)$. The Euler Method has a discretisation error $O(h^2)$ for each step in the time-like direction. For the system $u = \frac{dx}{dt} = f(x,t)$, $x(t_0) = x_0$ (Figure 5.3), we can write $x_{n+1} = x_n + u_n \Delta t$. This equation represents a particle's position with time. u in turn can be calculated from the equation $u_{n+1} = u_n + a_n \Delta t$, where a_n is the acceleration at n.

Although attractive for its simplicity, the error accumulates with each step of the time-like direction and quickly becomes significant rendering the solution too inaccurate for use. Other linear algorithms such as the Mid-point Method and the Leap-Frog or Half-Step Method have much better accuracy [241]. It is interesting to note that according to Cromer [241], the superior accuracy of the Leap-Frog Method over the Euler Method is not because it better approximates the first derivative at a point, but because it better approximates the *first integral of motion*.

Runge-Kutta Methods

As outlined in textbooks [e.g. 240; 239], one particular Runge-Kutta method consists of four intermediate calculations to solve for y in $y' = f(x,y)$. The solution is:

$$y_{n+1} = y_n + \frac{1}{6}k_1 + \frac{1}{3}k_2 + \frac{1}{3}k_3 + \frac{1}{6}k_4 + O(h^5) \tag{5.15}$$

Where values are as defined previously and $k_1 = hf(x_n, y_n)$, $k_2 = hf(x_n + \frac{1}{2}h, y_n + \frac{1}{2}k_1)$, $k_3 = hf(x_n + \frac{1}{2}h, y_n + \frac{1}{2}k_2)$ and $k_4 = hf(x_n + h, y_n + k_3)$.

Runge-Kutta methods, although accurate, incur calculation and storage penalties, requiring calculation of the variables at intermediate positions between steps in the time-like direction and can result in a computationally expensive program [249]. Nevertheless, Runge-Kutta methods are widely used [e.g. 250; 251; 252].

Verlet Method

The Verlet method was used by Loup Verlet in his 1967 paper on the motion of particles under the influence of molecular forces [110]. The Verlet algorithm and its variants are widely used in physics engines where high-speed calculation is necessary. Verlet solves $m\frac{d^2r_i}{dt^2} = \sum_{j\neq i} f(r_{i,j})$ using:

$$r_i(t+h) = 2r_i(t) - r_i(t-h) + \sum_{j\neq i} f(r_{i,j}(t))h^2 \tag{5.16}$$

where h is a small time increment. The Verlet algorithm is derived by combining two Taylor series expansions. With r the position, v the velocities, a the accelerations, and b the third derivatives of r with respect to t, all vector quantities, we can write:

$$r(t+\Delta t) = r(t) + v(t)\Delta t + ... + a(t)\Delta t^2 + (1/6)b(t)\Delta t^3 + O(\Delta t^4) \tag{5.17}$$

$$r(t-\Delta t) = r(t) - v(t)\Delta t + ... + a(t)\Delta t^2 - (1/6)b(t)\Delta t^3 + O(\Delta t^4) \tag{5.18}$$

Adding Equations (5.17) and (5.18) gives

$$r(t+\Delta t) = 2r(t) - r(t-\Delta t) + 2a(t)\Delta t^2 + O(\Delta t^4)$$

Which is the method proposed by Verlet. The Verlet algorithm is accurate, formally of $O(\Delta t^4)$ though no third derivatives are explicitly required. It is simple to implement and is popular. Velocity values can be calculated using

$$v(t) = \frac{r(t+\Delta t) - r(t-\Delta t)}{2\Delta t} + O(\Delta t^2)$$

The disadvantage of this is that the error in the velocity values are $O(\Delta t^2)$ rather than $O(\Delta t^4)$. Swope et al. showed that the velocity values at the new time-step can be explicitly calculated with a higher accuracy by re-writing the algorithm in an equivalent form [253], yielding:

$$r(t + \Delta t) = r(t) + v(t)\Delta t + \frac{1}{2}a(t)\Delta t^2 \tag{5.19}$$

$$v(t + \Delta t) = v(t) - \frac{1}{2}\big(f(t + \Delta t) + f(t)\big)\Delta t \tag{5.20}$$

However, this requires knowledge of the force or accelerations at $t + \Delta t$ *before* calculation of the velocities at $t + \Delta t$, i.e. the forces acting on the body must be known at $t + \Delta t$.

5.6 Preliminary Analysis of Particle Motion in the USP Apparatus

5.6.1 Typical Particle Size

Assuming Stokes flow, the drag force (F_d) on a sphere can be written $F_d = 6\pi\mu a U$, or $\frac{F_d}{\mu a U} = 6\pi = \text{const.}$ [114]. The momentum of a particle is written as $p = \frac{4}{3}\pi a^3 \rho_p U$. Since $F = ma$, we can write $F \approx \frac{p}{t}$, or $t \approx \frac{\frac{4}{3}\pi a^3 \rho_p U}{F}$ or $t \approx \frac{\frac{4}{3}\pi a^3 \rho_p U}{6\pi\mu a U} = \frac{2a^2}{9\nu}$. Taking the time to destroy the momentum of a particle as being about 1 second and the kinematic viscosity of the fluid to be that of the solvent, 0.1M HCl at 37^o, i.e. $\nu = 0.0078\dot{6} \approx 10^{-2}$ cm^2 s^{-1}, then $1 \approx 100a^2$ or $a \approx 0.1$ cm. The important parameter in this approximation is the time taken for a particle initially at rest to achieve the same velocity as the fluid, i.e. 1 second in the estimate presented.

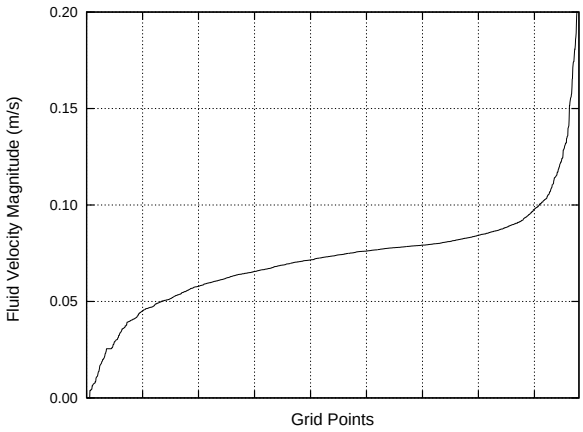

Figure 5.4: Fluid velocity magnitudes encountered within the USP Dissolution Apparatus 2. As can be clearly seen, velocities are distributed mostly between 5 cm s^{-1} and 10 cm s^{-1}. The average fluid velocity magnitude within the device is about 7.2 cm s^{-1}.

5.6.2 Maximum Fluid Velocities

With a paddle speed of about 50 revolutions per minute, or $\frac{5}{6}$ revolutions per second, the maximum tangential speed for fixed body rotation at the edges of the device will be $\frac{5}{6} \times 2\pi r = 31.4$ cm s^{-1}. For a particle at rest with respect to the device, the maximum relative velocity will therefore be 31.4 cm s^{-1}.

5.6.3 Maximum Relative Reynolds Number, Re_p

With $q_{\max} = 31.4$ cm $s^{-}1$, $a = 0.05$ cm and $\nu = 0.00787 \approx 10^{-2}$ cm^2 s^{-1}, $Re_p = \frac{2aq_{\max}}{\nu} = \frac{31.4 \times 0.1}{10^{-2}} \approx 800$. With $q = 1.83$ cm s^{-1}, taken from previous studies [17], $Re_p \approx 46$. The average fluid velocity magnitude within the device is about 7.2 cm s^{-1} (Figure 5.4), giving $Re_p = \frac{7.2 \times 0.1}{0.00787} \approx 91.4$.

5.6.4 Effect of Discrete Velocity Field Density on the Relative Reynolds Number, Re_p

The original discrete velocity fields, produced by D'Arcy et al [19], were processed to produce several additional files containing subsets of the original data. These subsets

represent a "thinning" of the original data set. The original data file contains some 1,759,974 lines of information, each line corresponding to a discrete spatial node or data point. The USP apparatus is of overall height $h = 126$ mm and diameter $2r = 101.6$ mm. Considering the USP apparatus as consisting of two parts, a cylinder of height 75.5 mm and radius 50.8 mm and a hemisphere of radius 50.8 mm, we can calculate the total volume of the device, V_T.

Assuming that the nodes are distributed evenly in this space, we can say that the average size of volumetric element is $V_N = \frac{V_T}{N}$, where N is the total number of nodes. Further, we can say that the average span between adjacent nodes is $x_N = V_N^{\frac{1}{3}}$. That is, with $V_T = 1,307.4$ cm^3, we can say that $V_N = 0.000743$ cm^3 and that the average spacing between nodes in the original high-density grid is $x_N = 0.091$ cm. The two other grids generated have 100 and 1,000 times fewer nodes, i.e. grid 2 has 17,600 nodes and grid 3 has 1,760 nodes. These correspond to an average node spacing of 0.42 cm and 0.91 cm respectively.

Although attractive for its simplicity, a major problem with forcing a particle to a grid node after each time-step is that if the absolute particle velocity falls below a minimum required $v_{p,\min}$ (Table 5.2), then an artificial velocity term will be introduced, i.e. a particle violating $\Delta t < \frac{\bar{v_p}}{h}$ will jump through the grid at an artifical velocity (see Table 5.2). In fact, as the timestep is reduced, the apparent speed of such a particle relative to the grid will increase quickly to hundreds of centimetres per second.

Conversely, if the time-step is too large, then the particle will have moved too far for any sensible prediction to be made of its motion within the device, e.g. a linear estimate of the new position of a particle moving at 30 cm s^{-1} will place the particle well outside the walls of the device. The nearest neighbour algorithm will then position the particle at the nearest node inside the device.

A nearest-neighbour algorithm can be used to set fluid and particle velocities at a point but not to force the re-positioning of the particle at each time-step to the

Δt (s)	$v_{p,\min}$ (M1) (cm s^{-1})	$v_{p,\min}$ (M2) (cm s^{-1})	$v_{p,\min}$ (M3) (cm s^{-1})
1	0.09	0.42	0.91
0.1	0.91	4.20	9.06
0.01	9.06	42.00	90.57
0.001	90.57	420.00	905.67

Table 5.2: Minimum absolute particle velocities v_p with respect to the USP apparatus required for three different grids when the particle is forced to a grid node after each timestep. If the velocity per time-step falls below the minimum value, an artificial velocity term will be introduced. Velocities are calculated by dividing the average span between grid points by the time-step. Mesh 1 (M1) has 1,760,000 grid points with an average spacing of ≈ 0.0906 cm. Mesh 2 has 17,600 grid points with an average spacing of ≈ 0.420 cm. Mesh 3 has 1,760 grid points with an average spacing of ≈ 0.906 cm.

nearest node.

5.6.5 Mass Transfer from a Particle in the USP Apparatus

Mass transfer from a spherical particle moving through a fluid can be calculated using empirical correlations relating experimental data to important parameters. Numerous correlations have been proposed for heat and mass transfer from the surface of a sphere [e.g. 254; 255; 256; 257; 102].

$S\bar{h}_p$ is the average *Sherwood Number* of a particle [254; 102], defined as

$$S\bar{h}_p = \frac{2a\bar{h_m}}{D} \tag{5.21}$$

where $\bar{h_m}$ is the average mass transfer film coefficient (or the convection mass transfer coefficient), a is the radius of the sphere, or particle, and D is the diffusivity. $S\bar{h}_p$ can be considered as the dimensionless concentration gradient at the surface; this can be demonstrated by considering Fick's law expressed in terms of $\bar{h_m}$ [102],

$$\frac{\partial C}{\partial y} = \frac{\bar{h_m}}{D}(C_s - C_\infty) \tag{5.22}$$

Sink conditions pertain, since it is assumed that the initial particle weight is less than 10 % of the amount of solute necessary to saturate the solution [88], so $C_\infty \approx 0$, and

$$\frac{\partial C}{\partial y} = \frac{\bar{h_m}}{D}(C_s) \tag{5.23}$$

Non-dimensionalising this equation by multiplying $\frac{\partial C}{\partial y}$ by $\frac{2a}{C_s}$ yields,

$$\frac{\partial c'}{\partial y'} = \frac{2a\bar{h_m}}{D} \tag{5.24}$$

where $\frac{\partial c'}{\partial y'}$ is the dimensionless concentration gradient at the surface and, as previously shown, the group $\frac{2a\bar{h_m}}{D}$ is the average Sherwood number. When $S\bar{h}_p$ is known, a value for the mass transfer from a particle in a fluid can be calculated by writing

$$\bar{h_m} = -\frac{D_{AB}}{2a} S\bar{h}_p \tag{5.25}$$

Since the average mass flux of solute per unit surface area of the sphere is given by

$$m'' = -\bar{h_m} C_s \tag{5.26}$$

assuming sink conditions, the mass transfer rate from a spherical particle of radius a can is then calculated as

$$\dot{m} = -4\pi a^2 \bar{h_m} C_s = -2a\pi D_{AB} S\bar{h}_p C_s \tag{5.27}$$

The Sherwood number of, and hence mass transfer from, a spherical particle is a function of three main processes, (i) radial diffusion, (ii) free or natural convection and (iii) forced convection. These processes are linked to the Schmidt number (Sc),

Grashof number (G') and Reynolds number (Re_p) respectively. Sc and Re_p are well known[9]. The Grashof number, G', can be considered as the free convection equivalent of the Reynolds number, and is a measure of the ratio of the inertial forces to the buoyancy forces [254; 102]. G' is defined as

$$G' = \frac{8ga^3}{\nu^2}\frac{\Delta\rho}{\rho} \tag{5.28}$$

where g is acceleration due to gravity, a is the radius of the particle, ν is the kinematic viscosity of the solvent, ρ is the bulk density of the pure solvent and $\Delta\rho$ is the difference between the density of the saturated solution and the bulk density.

For the problem under consideration, $g = 980$ cm s^{-2}, a varies with particle size, and the properties of pure 0.1M hydrochloric acid (HCl) are $\nu = 7.87 \times 10^{-3}$ cm^2 s^{-1}, $\rho = 1.19$ g cm^{-3}. D'arcy et al. arrived at an experimental value for $\Delta\rho$ of 1.99 kg m^{-3} or 1.99×10^{-3} g cm^{-3} [258]. Other relevant quantities include the saturation concentration of benzoic acid in HCl, $C_s = 4.55 \times 10^{-3}$ g cm^{-3} and the diffusivity $D = 1.236 \times 10^{-5}$ cm^2 s^{-1}. The Schmidt number, $Sc = \dfrac{\nu}{D} = 636.7$.

Using these values, together with the average relative Reynolds numbers, $\bar{Re}_p$, calculated for particles of various sizes moving through the USP apparatus, we can determine G'. Experimental correlations are chosen to relate $S\bar{h}_p$ to these three numbers. Once $S\bar{h}_p$ is known, the average mass transfer rate $\dot{m}$ can be calculated

Garner [254] and Miller [257] provide reviews of useful experimental correlations although more recent studies also exist. Well-known correlations include those of Ranz and Marshall and Harriott [255; 256]. Incropera and DeWitt recommend a heat transfer correlation proposed by Whitaker in 1972 [102]. The work presented here uses four recommended correlations, two each from Garner and Miller for free and forced convection respectively. $S\bar{h}_p = 2$ corresponds to mass transfer by radial diffusion only and represents the lower limit of $S\bar{h}_p$ [254].

These correlations are: (1) Garner's free convection correlation,

[9]See the Glossary for brief descriptions.

$$S\bar{h}_p = 0.50(G'Sc)^{0.25} \tag{5.29}$$

for $G'Sc \leq 10^5$. (2) Garner's forced convection correlation,

$$S\bar{h}_p = 0.50(G'Sc)^{0.25} + 0.48Re_p^{0.5}Sc^{0.33} \tag{5.30}$$

again for $G'Sc \leq 10^5$. (3) Miller's free convection correlation,

$$S\bar{h}_p = 2 + 0.60G'^{0.25}Sc^{0.25} \tag{5.31}$$

(4) Miller's forced convection correlation,

$$S\bar{h}_p = 2 + 1.10Re_p^{0.5}Sc^{0.33} \tag{5.32}$$

Using these correlations, $\bar{h_m}$ can be calculated as described previously, i.e. $\dot{m} = -2a\pi D_{AB}Sh_pC_s$.

Miller's 1971 paper is a very useful review of mass transfer correlations for suspended solute particles dissolving in an agitated vessel [257]. Importantly, Miller reports that *radial diffusion* is the dominant mode of mass transfer for particles of diameter 205 microns and less, based on data presented by Harriott in his 1962 work [255]. This figure was arrived at by considering the *turbulence microscale* measure η which represents the size of the smallest turbulent eddies expected in a particular system configuration. As discussed by Miller, η (as defined by Shinnar and Church an earlier 1960 paper) is given as:

$$\eta = 0.1983(P/V')^{-\frac{1}{4}}\nu^{\frac{3}{4}} \tag{5.33}$$

where P is the agitator power input and V' is the volume of the device. Eddies at the small eddy equilibrium end of the turbulence energy spectrum are most important for mass transfer [257].

5.6.6 Visualisation of Results

With the development of CFD, the visualisation of the complex data produced by these codes has become increasingly important. Visualisation greatly facilitates the interpretation of complex data, revealing underlying patterns and structures [259]. All the information presented graphically in this thesis is visualised using GnuPlot [189], VisIt [235], Fluent [106] or ADFViewer [260]. GnuPlot, the standard Unix/Linux tool, was used to produce most of the two-dimensional plots while Fluent, ADFViewer and VisIt were used to visualise the commercial CFD code data.

5.7 Chapter Summary and Conclusions

This chapter introduced the literature, theory and methods associated with the third study that contributes to this thesis, the dissolution of a drug particle moving in the USP apparatus. This included a review of the classical work of Taylor and Glauert, who calculated analytical and numerical solutions to the motion of raindrops in curved airstreams. The governing equations for, and an overview of the numerical methods involved in, the calculation of particle motion in the USP apparatus were described. The chapter finishes with some preliminary ideas about expected particle motion and a review of experimental mass transfer correlations. The utility of the methods presented here and their relevance to the thesis, that simulation is useful for pharmaceutics, is discussed in Chapter 8. Chapter 6 continues with results, and discussion, about the first of the three studies described.

Chapter 6

Results and Discussion, Study 1

In this chapter we present results from the core investigations presented in this thesis, i.e. the initial dissolution rate from a tablet dissolving in the USP apparatus. The significance of these results, as well as their context in the overall thesis, is discussed.

6.1 Investigations of Previous Work

6.1.1 The Pohlhausen Solution

As discussed previously, Crane et al. [17] describe a semi-analytical procedure for calculating the release rate of drug, $\dot{m}$, from a cylindrical tablet that consists of alternating layers of drug and excipient, concluding with several expressions that can be used to get solutions for tablets consisting, in total, of 3 and 5 layers. Two questions immediately come to mind: (1) can these expressions be generalised to deal with any number of layers and (2) what happens when the number of layers is very large? Does the drug release rate as predicted by Crane et al. tend to a limiting value?

Generalising to Many Layers

Considering the expression given by Crane et al. for the ratio of the mass transfer of an excipient from a 3-layer compact ($\dot{m}_{\text{e-3-layer}}$) to the mass transfer from a compact consisting entirely of the excipient ($\dot{m}_{\text{e-1-layer}}$),

$$\frac{\dot{m}_{\text{e-3-layer}}}{\dot{m}_{\text{e-1-layer}}} = \left[1 - \left(\frac{x_2}{x_3}\right)^{\frac{3}{4}} + \left(\frac{x_1}{x_3}\right)^{\frac{3}{4}}\right]^{\frac{2}{3}} \tag{6.1}$$

where x_1, x_2 and x_3 are defined for 1-/3-layer systems in Figure 3.1, it becomes evident that, for the case of a compact consisting of 3 equally-spaced layers, one drug layer sandwiched between two layers of excipient, we can replace this equation with the equivalent expression

$$\frac{\dot{m}_{\text{e-3-layer}}}{\dot{m}_{\text{e-1-layer}}} = \left[\sum_{n=0}^{2}\left(\frac{3-n}{3}\right)^{\frac{3}{4}}(-1)^n\right]^{\frac{2}{3}} \tag{6.2}$$

Likewise, and for the same condition of 3 equally-spaced and alternating layers, its complement, the ratio of the mass transfer of a drug from a 3-layer compact ($\dot{m}_{\text{d-3-layer}}$) to the mass transfer from a compact consisting entirely of the drug ($\dot{m}_{\text{d-1-layer}}$) can be written as

$$\frac{\dot{m}_{\text{d-3-layer}}}{\dot{m}_{\text{d-1-layer}}} = \left[1 - \sum_{n=0}^{2}\left(\frac{3-n}{3}\right)^{\frac{3}{4}}(-1)^n\right]^{\frac{2}{3}} \tag{6.3}$$

Similarly for the case of five equally spaced and alternating layers of drug and excipient, two drug layers sandwiched between three layers of excipient

$$\frac{\dot{m}_{\text{e-5-layer}}}{\dot{m}_{\text{e-1-layer}}} = \left[\sum_{n=0}^{4}\left(\frac{5-n}{5}\right)^{\frac{3}{4}}(-1)^n\right]^{\frac{2}{3}} \tag{6.4}$$

$$\frac{\dot{m}_{\text{d-5-layer}}}{\dot{m}_{\text{d-1-layer}}} = \left[1 - \sum_{n=0}^{4}\left(\frac{5-n}{5}\right)^{\frac{3}{4}}(-1)^n\right]^{\frac{2}{3}} \tag{6.5}$$

We can at this point easily generalise these observations to an odd number, p,

of equally-spaced, alternating, layers of drug and excipient with the drug layers sandwiched between the layers of excipient:

$$\frac{\dot{m}_{\text{e-}p\text{-layer}}}{\dot{m}_{\text{e-1-layer}}} = \left[\sum_{n=0}^{p-1}\left(\frac{p-n}{p}\right)^{i}(-1)^{n}\right]^{\frac{2}{3}} \tag{6.6}$$

$$\frac{\dot{m}_{\text{d-}p\text{-layer}}}{\dot{m}_{\text{d-1-layer}}} = \left[1-\sum_{n=0}^{p-1}\left(\frac{p-n}{p}\right)^{i}(-1)^{n}\right]^{\frac{2}{3}} \tag{6.7}$$

where i is the index, evaluated as $\frac{3}{4}$ [17]. These equations represent an extension of the work of Crane et al [17]. We explicitly state the general case that their results imply.

The Case When the Number of Layers is Large

It can be readily demonstrated that the series appearing in Equation (6.6) converges to a fixed value as $p \to \infty$ for the case of $i = 1$. When $i = 1$, the series can be written as $-\frac{0}{p}+\frac{1}{p}-\frac{2}{p}+\frac{3}{p}-\frac{4}{p}+\frac{5}{p}\ ...\ \frac{p}{p}$. Pairing the terms as follows, $\left(-\frac{0}{p}+\frac{1}{p}\right)+\left(-\frac{2}{p}+\frac{3}{p}\right)+\left(-\frac{4}{p}+\frac{5}{p}\right)+\ ...\ +\left(-\frac{(p-1)}{p}+\frac{5}{p}\right)$, it is evident that the sum of these pairs is always $\frac{1}{p}$. Since there are $\frac{(p+1)}{2}$ differences, the series sums to $\frac{1}{p}\times\frac{(p+1)}{2}=\frac{1}{2}+\frac{1}{2p}$.

As p becomes large, $\frac{1}{2p}$ becomes small and the sum of the series converges to $\frac{1}{2}$. The question now becomes, what is the behaviour of Equation (6.6) as $p \to \infty$ for positive values of i other than 1? Taking the case when i is an integer, $i \in \mathbb{Z}$, we can write that $\sum_{n=0}^{p-1}\left(\frac{p-n}{p}\right)^{i}(-1)^{n} = \frac{1}{p^{i}}\left[p^{i}-(p-1)^{i}+(p-2)^{i}-(p-3)^{i}+\ ...\ \right]$. Since $x^{i}-y^{i}=(x-y)(x^{i}+x^{i-2}y+\ ...\ +y^{i})$ and if we group the terms in pairs, denoted as $2n$ and $2n-1$ where $n = 1, \ ...\ , \frac{p}{2}$, we can re-write this series as

$$\sum_{n=0}^{p-1}\left(\frac{p-n}{p}\right)^{i}(-1)^{n}=$$
$$\frac{1}{p^{i}}\sum_{n=0}^{\frac{p}{2}}\big(2n-(2n-1)\big)\big((2n^{i-1})+2n^{i-2}(2n-1)+...+(2n-1)^{i-1}\big)$$

Since $2n-(2n-1)=1$,

$$\begin{aligned}\sum_{n=0}^{p-1}\left(\frac{p-n}{p}\right)^{i}(-1)^{n}=&\frac{1}{p^{i}}\sum_{n=1}^{\frac{p}{2}}1.\big(i(2n)^{i-1}+\text{terms with power } i-2 \text{ or less}\big)\\ =&\frac{1}{p^{i}}\sum_{n=1}^{\frac{p}{2}}\big(i(2^{i-1})n^{i-1}+\text{terms with power } i-2 \text{ or less}\big)\\ =&\frac{1}{p^{i}}i2^{i-1}\sum_{n=1}^{\frac{p}{2}}\big((n^{i-1})+\text{terms with power } i-2 \text{ or less}\big)\end{aligned}$$

Using the identity $\sum_{k=1}^{n}k^{\Gamma}=\frac{n^{\Gamma+1}}{\Gamma+1}+(\text{terms with powers less than } \Gamma+1)$, we can write

$$\begin{aligned}\sum_{n=0}^{p-1}\left(\frac{p-n}{p}\right)^{i}(-1)^{n}=&\frac{1}{p^{i}}i2^{i-1}\left(\frac{p^{i}}{i2^{i}}+\text{terms with power } i-1 \text{ or less}\right)\\ =&\frac{1}{2}+\left(\text{terms that are functions of } \frac{1}{p}\right)\\ =&\frac{1}{2} \text{ as } p\to\infty\end{aligned}$$

The next step is to investigate the behaviour of Equation (6.6) as $p\to\infty$ for positive values of i other than $i\in\mathbb{Z}$, i.e. for i a rational number, $i\in\mathbb{Q}$. Using numerical experiments, it is clear that as p gets very large the sum of the series approaches $\frac{1}{2}$ for all $i>0$ (Table 6.1). In addition, the ratio of the mass transfer

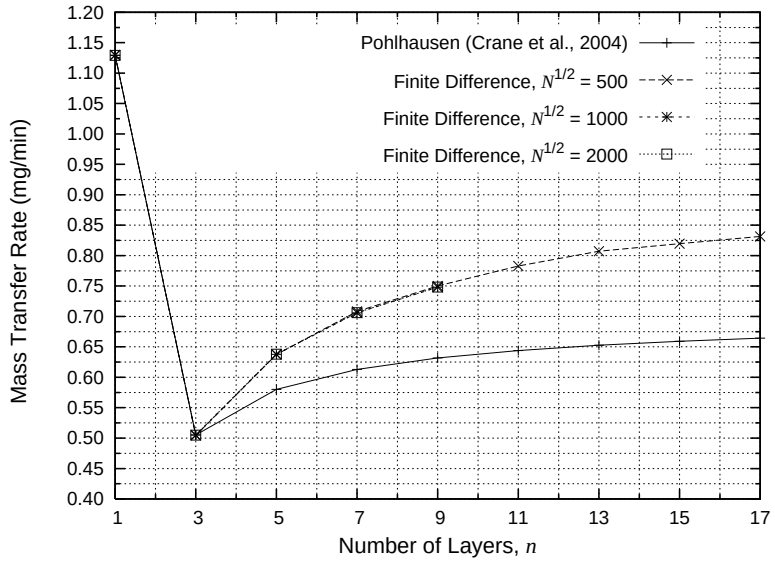

Figure 6.1: Mass transfer values calculated using the semi-analytical Pohlhausen method [21] and the numerical finite difference method presented in this thesis [261].

of a drug from a p-layer compact ($\dot{m}_{\text{d-5-layer}}$) to the mass transfer from a compact consisting entirely of the drug ($\dot{m}_{\text{d-1-layer}}$) tends to $\left(\frac{1}{2}\right)^{\frac{2}{3}} = 0.63$ for all $i > 0$ as p gets very large (see also Figure 6.1). Following the method proposed by Crane et al [17], a tablet consisting of a very large number of alternating layers of drug and excipient will have an (initial) mass transfer rate of drug equivalent to 63% of the initial mass transfer rate of drug from a tablet that consists entirely of drug.

It is interesting to speculate on the possible applications of this solution. A tablet containing a very large number of alternating layers of drug and excipient may have similar initial dissolution properties to the more common type of dissolution controlled tablet where small particles of drug and excipient are intermixed.

6.1.2 The PSUDO Solutions

The Effect of Advection Velocities on Mass Transfer Rates

As discussed in Chapter 2, the models used in the PSUDO project consistently overestimate the mass transfer rate of drug from a layered compact [20]. The authors

	i	0.25	0.75	1	2	3	4
p							
3		0.8562	0.7009	0.6667	0.6667	0.7407	0.8148
5		0.8078	0.6319	0.6000	0.6000	0.6480	0.6960
101		0.6400	0.5118	0.5050	0.5050	0.5074	0.5099
1,001		0.5786	0.5020	0.5005	0.5005	0.5007	0.5010
10,001		0.5442	0.5003	0.5000	0.5000	0.5001	0.5001
100,001		0.5248	0.5001	0.5000	0.5000	0.5000	0.5000
1,000,001		0.5140	0.5000	0.5000	0.5000	0.5000	0.5000
10,000,001		0.5079	0.5000	0.5000	0.5000	0.5000	0.5000
100,000,001		0.5044	0.5000	0.5000	0.5000	0.5000	0.5000
1,000,000,001		0.5025	0.5000	0.5000	0.5000	0.5000	0.5000

Table 6.1: Numerical investigation into the convergence of $\sum_{n=0}^{p-1} \left(\frac{p-n}{p}\right)^i (-1)^n$ for $i \in \mathbb{Q}$ as p becomes large.

attribute this to the fact that mixing in the bulk fluid is neglected, so drug is not drawn away from the surface sufficiently quickly. From examination of the literature, it seems likely that the reasons for this overestimate are (1) the use of a constant advection velocity v_z in the boundary-layer region and (2) neglecting the normal velocity v_n.

In order to test these ideas and to ascertain the impact of these simplifications, the Crank-Nicolson finite difference scheme was used to calculate the mass transfer rate from tablets with a constant horizontal and vertical fluid velocity imposed across the region of interest (i.e. the velocity boundary-layer was ignored). It is clear from Table 6.2 that assuming a constant horizontal advection velocity v_z throughout the diffusion layer introduces a significant error into the calculation. In fact, the mass transfer from a surface can be overestimated by more than a factor of 5. Neglecting advection normal to the surface also introduces a smaller, but noticeable, error (See Table 6.2). One direct result of the over-estimated fluid velocity close to the surface is that the concentration boundary-layer will tend to stay close to the surface with time. In addition, as noted in the report, the drug release profile will plateau much too early.

		$\dot{m}$		
Compact Type	u_l, v_l	$u_l, 0$	U, v_l	$U, 0$
[BA] **1-Layer**	**1.13 (-)**	0.71 (0.63)	5.76 (5.11)	5.72 (5.08)
[-/BA/-] **3-Layer**	**0.51 (-)**	0.43 (0.86)	3.40 (6.73)	3.39 (6.72)
[-/BA/-/BA/-] **5-Layer**	**0.64 (-)**	0.49 (0.76)	4.10 (6.43)	4.09 (6.41)

Table 6.2: Mass transfer rates (mg min^{-1}), calculated using finite differences, from 1/3/5-Layer compacts dissolving in a type 2 USP dissolution test apparatus for various u, v ($cm\ s^{-1}$). u and v are the horizontal and normal velocity components of the flow within the concentration boundary-layer respectively. U is the freestream fluid velocity, in this instance 1.83 $cm\ s^{-1}$. u_l and v_l are the velocity components calculated using Kestin and Persen's velocity approximation. Throughout this thesis, u_l and v_l are synonymous with u and v but for the purpose of clarity in this table, the difference is explicitly highlighted. Errors are expressed as a factor of the corresponding u_l, v_l result and listed in brackets.

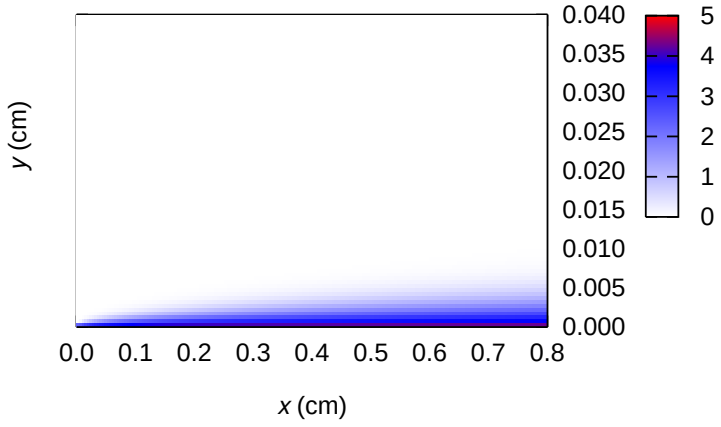

Figure 6.2: Visualisation of the concentration boundary-layer above the surface of a 1-layer tablet, generated using the first method described in the PSUDO project with a constant advection velocity $U = 1.83$ cm s^{-1}. The scale 0-5 is the drug concentration in mg cm^{-3}.

In the visualisation of the concentration boundary-layer above the surface of a 1-layer tablet shown in Figure 6.2, the fluid is moving from left to right and the surface of the tablet forms the bottom axis of the graph. The visualisation is generated using the first method described in the PSUDO project with a constant advection velocity $U = 1.83$ cm s^{-1}. The normal velocity component is neglected. The resulting high mass transfer rate of 9.53×10^{-5} g s^{-1} (or 5.72 mg min^{-1}) is vividly apparent in the thin concentration boundary-layer.

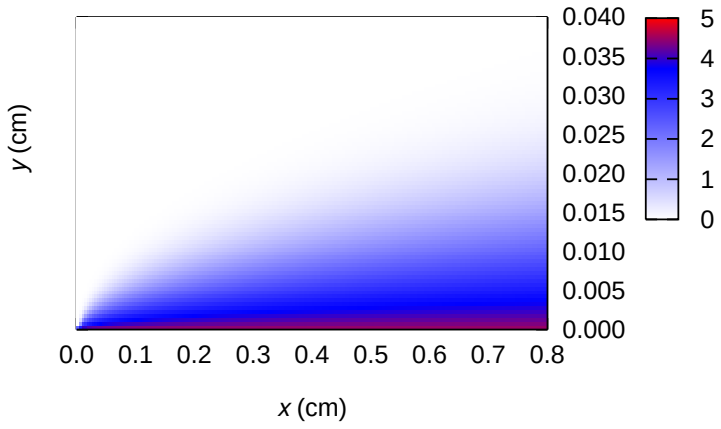

Figure 6.3: Visualisation of results from the finite difference scheme outlined in this thesis with a freestream velocity of $U = 1.83$ cm s^{-1}. u and v close to the surface are calculated using the velocity boundary-layer equations.

The second visualisation (Figure 6.3) was generated using the finite difference method presented in this thesis with a freestream velocity of $U = 1.83$ cm s^{-1} [261]. The velocity components close to the surface are calculated in accordance with boundary-layer theory. The resulting mass transfer rate of 1.13 mg min^{-1} is consistent with analytical solutions and experiment presented later in this chapter. The concentration boundary-layer can be seen to be obviously thicker due to the lower velocities very close to the surface.

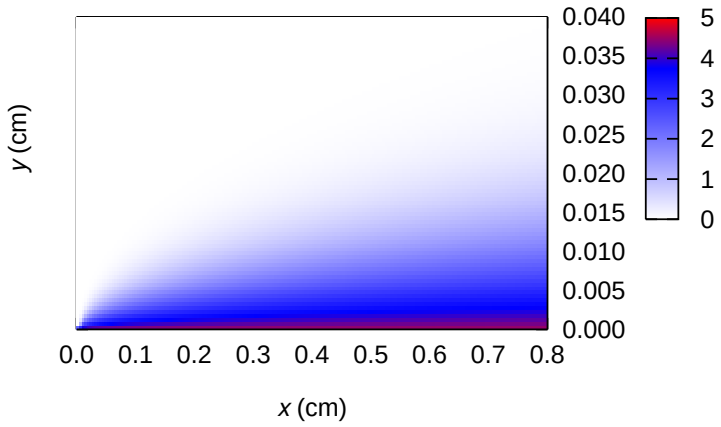

Figure 6.4: Visualisation of results using the first method described in the PSUDO project with a constant advection velocity $U = 0.12$ cm s^{-1}.

In order to match experimental values for mass transfer from a 1-layer compact (1.46 mg min^{-1} [104]), the first method described in the PSUDO project [20] must be used with a constant advection velocity $U = 0.12$ cm s^{-1}. The concentration boundary-layer in this case is visually similar to that produced by the finite difference scheme using a free-stream velocity of 1.83 cm s^{-1}. This agrees with and explains the observations of the PSUDO project [20], which indicate that an exceptionally low advection velocity is required to achieve experimental mass transfer rates.

Much of the error in the PSUDO results is due to two assumptions: (1) constant v_z and (2) neglecting convective transfer perpendicular to the surface. Using a fixed advection velocity leads to an overestimated mass transfer rate from the surface.

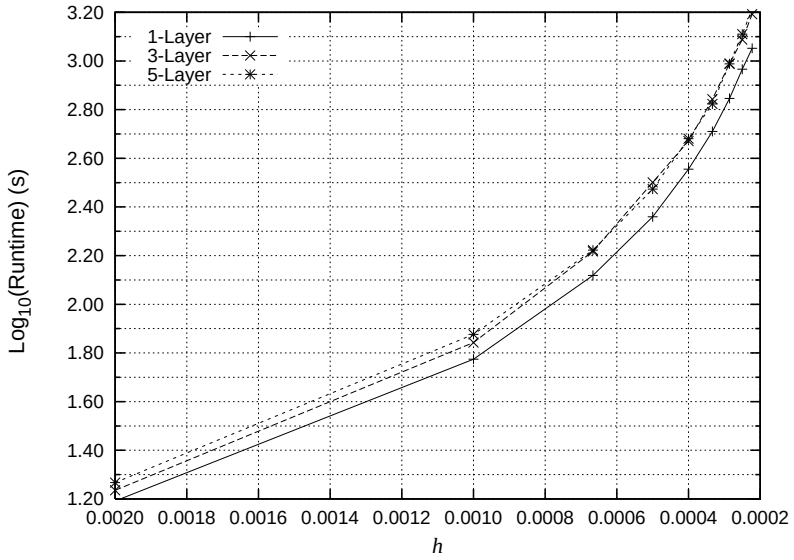

Figure 6.5: Finite difference P4 2.4GHz 500MB RAM program runtimes with decreasing representative cell size, h.

6.2 Numerical Results

6.2.1 Verification of the Scheme

A grid sensitivity analysis [144] (Table 6.3) indicated that the 5-layer finite difference model converges as $h \to 0$ with a discretisation error of 0.02 % (Table 6.4). The 1-layer finite difference scheme converges linearly with decreasing h, i.e. as follows , as does the 5-layer scheme, i.e. as follows . The 3-layer scheme, however, displays an oscillatory convergence, i.e. . These analyses give us further confidence that the Crank-Nicolson finite difference scheme is solving the equations correctly.

The finite difference program runtime can be defined as $t_c = \beta h^2$ where t_c is the computation time and β is a constant. $t_{c_{h=0.001}} = 75$ s (implemented with Python on a 2.4 GHz P4, 512 MB RAM) where h is the cell size, defined earlier. So t_c is a simple function of the square of the cell size or a linear function of the number of cells in the grid (Figure 6.5).

6.2.2 The Effect of Discontinuities

Leading Edge Velocity Singularity

For a 1-layer tablet of benzoic acid, the mass transfer rate $\dot{m}$ calculated using the finite difference scheme is 1.1259 mg min^{-1} corrected for the velocity singularity at the leading edge. The relative error with respect to the experimental value of 1.46 mg min^{-1} [104] is 22.9% (Table 6.5). The mass transfer rates calculated without a correction for the velocity singularity is 1.1299 mg min^{-1} (the singular values at the leading edge were simply omitted). This has a 22.6% error with respect to experiment and a 0.36% error with respect to the corrected solution. It is interesting to note that the error between the corrected and uncorrected finite difference solutions is small and that the uncorrected solution is still within 0.1% of the Kestin-Persen analytical solution.

Crank-Nicolson Oscillations

As illustrated in Figure 6.6 a-f, our solution features discontinuities in the normal first derivative of concentration at the edges of the diffusing regions. The calculated $\left.\frac{\partial c}{\partial y}\right|_{y=0}$ oscillates in the streamwise direction, from left to right. This is a typical response of the Crank-Nicolson scheme to sharp initial transients (the x or streamwise direction is the time-like variable in our simulation) [157; 262; 198]. Although the oscillations in $\left.\frac{\partial c}{\partial y}\right|_{y=0}$ clearly persist over the length of the diffusing regions (Figure 6.6 a-f), they are damped and are relatively small at the end of each of the regions. In addition, as is evident in Figures 6.7 and 6.8, the oscillations in $\left.\frac{\partial c}{\partial y}\right|_{y=0}$ do not lead to similar oscillations in c (with only minor distortions visible in Figure 6.8). Taking the case of the finite difference solution for the 3-layer system, which is validated against an analytical solution (Table 6.5), the relative error between the finite difference and the analytical solution is extremely small, much less than 0.01%. This is well inside what is considered to be an acceptable level of accuracy in numerical

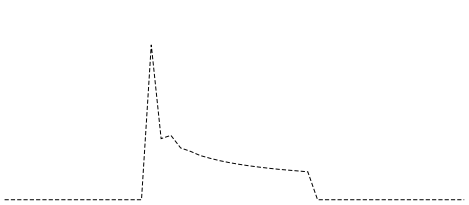

(a) 50×50 grid, 3-layer tablet.

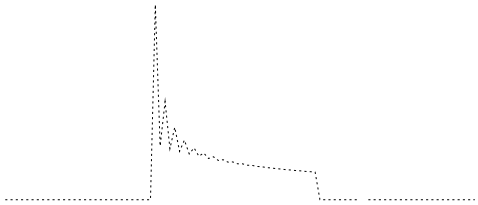

(b) 100×100 grid, 3-layer tablet.

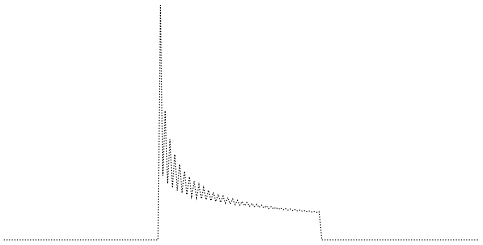

(c) 200×200 grid, 3-layer tablet.

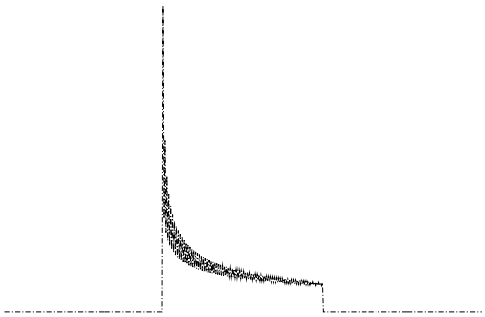

(d) 500×500 grid, 3-layer tablet.

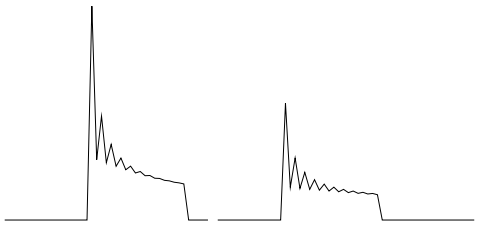

(e) 500×100 grid, 5-layer tablet.

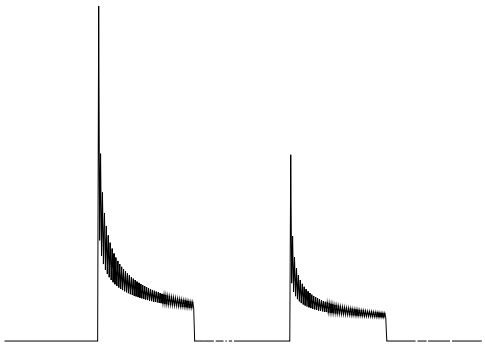

(f) 500×500 grid, 5-layer tablet.

Figure 6.6: Discontinuities in $\left.\frac{\partial c}{\partial y}\right|_{y=0}$, indicated by extreme values, occur at the edges of the diffusing regions, resulting in oscillations of the Crank-Nicolson results.

simulation [136]. This is despite the oscillations in $\left.\frac{\partial c}{\partial y}\right|_{y=0}$ evident in Figure 6.6 a-d. For this reason, although the extreme values of $\left.\frac{\partial c}{\partial y}\right|_{y=0}$ lead to oscillations in the

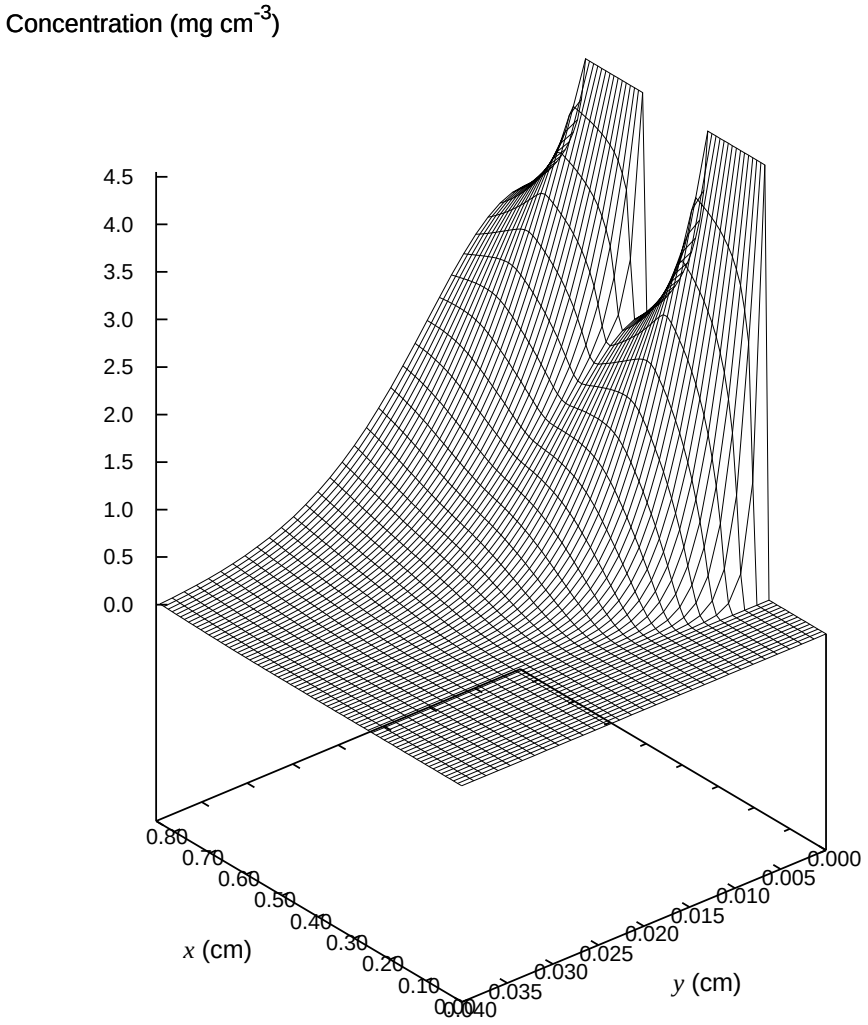

Figure 6.7: Reverse angle visualisation of the concentration gradients above the surface of a 5-layer tablet. The tablet surface is on the right of this plot and the fluid flow is from bottom right to top left. The high concentrations close to the two diffusing layers are clearly visible. Crank-Nicolson oscillations in $\left.\frac{\partial c}{\partial y}\right|_{y=0}$ do not lead to oscillations in c.

calculation of $\left.\frac{\partial c}{\partial y}\right|_{y=0}$ across the diffusing regions, the concentration values display smooth behaviour.

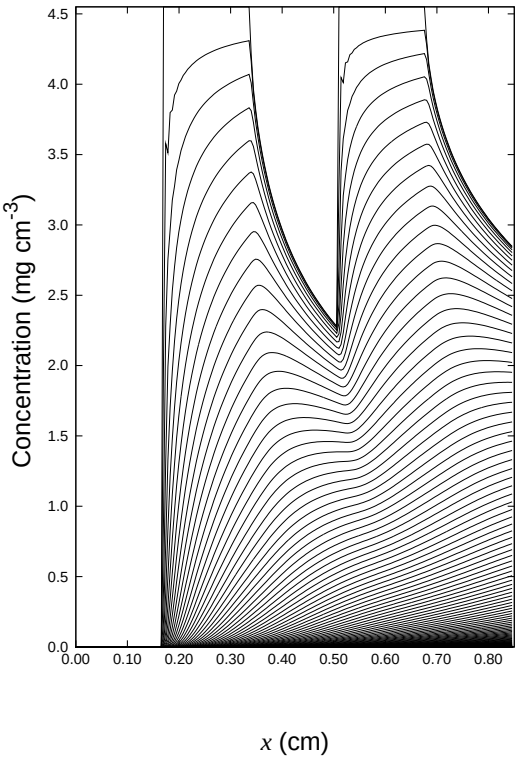

Figure 6.8: Concentration vs. x position. Contours are lines of constant y. This plot is generated from a 200×200 grid. Some minor oscillation is visible at high concentrations close to the leading edges of the diffusing regions ($x = x_1$ and $x = x_3$).

6.2.3 Validation, Comparison with Experiment and Previous Work

The good agreement between the finite difference method and the other models for 1-/3-layer compacts, suggests that the scheme is correctly describing the physics of dissolution (Table 6.5).

It is clear from Figure 6.1 and Tables 6.5 and 6.6 that results from the finite difference solution and the Pohlhausen solution of Crane et al. [17] diverge for systems of 5 layers and more. However, the solutions diverge more slowly as the number of layers increases. This behaviour is intuitive: the rate of increase in error between the two solutions ought to fall as the number of layers increases. The

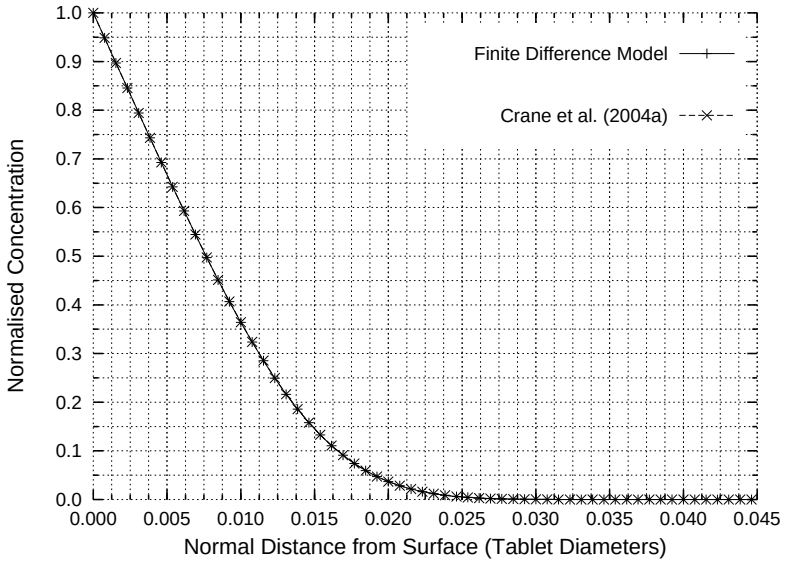

Figure 6.9: Concentration-distance curve normal to the compact surface at the start of the inert layer, $x = x_2$. The concentration curve for the Pohlhausen model was generated using an equivalent numerical implementation of the semi-analytical Pohlhausen model.

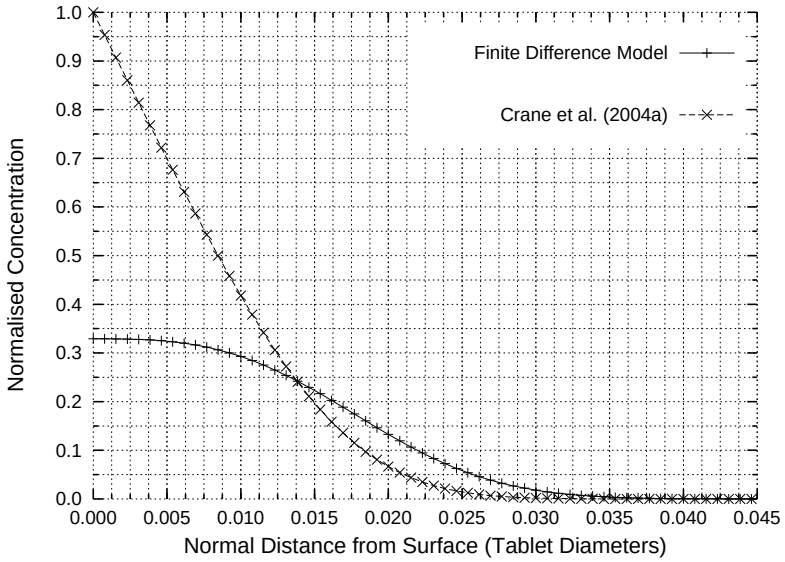

Figure 6.10: At the end of the inert region, at $x = x_3$. The finite difference curve is the more physically realistic.

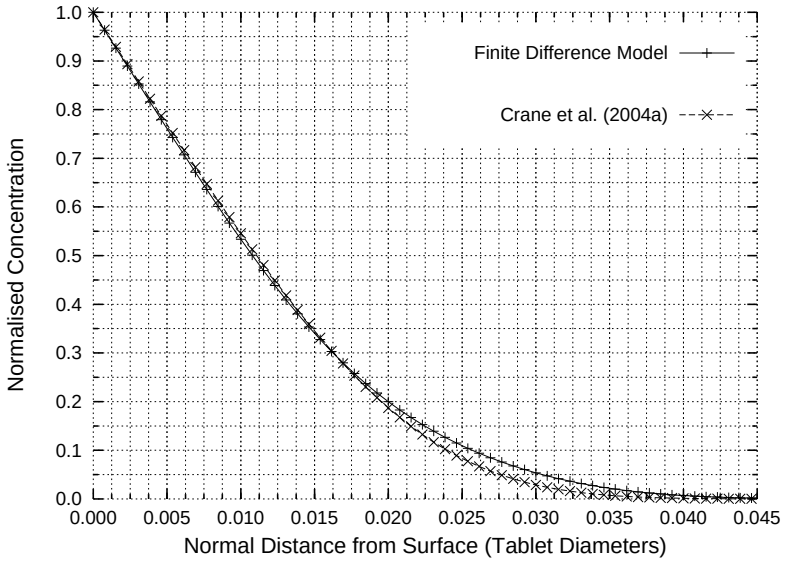

Figure 6.11: At the end of the second drug layer, $x = x_4$.

relative error between the solutions depends on the width of the layers, so as the layer widths reduce, the error between the two solutions per layer also reduces. As the number of layers grows very large, the overall error between the two solutions should increase more slowly, eventually converging on a fixed or systemic value.

The cause of the 10.1% difference between the Pohlhausen and finite difference solutions for a 5-layer system (Table 6.6) is illustrated in Figures 6.9 - 6.11. Referring to Figure 3.1, the drug concentration profiles and corresponding mass transfer rate estimates generated by the Pohlhausen and finite difference solutions almost coincide at the end of the first drug layer, at $x = x_2$ (Figure 6.9). Just before the start of the second drug layer, at $x = x_3 = 0.51$, the concentration-distance curves are quite different (Figure 6.10) but the mass transfer rates based on these curves are almost the same. Since the same linear velocity profiles are used in both solutions and we have confidence in the finite difference scheme, it is the difference in the shape of the concentration profiles at $x = x_3$ that gives rise to the slight difference in the drug concentration profiles at $x = x_4$ (Figure 6.11) and the differing mass transfer rates. The shape of the concentration profiles at x_3 only depends on how

the Neumann boundary condition within the central layer ($x_2 \leq x \leq x_3$) is implemented. It follows then that the 10.1% difference between the Pohlhausen and finite difference estimates can be entirely attributed to the differing implementations of this boundary condition. Further, the fixed relative error between the Pohlhausen and finite difference estimates (Figure 6.1) can also be entirely attributed to the different implementations of this same boundary condition.

Although the absolute theoretical and experimental mass transfer rate estimates differ (Table 6.5), if the 3-/5-layer results are presented as fractions of the associated 1-layer solutions, a much better agreement is evident (Table 6.6). This suggests that much of the underlying physics has been captured by the models. Recent hydrodynamic analyses [44; 19] show that for a compact placed centrally in the device the fluid flows tangential to the curved surface, not parallel to its long axis. One implication of this, corresponding with our results, is that the theoretical models will consistently underestimate the mass transfer rate. Any complete model of drug dissolution will need to incorporate, in addition to the velocity boundary-layer equations, a more realistic free-stream velocity, [e.g. 44; 19].

The results presented in this section were for layered tablets in which benzoic acid (BA) is treated as the drug component. Previous studies [104; 21; 17] provide graphed data for layered tablets in which salicylic acid is the drug component, i.e. the 1-layer compact consists entirely of BA and the 3- and 5-layer tablets have the form BA/SA/BA and the BA/SA/BA/SA/BA respectively. Graphing output from the finite difference model (Figure 6.12) and comparing it with graphs from Crane et al. [21] (Figure 6.13), we can see that the initial mass transfer rates calculated with the finite difference model agree reasonably well with the previous studies and with experiment.

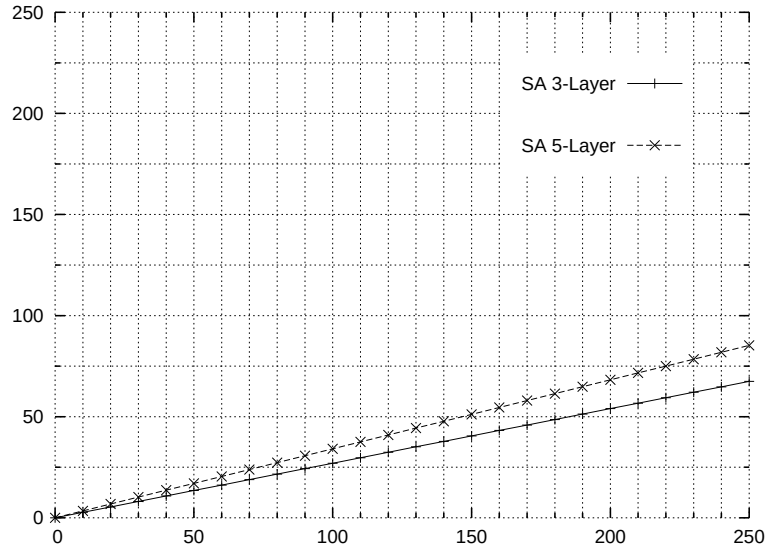

Figure 6.12: Finite difference showing dissolved mass of Salicylic Acid (SA) against time (minutes).

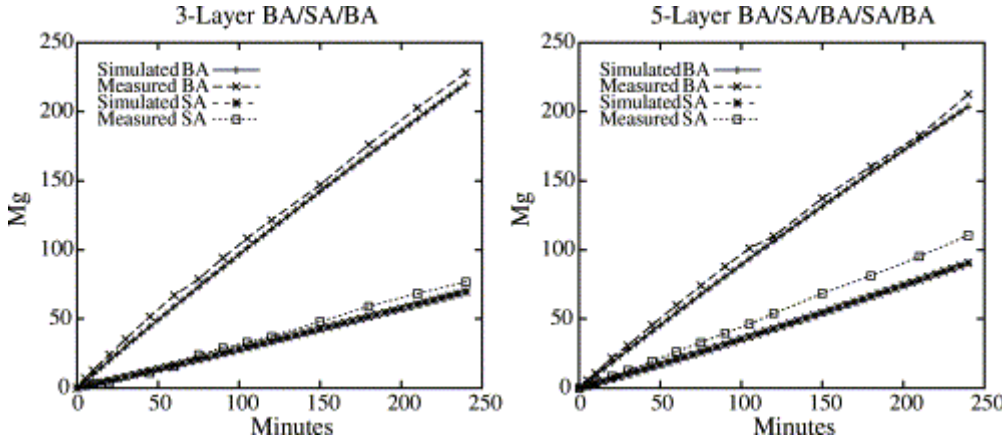

Figure 6.13: Results for compacts of BA and SA, showing dissolved mass of each substance against time. The 3-layer and 5-layer compacts have reversed structures when compared to the tablets for which results are presented in this thesis. Reprinted from [17], copyright (2004), with permission from Elsevier.

6.3 Chapter Summary and Conclusions

In summary, this chapter presented results from the first of three studies described in this thesis.

The Pohlhausen [17] and PSUDO [20] models of the initial mass transfer rate

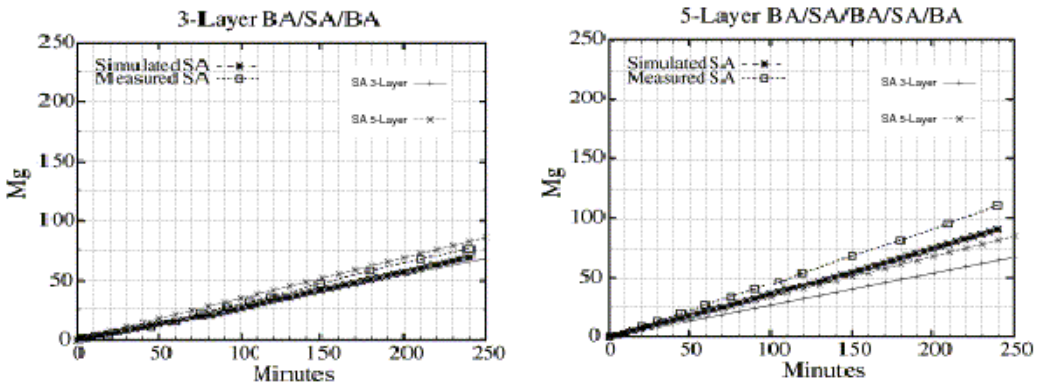

(a) (b)

Figure 6.14: Superimposing Figure 6.12 over Figure 6.13, it is evident that the current scheme agrees well with both experiment and previous simulation for the 3-layer case (a). For the 5-layer case (b), the current work, represented by the lowest solid line, underestimates the experimental measurements, the highest dashed line with empty boxes.

from a multi-layered tablet were examined and extended. Although some oscillation of a first derivative of the concentration c is present in the solution, the Crank-Nicolson (CN) finite-difference method was verified using the grid convergence index method and validated against data from an experimental study and analytical solutions and found to be a superior solution method. The CN solution and the previous Pohlhausen approximations to the drug mass transfer rate from the surface of a 5-layer compact are shown to differ by 10.1%, a fact attributed entirely to the different implementations of a derivative surface boundary condition. Using the CN model as a benchmark solution, the analytical Pohlhausen estimate is shown to be usefully accurate. The assumption of a steady, axial mainstream flow is likely to be the primary reason for the error between the experimental and theoretical results. A future complete model of drug dissolution must incorporate boundary-layer theory close to the surface using a more realistic free-stream velocity field ideally calculated concurrently using a computational fluid dynamics code.

In addition, several specific and general research questions are suggested to the interested reader. These include the explorations of the limits of validity for the

Pohlhausen solution, to further clarify the reasons for its deviation from the CN solution and to formally demonstrate that its convergence as the number of layers becomes very large can be written in a closed form. In addition, it will be interesting to formulate other applications for the extended Pohlhausen solution. These may have some utility when considering matrix tablets, where the drug is dispersed as very small particles throughout the tablet, i.e. a large number of layers may approximate matrix tablet behaviour. Other applications may include microelectrode analysis. The CN finite-difference method can be extended in many ways including the already mentioned consideration of more realistic flows from a coupled CFD code. There are many outstanding investigations around the CN scheme, including, e.g. detailed investigations of its validity and incorporation of more efficient mesh distributions.

Importantly, this study demonstrates that simulation, which includes mathematical and numerical approaches, is useful in the description of pharmaceutical processes. Chapter 7 continues with results from the second of the three studies that contribute to this thesis.

$\phi = \dot{m}$	**1-Layer Results**	**3-Layer Results**	**5-Layer Results**
	■ [BA]	▬ [-/BA/-]	〓 [-/BA/-/BA/-]
N_1, N_2, N_3	$40000, 10000, 2500$	$40000, 10000, 2500$	$40000, 10000, 2500$
h_1, h_2, h_3	$0.0002, 0.0005, 0.002$	$0.0002, 0.0005, 0.002$	$0.0002, 0.0005, 0.002$
r_{21}	2.25	2.25	2.25
r_{32}	4	4	4
ϕ_1	1.129213644	0.504887462	0.638030816
ϕ_2	1.129316609	0.504879397	0.637924898
ϕ_3	1.129940559	0.50451875	0.637449681
ϵ_{21}	0.000102965	-8.06485E-06	-0.000105918
ϵ_{32}	0.00062395	-0.000360647	-0.000475217
p	1.095741391	2.67159063	0.844602624
ϕ_{ext}^{21}	1.129141723	0.504888506	0.638138499
ϕ_{ext}^{32}	1.129141723	0.504888506	0.638138499
ϵ_{a}^{21}	0.01%	0.0016%	0.02%
$\epsilon_{\text{ext}}^{21}$	0.01%	0.0002%	0.02%
$\text{GCI}_{\text{fine}}^{21}$	0.01%	0.0003%	0.02%

Table 6.3: Calculating the grid convergence index for the Crank-Nicolson finite difference scheme presented in this thesis. The procedure is the same as outlined by Celik [149].

5-Layer [-/BA/-/BA/-]

$N^{\frac{1}{2}}$	$h \times 10^{-4}$	$\Delta x \times 10^{-4}$ (cm)	$\Delta y \times 10^{-4}$ (cm)	$\dot{m}$ (mg min^{-1})	t_{run} (s)
500	20.00	17.00	2.00	0.63745	18
1000	10.00	8.50	1.00	0.63775	75
1500	6.67	5.67	0.67	0.63786	167
2000	5.00	4.25	0.50	0.63792	297
2500	4.00	3.40	0.40	0.63796	479
3000	3.33	2.83	0.33	0.63799	666
3500	2.86	2.43	0.29	0.63801	973
4000	2.50	2.13	0.25	0.63802	1289
4500	2.22	1.89	0.22	0.63803	1637

Table 6.4: Linear convergence of the 5-layer solution with decreasing dimensionless cell size h (or increasing number of nodes, N). $\dot{m}$ (mg min^{-1}) is the mass transfer value and Δx and Δy are the dimensional finite difference cell dimensions. t_{run} is the program runtime. As h decreases, the solution converges to a value of $\dot{m}$ close to 0.63803 mg min^{-1}.

Data Source	1-Layer	3-Layer	5-Layer
	[BA]	[-/BA/-]	[-/BA/-/BA/-]
Experiment			
Healy et al. [104]	**1.46** (-)	**0.64** (-)	**0.73** (-)
(Semi-)Analytical Models			
Crane et al. [17]	1.17 (19.8)	-	-
Kestin and Persen [108]	1.13 (22.9)	0.51 (21.6)	-
Pohlhausen [21]	1.13 (23.0)	0.51 (21.6)	**0.58 (20.9)**
Finite Difference Model			
McMahon et al. [261]	1.13 (22.9)	0.51 (21.6)	**0.64 (12.9)**

Table 6.5: Experimental and theoretical values for the mass transfer rate of benzoic acid (BA) from 1/3/5-Layer compacts dissolving in a USP dissolution apparatus, $\dot{m}$ (mg min^{-1}). Percentage errors with respect to the experimental values are listed in brackets (%). The experimental values for 3/5 layer compacts are inferred from figures for salicylic acid in [21].

Data Source	**1-Layer**	**3-Layer**	**5-Layer**
	[BA]	[-/BA/-]	[-/BA/-/BA/-]
Experiment			
Healy et al. [104]	1.00 (29.8)	0.44 (27.5)	0.50 (26.4)
(Semi-)Analytical Models			
Crane et al. [17]	1.00 (4.1)	-	-
Kestin and Persen [108]	1.00 (0.1)	0.45 (0.1)	-
Pohlhausen [21]	**1.00** (-)	**0.45** (-)	**0.51** (-)
Finite Difference Model			
McMahon et al. [261]	1.00 (0.1)	0.45 (0.1)	**0.57 (10.1)**

Table 6.6: Experimental and theoretical values for the mass transfer rate of benzoic acid (BA) normalised with respect to 1-layer values. Percentage difference of mass transfer rates with respect to the Pohlhausen values are listed in brackets (%). The 10.1% discrepancy between the Pohlhausen and finite difference methods results from the different implementations of the Neumann boundary condition only. An important point is that although the finite difference results is a little further from the reported experimental value, the reasons why this is so are quite well understood.

Chapter 7

Results and Discussion, Study 2

In this chapter we present results from the second of two studies presented in this thesis, the flow around the top of a cylinder. The significance of these results, as well as their context in the overall thesis, is discussed.

7.1 2D Validation with Comparisons of Flow Around a Circular Cylinder

7.1.1 Qualitative 2D Validation

Visual comparisons of the flow patterns around a circular cylinder predicted by Fluent and experimental visualisations and descriptions in the literature formed part of our validation. The classification and description of the flow regimes discussed are taken from Coutanceau and Defaye's 1991 review paper [212]. This complete paper contains many striking images of two dimensional flow about circular cylinders and a flow regime classification with careful description.

The first flow regime considered consisted of flows of Reynolds number (Re) between 35 and 60 [212] . In this range, flow instabilities appear, with slight asymmetry of the attached wake bubble and less well defined boundaries between the wake bubble and the surrounding, increasingly wavy, wake flow. For a laminar

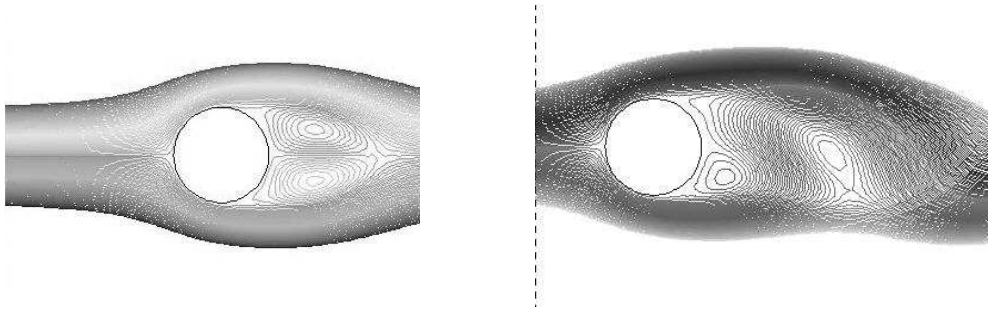

(a) (b)

Figure 7.1: (a) Flow pattern around an infinite, or 2D, cylinder with $Re = 50$. (b) Flow around the same cylinder but with $Re = 80$. These images were generated using the commercial CFD code Fluent as a demonstration and validation of its capabilities. The flow patterns agree well with experimental observations [212].

incident flow at a Reynolds number of 50, the flow pattern generated by Fluent compares favourably with experimental description (Figure 7.1 (a)).

The second flow regime considered consists of flows where $60 < Re < 100$. In this range the wake asymmetries are pronounced, leading to vortex shedding from alternate sides of the cylinder [212][1]. The output from Fluent for a laminar incident flow again agrees well with experiment (Figure 7.1 (b)). The attached bubble can be seen on the bottom right of the cylinder with a shed vortex downstream.

The final flow regime considered as part of this visual comparison with experiment is defined by flows where $2 \times 10^3 < Re < 100 \times 10^3$. Flows in this regime still display a laminar boundary-layer which separates from the surface at about 80° from the stagnation point at the front of the cylinder; this separation point moves forward as the Reynolds number increases [212]. An irregular secondary boundary-layer is formed and a turbulent von Kármán vortex street is fully established. As illustrated in Figure 7.2, the Fluent solution for a flow of $Re = 3900$ agrees well with this description and with experimental visualisations [e.g. 263; 212].

[1]The asymmetric vortices are caused by small oscillations in the pressure distribution around the cylinder.

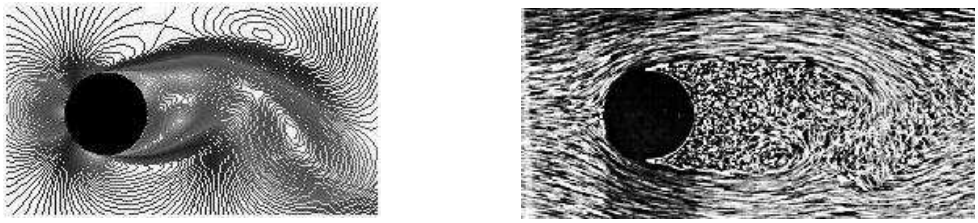

(a) (b)

Figure 7.2: (a) Fluent generated 2D flow around an infinite cylinder with $Re = 3,900$. (b) An experimental visualisation of 2D flow at a $Re = 2,000$, taken from [263]. These systems fall within flow Regime 7, $2,000 < Re < 100,000$ [212]. The Fluent solution agrees well with this observed flow.

7.1.2 Quantitative 2D Validation

Our quantitative validations focused on measurable quantities such as the drag coefficient, C_d, the circumferential pressure coefficient C_p and the angle of separation, θ. For laminar flow regimes, up to $Re \approx 10^3$ [212], the Fluent estimates for C_d compare well with classic experimental studies [e.g 210; 213] (Figure 7.3 and Table 7.1). The Fluent generated output agrees well with experimental results for C_d, C_p and θ from several large eddy simulation models as well as the experimental measurements for $Re = 3,900$ presented by Franke et al. [206] (see Table 7.2).

It is evident however, that *reasonably well* is the strongest statement that can possibly be made about how well the Fluent data matches results from other studies. There is ample room for disagreement about this positive assessment. The results for the flow variables are extremely sensitive to boundary conditions, small changes in the cylinder geometry, and small disturbances in the calculated flow caused by numerical error, e.g. truncation and rounding errors [206]. Variables evaluated close to the surface of the cylinder can be particularly sensitive to grid resolution. Experimental studies are extremely sensitive to test rig variables, including the aspect ratio of the test channel, blockage effects, end conditions and the turbulence intensity of the flow. It is important to bear all this in mind when comparing results for apparently similar systems. It is reasonable, given that the Fluent simulation produces qualitatively correct results especially away from the surface, to state that

Re	$\text{Log}_{10}(\text{Re})$	$\boldsymbol{C_d}$ Fluent	$\text{Log}_{10}(C_d \text{ Fluent})$	$\boldsymbol{C_d}$ Exp	$\text{Log}_{10}(C_d \text{ Exp})$	**% Error**
1	(0.00)	10.00	(1.00)	10.40	(1.02)	3.85
2	(0.30)	6.00	(0.78)	6.30	(0.80)	4.76
4	(0.60)	5.00	(0.70)	4.10	(0.61)	21.95
8	(0.90)	3.00	(0.48)	2.90	(0.46)	3.45
10	(1.00)	2.40	(0.38)	2.60	(0.41)	7.69
20	(1.30)	2.10	(0.32)	1.90	(0.28)	10.53
30	(1.48)	1.80	(0.26)	1.70	(0.23)	5.88
40	(1.60)	1.60	(0.20)	1.50	(0.18)	6.67
50	(1.70)	1.50	(0.18)	1.40	(0.15)	7.14
80	(1.90)	1.40	(0.15)	1.40	(0.15)	0.00
100	(2.00)	1.40	(0.15)	1.40	(0.15)	0.00
150	(2.18)	1.30	(0.11)	1.20	(0.08)	8.33

Table 7.1: Comparison of calculated and experimental values for the drag coefficient C_d of a 2D flow around a cylinder at low Reynolds numbers. Experimental values are taken from [210] and [213].

the results produced with Fluent do match results from the literature *reasonably well*.

7.2 3D Validation with Comparisons of Flow Around a Circular Cylinder

The validation for three-dimensional flow about a finite cylinder proceeded in a similar way to the two-dimensional validation. The primary references for validation of the three-dimensional simulation of the flow over the top of the cylinder were papers by Park and Lee [204] and Kline [205]; Park and Lee provide a description of the flow for a qualitative comparison, while Kline provides experimental speed-up

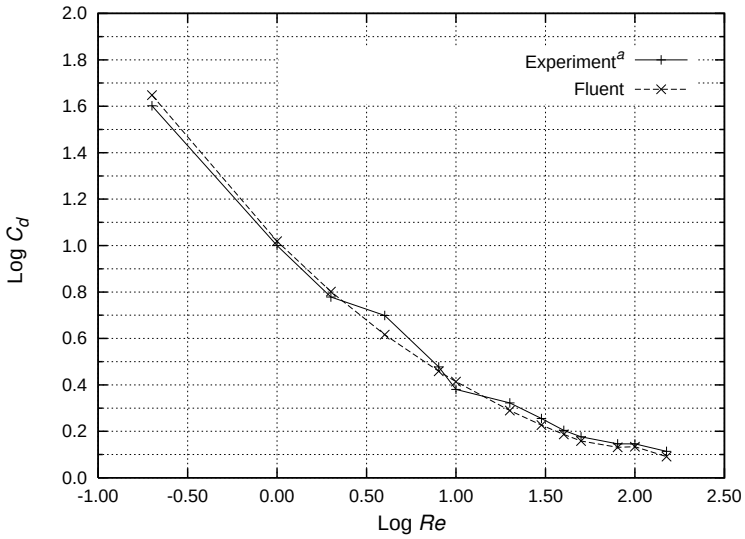

Figure 7.3: Comparison of calculated and experimental values for the drag coefficient C_d of a 2D flow around a cylinder at low Reynolds numbers, ranging from 0.2 to 150. *Note*: *(a)* these values are taken from [210] and [213].

measurements.

7.2.1 Qualitative 3D Validation

As illustrated in Figure 7.4, the visualised Fluent solution for a 3D flow of Reynolds number 20,000 past a finite cylinder of height to diameter ratio 5 ($H/D = 5$) agrees well with the experimental flow observed and recorded by Park and Lee [204]. This is particularly true in the region of interest directly above the top of the cylinder.

7.2.2 Quantitative 3D Validation

Uematsu and Yamada [266; 218] present experimental data for flows around finite cylinders with $Re \geq 38 \times 10^3$. Values for the drag coefficient (C_d) of the 3D finite cylinder correspond with experimental values [218] ($C_d \approx 0.60$, which falls within the range of experimental measurements for a $H/D = 3$). The authors also present results for the measured circumferential pressure coefficient (C_p) distribution around the middle ($H/2$) of a finite cylinder with $H/D = 3$. These distributions are mea-

Data Source	C_d	C_{pb}	θ_s
Franke and Frank **[206], LES**^{a}:			
(i)	1.005	0.94	89.0
(ii)	0.999	0.90	88.7
(iii)	0.994	0.88	88.5
(iv)	0.985	0.86	88.3
(v)	0.978	0.85	88.2
Experiment^{b,c}	0.980^{d}	0.90^{e}	85.0^{f}
Fluent	1.160^{g}	1.00^{h}	90.0^{i}

Table 7.2: Comparison of numerical solutions and experimental results for two-dimensional flow about an infinite cylinder at $Re = 3,900$. *Notes*: *(a)* results from the LES models of Franke and Frank [206]; *(b)* and *(c)* are experimental results [264] [265] (*in* [206]); *(d), (e), (f)* have quoted measurement errors of ± 0.05, ± 0.05 and ± 2 units respectively [206]; *(g),(h)* and *(i)* are averaged values of oscillating quantities. Oscillation is due to asymmetric vortex shedding from the cylinder.

sured for both low and high turbulence intensities. *Low turbulence* corresponds to an intensity of 0.1% while *high turbulence* corresponds to an intensity of 6.4%.

Low turbulence calculations using Fluent for a 2D cylinder result in a C_p distribution that agrees well with the experimental distribution of C_p around a finite cylinder measured at $H/2$ [218] (Figure 7.5). This is not surprising since the flow around a finite cylinder at $H/2$ is almost two-dimensional. Low turbulence 3D Fluent calculations for C_p at $H/2$ around a finite cylinder agree less well with experiment [218] although the case for a high turbulence intensity shows closer agreement. The magnitudes and C_p distribution are both approximately correct.

From experimental studies [218], it can be seen that the C_p distribution varies between flows of different turbulence intensity. In low turbulence flows, the magnitude of C_p remains almost constant in the range $70° < \theta < 180°$, where θ is

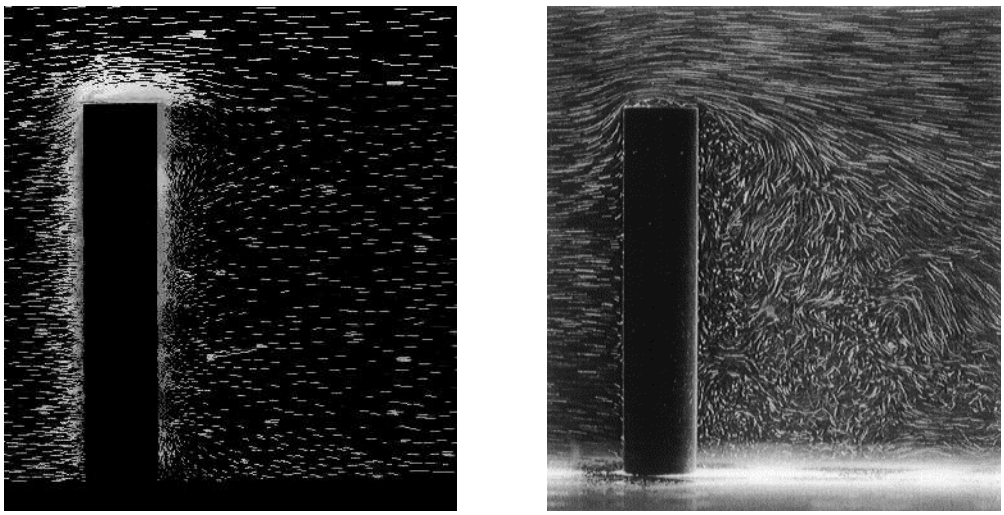

(a) (b)

Figure 7.4: (a) Fluent generated 3D flow around a finite cylinder of $H/D = 5$ at $Re = 20,000$. (b) An experimental visualisation of 3D flow past a similar cylinder at $Re = 20,000$. Reprinted from [204], Copyright (2000), with permission from Elsevier.

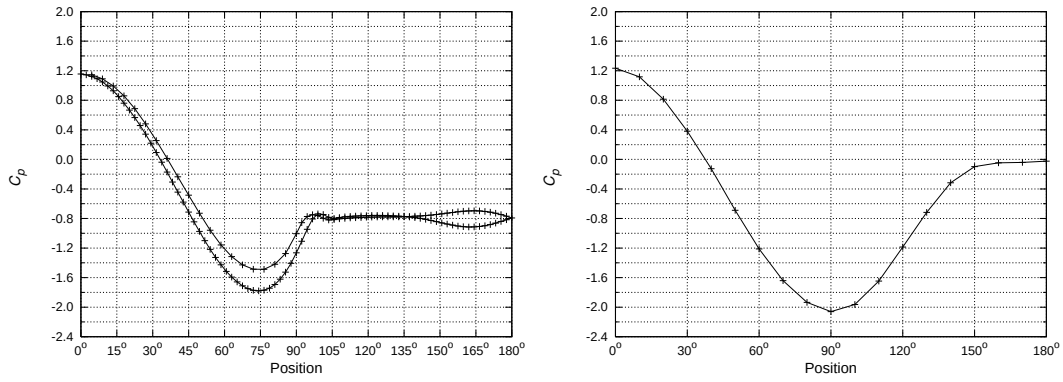

(i) (ii)

Figure 7.5: (i) C_p at $Re = 38 \times 10^3$ for 2D flow around a cylinder, (ii) C_p distribution at $H/2$ for low flow turbulence around a finite cylinder.

measured from the forward stagnation point. In the high turbulence case, however, C_p does not begin to level off until at least $\theta \approx 110^\circ$.

Since C_p on the windward side of the cylinder agrees quite well with literature and as we were interested, for this problem, in the flow several diameters vertically above the cylinder, the flow on the lee-side of the cylinder will not have an effect in this region. In the region of interest, one diameter above the cylinder, close wall

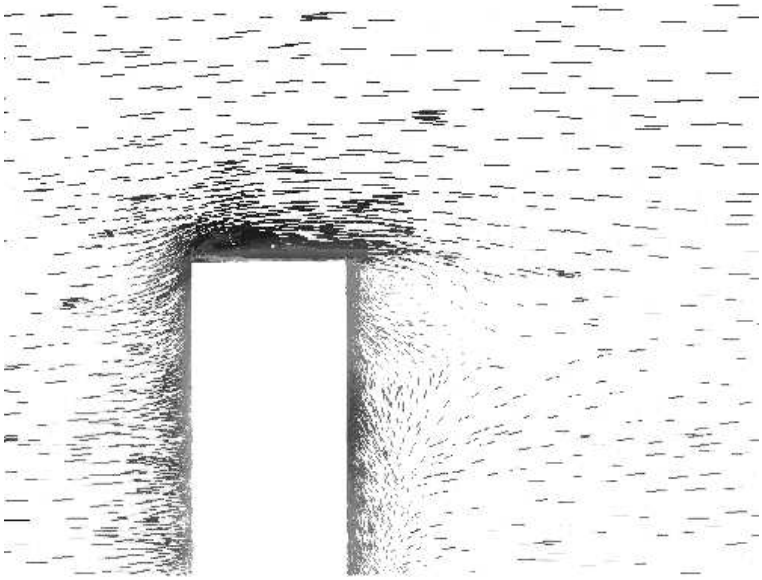

Figure 7.6: Detail from Figure 7.4 (a), a Fluent simulation of flow past a finite cylinder of height to diameter ratio 5 at a Reynolds number of 20,000.

and wake effects have little or no impact.

The quality of the simulation results is highly dependent on the mesh used. In the two-dimensional case, we found that meshes with circular or semi-circular computational domains gave the most realistic results when compared with literature. Similarly, in the three-dimensional case we used hemi-spherical and quarter-spherical domains; this was partly due to the relative success of the circular and semi-circular meshes in the two-dimensional case. There are, of course, limitations associated with these models including the fact that we are currently uncertain about the three-dimensional models' ability to capture close wall and wake effects.

7.3 Effect of a Meteorological Tower on its Top-Mounted Anemometer

For all configurations of wind-speed, turbulence intensity and terrain slope, our simulations show a significant difference between speed-up errors for solid and hollow

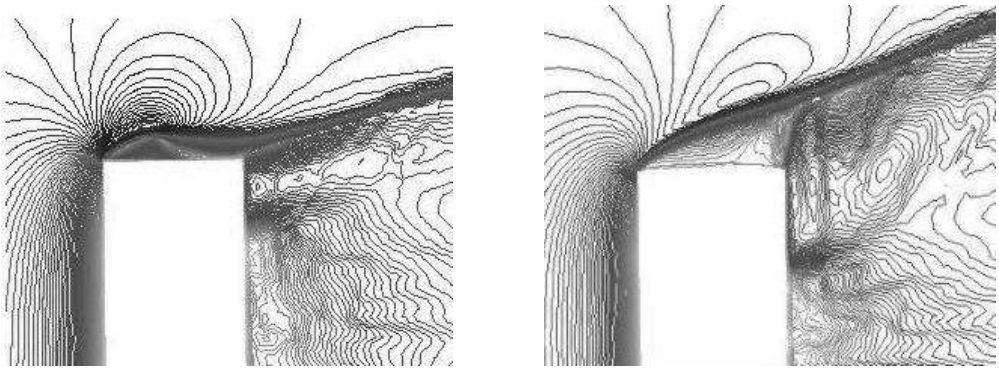

(a) (b)

Figure 7.7: Fluent generated 3D flow around (a) a solid cylinder (unstable) and (b) a hollow cylinder (stable). The internal flow up through the centre of the hollow cylinder tends to stabilise the main flow, forming the triangular pattern over the cylinder evident in (b). The recirculating flow about the top of the solid tower, however, is unstable and varies considerably with time.

towers. The airflow around the top of solid towers appears to be less stable, with rapid, time-dependent, fluctuations which give rise to significant uncertainty in the determination of the speed-up error. For a solid tower, the predicted speedup at a height of 2 diameters above the top of the tower is in the range of 1.5% to 2.0% (Figure 7.9). Results for the problem of a hollow tower with an anemometer located 2 diameters above the top are presented below.

7.3.1 Sensitivity to the Free-stream

Most wind turbines operate at wind-speeds ranging from 8 to 12 m/s. In this range, the relative magnitude of the simulated speed-up is almost independent of the absolute magnitude of the free-stream wind-speed (speed-up is written as a percentage of the free-stream wind-speed). This independence can be seen in Figure 7.10 - 7.12 for a free-stream turbulence intensity of 10%.

7.3.2 Sensitivity to Turbulence

In the normal operating range of wind-speeds (8 to 12 m/s) and turbulence intensities, the simulated speed-up appears to be also independent of the turbulence inten-

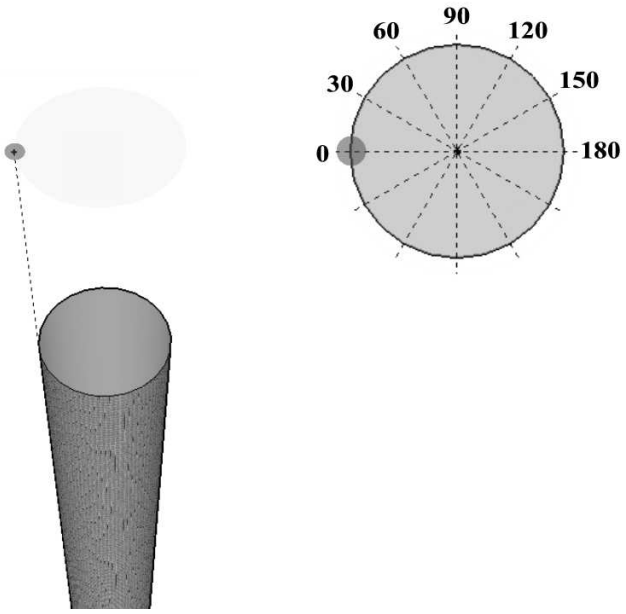

Figure 7.8: Sample anemometer positions (in steps of 30°) around the circumference of the meteorological tower. The wind blows from left to right. The anemometer cups are located two diameters above the top of the tower.

sity of the free-stream (Figure 7.13). This conclusion is based on two simulation runs with turbulence intensities of 10% and 15% and implies that the anemometer data can be corrected without any complications arising from turbulence in the airflow. Together with the previous observation (Section 7.3.1), we find that the speed-up can be associated with a particular anemometer set-up and is dependent only on quantities that can be determined (terrain slope, tower geometry, fluid properties and tower surface conditions).

7.3.3 Sensitivity to Sloped Terrain

Airflow is accelerated when passing over a hill and, for this reason, wind farms are often sited on slopes. For practical considerations, these slopes never exceed 25°. Simulation runs at slopes of 0°, 15° and 25° indicated that, as expected, the speed-up has a significant dependence on terrain slope (Figure 7.14 and 7.15). However,

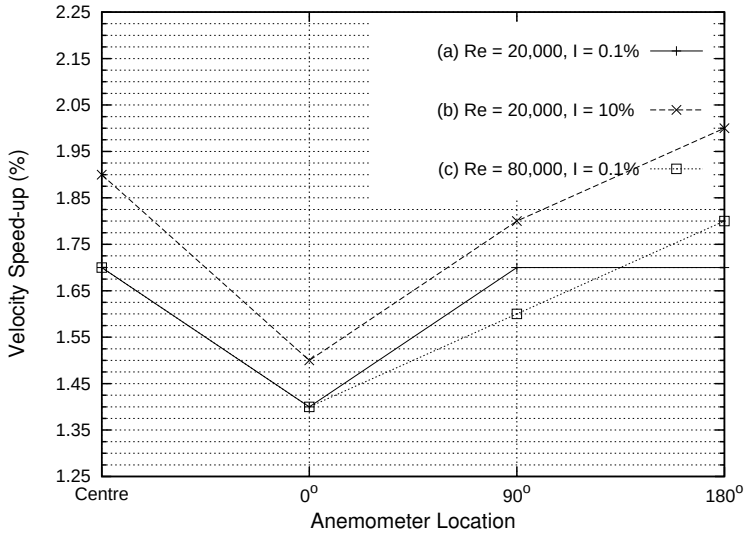

Figure 7.9: Influence of the free-stream wind-speed (i.e. Re) and turbulence intensity (I) for a solid tower positioned on level ground. *Notes*: (a) $Re = 20 \times 10^3$, $I = 0.1\%$; (b) $Re = 20 \times 10^3$, $I = 10.0\%$; (c) $Re = 80 \times 10^3$, $I = 0.1\%$.

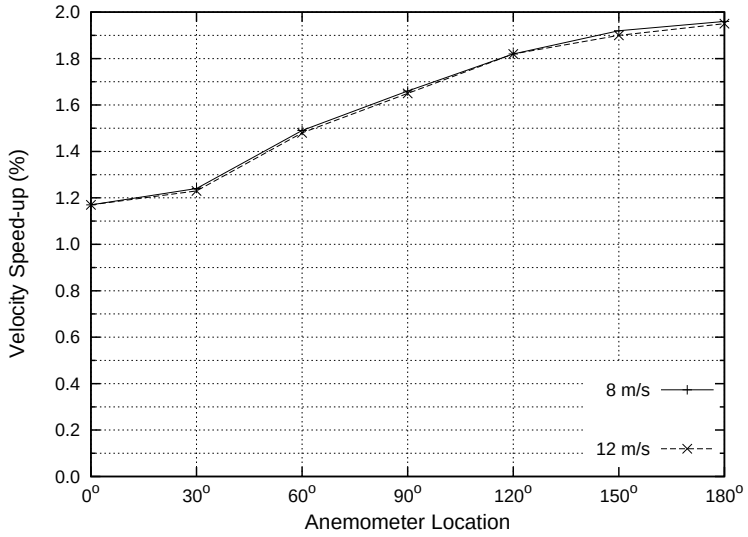

Figure 7.10: Influence of the free-stream wind-speed for a hollow tower positioned on level ground and a turbulence intensity of 10%.

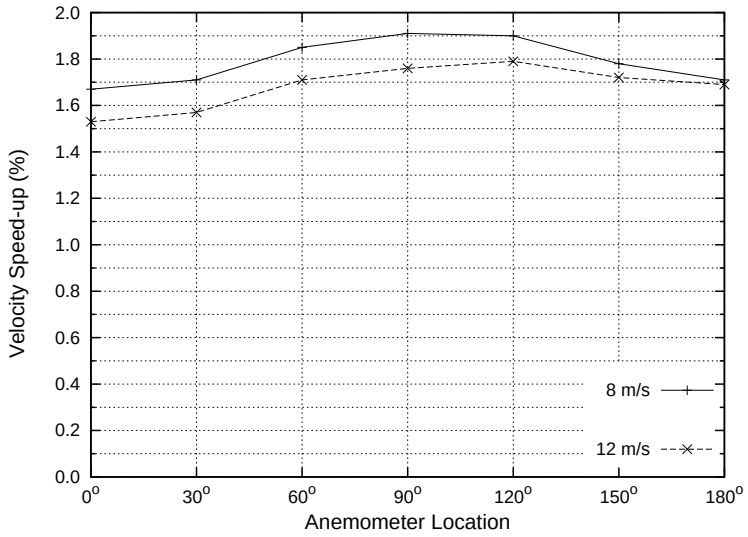

Figure 7.11: Influence of the free-stream wind-speed for a hollow tower positioned on a slope of 15° and a turbulence intensity of 10%.

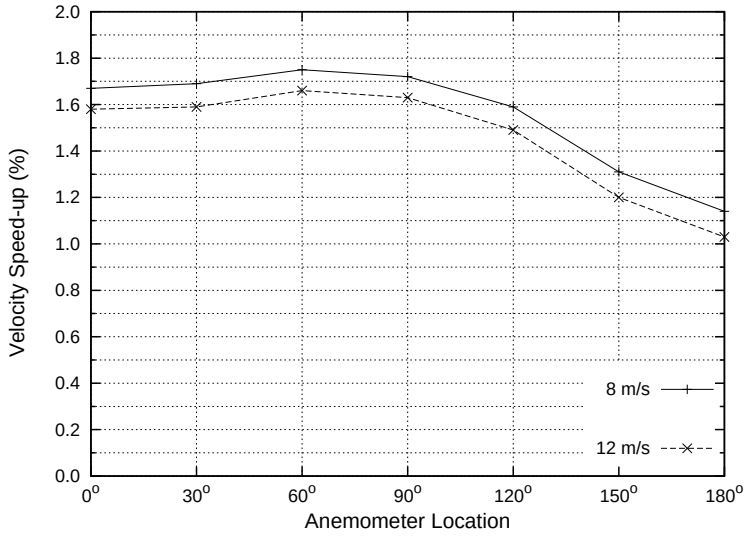

Figure 7.12: Influence of the free-stream wind-speed for a hollow tower positioned on a slope of 25° and a turbulence intensity of 10%.

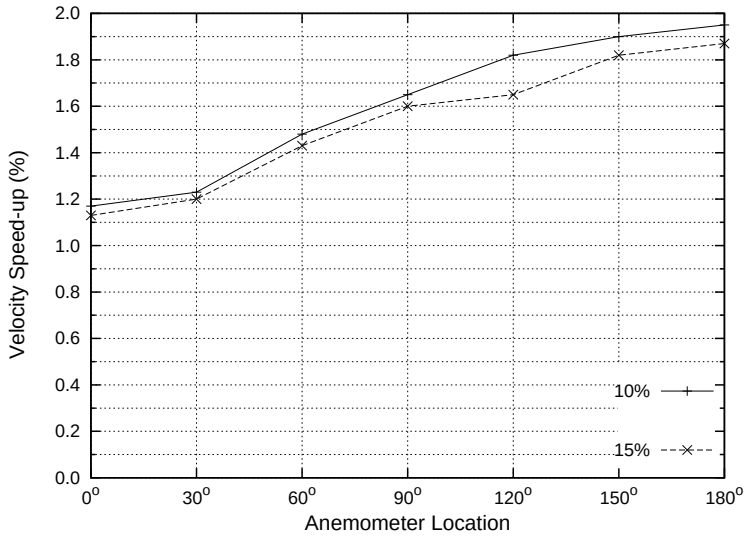

Figure 7.13: Influence of the turbulence intensity for a hollow tower positioned on level ground and a free-stream wind-speed of 8 m/s.

as can be seen in these figures, there is only a small difference between speed-up values from 0° through 60° (Figure 7.8) for slopes of 15° and 25°. This leads to the practical suggestion that if the prevailing wind is up-hill and parallel to the hillside, speed-up dependence on slope can be minimised by installing the anemometer on the upstream side of the tower, between 0° and 30° on the circumference (Figure 7.8).

7.3.4 Sensitivity to Tower Condition

The surface roughness of the interior of the hollow tower is captured by the pipe friction coefficient λ. We ran simulations with $\lambda = 0.02$ and $\lambda = 0.05$, corresponding respectively to a very smooth and a very rusty tower. For the case of a tower positioned on level ground, with a free-stream wind-speed of 8 m/s and a turbulence intensity of 10%, there is a small dependence on λ (Figure 7.16). A more complete study may establish that for normal wind conditions, the pipe friction coefficient does not significantly affect the speed-up error. Careful selection of tower materials, regular maintenance and cleaning will minimise variability in the condition of the

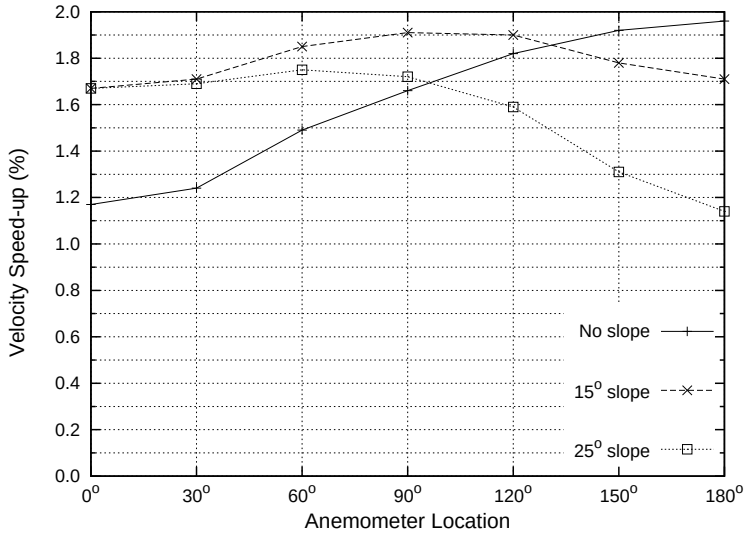

Figure 7.14: Influence of terrain slope for a hollow tower in a free-stream wind-speed of 8 m/s and a turbulence intensity of 10%.

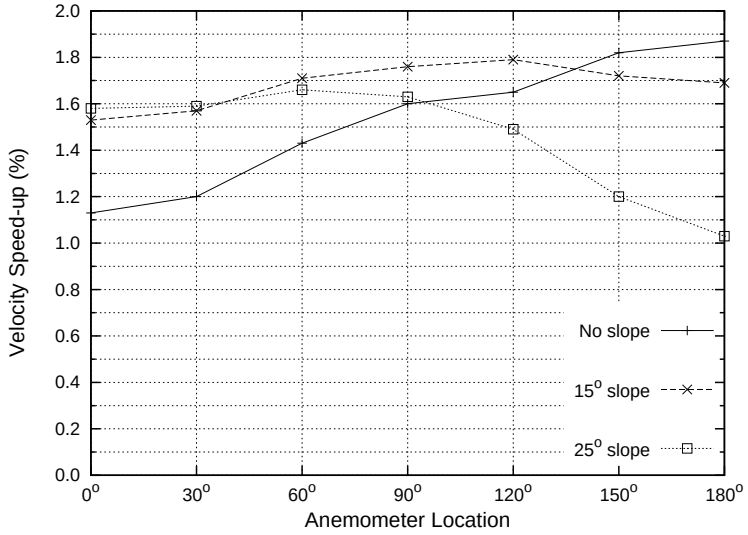

Figure 7.15: Influence of terrain slope for a hollow tower in a free-stream wind-speed of 12 m/s and a turbulence intensity of 10%.

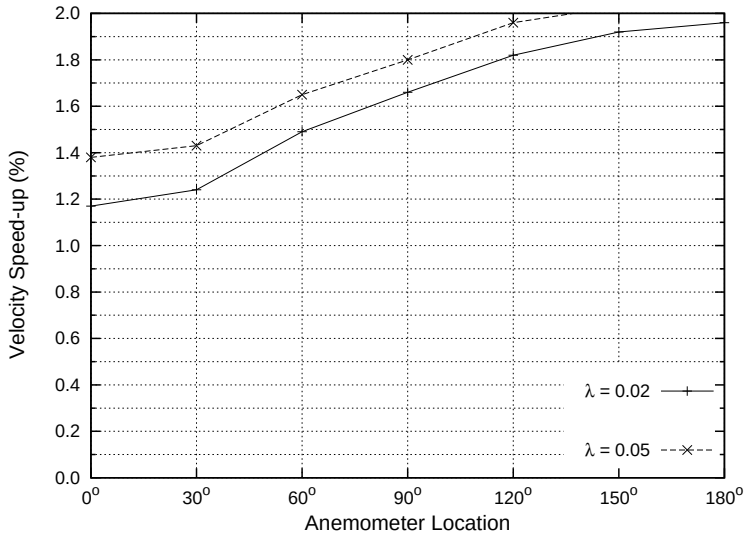

Figure 7.16: Influence of the pipe friction coefficient λ for a hollow tower positioned on level ground, a free-stream wind-speed of 8 m/s and a turbulence intensity of 10%.

tower and of any effect that the surface roughness (and debris) will have on the airflow through and around the structure.

7.3.5 Speed-up Envelope

In addition to the speed-up values for anemometers located 2 diameters above the top of the tower, we also recorded wind-speed values at various heights above the centre of the tower. The speed-up decreases as the distance above the tower increases. This is shown in Figure 7.17 for a wind-speed of 12 m/s and a turbulence intensity of 10%. Engineers and technicians may find this plot useful when locating anemometers.

7.4 Chapter Summary and Conclusions

In summary, this chapter presented results from the second of three studies described in this thesis.

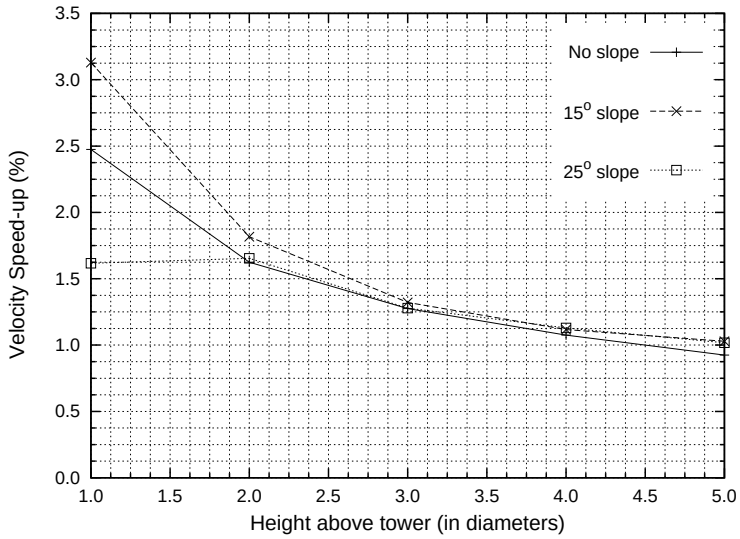

Figure 7.17: Speed-up values at various heights above the centre of a hollow tower positioned on level ground.

This second study began with an investigation of the flow around a finite cylinder with attention given to the problem of determining the measurement error due to speed-up for the specific case of an anemometer located 2 diameters above the top of a hollow meteorological tower sited on level terrain. It was found that the maximum error for this configuration is approximately 2% of the actual wind-speed (Figure 7.10). This compares well with experimental measurements for a hollow meteorological tower, which range from 1.7% to 3.4% [205].

It is concluded that the speed-up over the top of a hollow meteorological tower depends only on variables that can be determined. Speed-up is independent of the absolute magnitude of the free-stream wind-speed and the turbulence intensity of the wind. The error depends on the geometry of the meteorological tower, the slope of the terrain where the tower is sited and the condition of the tower.

In summary, top-mounted anemometers should be located at the windward side of a meteorological tower, where a particular wind direction prevails, and at least 5 diameters above the top. This will reduce speed-up to less that 1%. The IEA recommendation is for a minimum separation of about 6 tower diameters [203].

In line with the IEA's recommendation that the anemometer installation should be 'clean' [203], towers should be made from a corrosion resistant material and maintained and cleaned regularly to minimise flow disturbance.

Many other research problems are indicated; in the area of wind energy, several new refinements of the work developed here are essential and will make a useful contribution to the field. These include extending the analysis for different tower and anemometer configurations and for different tower types, e.g. considering the error in wind-speed measurements from anemometers mounted close to the *side* of a meteorological tower. Another useful study will be to further refine the simple turbulence model used and to carry out a more complete study of the effect of turbulence.

Although not pursued explicitly, techniques developed here for the problem of flow around a meteorological tower can be applied to the similar problem of flow around a finite cylindrical tablet. Using the specific problem outlined here as a basis, it is argued that simulation can provide useful insight for similar pharmaceutical problems. Chapter 8 continues with results from the third of the three studies that contribute to this thesis.

Chapter 8

Results and Discussion, Study 3

In this chapter we present results from the final of the three primary investigations presented in this thesis, mass transfer from a particle moving through the USP apparatus. The significance of these results, as well as their context in the overall thesis, is discussed. Unless specified otherwise, the equations of motion used to produce the results presented in this chapter were Equations (5.4 - 5.9).

8.1 Computer Implementation of Taylor's Work

Results for two different initial conditions were calculated, (1) with the particle assumed to be at rest with respect to the reference frame at $t = 0$ and (2) with the particle assumed to move with the flow at $t = 0$. In addition, solutions were calculated when (i) Stokes' law of resistance applies, using Equations (5.11) and (5.12) and (ii) Stokes' law does not apply, using Equations (5.13) and (5.14). A sample of these results is presented in Table 8.1.

Figure 8.1 (a) is a plot of the particle path for $\alpha = K_0 c = 0.5$, all defined previously, with Stokes' law of resistance assumed to apply and with the particle initially at rest[1]. Figure 8.1 (b) shows the particle path for the same α when Stokes' law does not apply, the particle is moving with the flow at $t = 0$ and the initial

[1] As discussed in Chapter 5, α is a parameter which is a function of $a^2 c$.

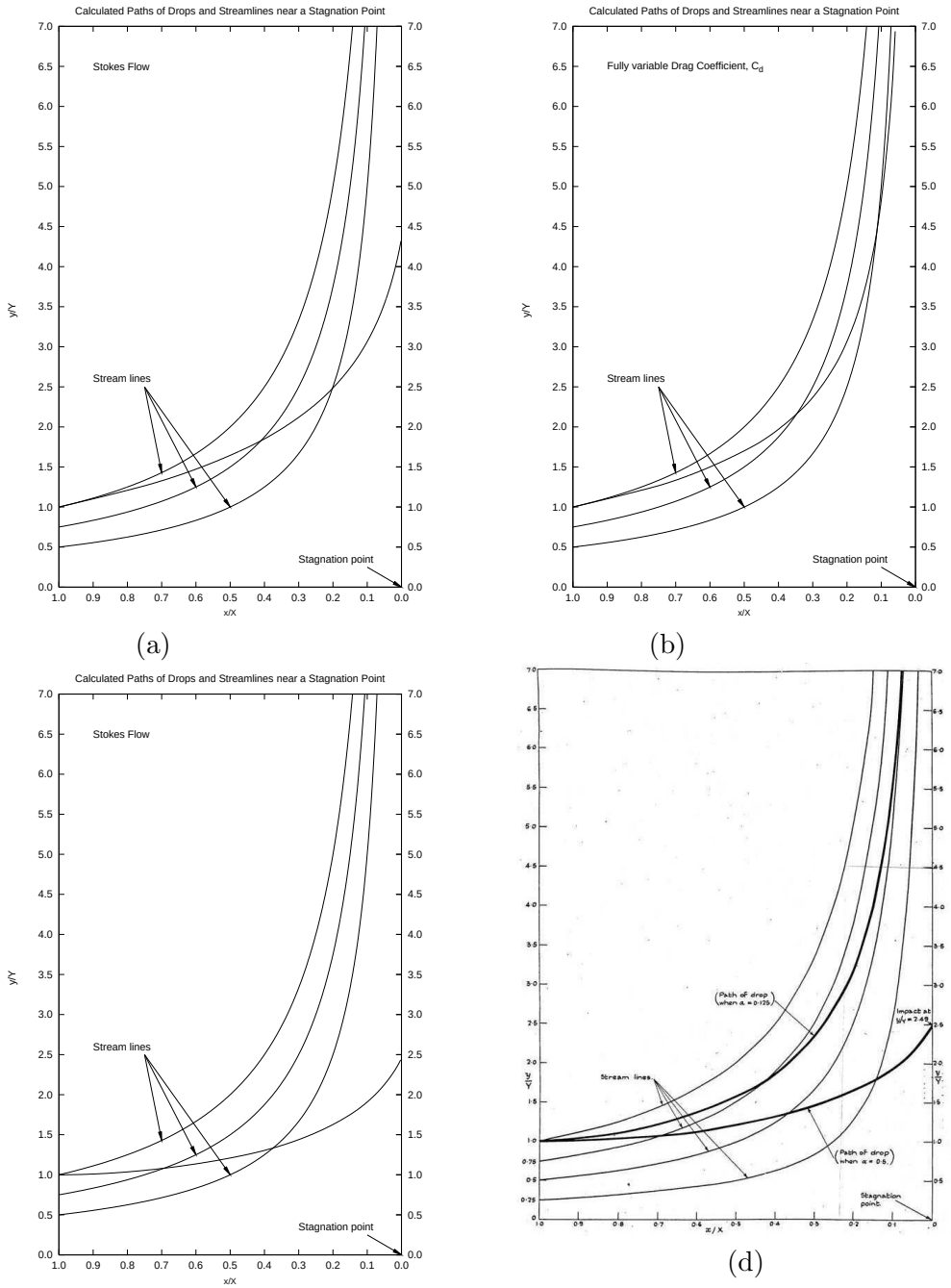

Figure 8.1: (a): $\alpha = 0.5$, Stokes flow, particle initially at rest. (b) $\alpha = 0.5$, Stokes' law does not apply, particle initially moving with the flow. (c): $\alpha = 0.5$, Stokes' flow, particle initially moving with flow. (d) Reproduced from Taylor's paper [22]: $\alpha = 0.5$, Stokes' flow, particle initially moving with flow.

	α	$Re_{t=0}$	y' **(impact)**	z **(impact)**	**time-step (impact)**
(a) - (1)(i)	0.5	-	4.36	4.72	471
(b) - (2)(ii)	0.5	100	-	-	481
(c) - (1)(ii)	0.5	-	2.45	3.15	314
(d) - Taylor	0.5	-	2.49	-	-

Table 8.1: Results for initial conditions (1) and (2) and flow types (i) and (ii). y' is the dimensionless displacement along the surface away from the stagnation point and z is the dimensionless time.

Reynolds number $Re_{p,t=0}$ is moderate, i.e. 100. Figure 8.1 (c), again corresponding to $\alpha = 0.5$, shows the path traced for assumed Stokes flow when the particle initially moves with the flow. Figure 8.1 (d) is reproduced from Taylor's paper [22], again with $\alpha = 0.5$, assumed Stokes flow and with a particle which initially moves with the flow.

The Runge-Kutta integration procedure consumes almost all the computation time. At present the current implementation[2] calculates about 3,700 time-steps per second. By way of comparison, the same Runge-Kutta integrations carried with pen, paper and an electronic calculator proceed at a rate of about 1.2 time-steps per hour and longer using a slide-rule instead of calculator[3]. Glauert's calculations [22; 23] seem all the more remarkable for this. Implementing this work numerically was important for the successful implementation of a particle tracking routine for the three-dimensional USP apparatus flow-field.

8.2 Extending Taylor's Analysis

One additional analysis is to consider the relationship between particle size and the average relative velocity magnitude, $|\bar{q}|$, i.e. the magnitude of the velocity of the

[2]Python script running on a Windows Intel Pentium 4, 2.4 GHz machine with 512 MB RAM.
[3]Conducted by the unpractised author.

particle with respect to the fluid, averaged over a fixed simulation time, t_s. It is speculated that $|\bar{q}|$ will increase with particle size, defined by particle radius a, and approach a limit as the particle size becomes large. Taking the case when Stokes' law applies, i.e. for very low average relative Reynolds numbers $\bar{Re}_p$ between the particle and the fluid, Taylor's problem of a particle moving close to a stagnation point can be solved using primitive variables with Equations (5.4 and 5.5).

Solving these equations using the Euler/LPA algorithm, the particle position and velocity components u and v as well as the resultant velocity q at each timestep in the interval $t = 0$ to $t = t_s$ were determined. The relative velocity magnitude $|q|$ was then calculated at each timestep and averaged over the simulated time t_s. Results for particles of various sizes moving through a stagnation flow, i.e. $u = -cx$ and $v = cy$, with velocities defined by $c = 0.5$ are presented in Table 8.2. The calculations were run for a simulated time of t_s for all the particle sizes. The resulting average relative velocity $|\bar{q}|$ averaged over t_s for each a is graphed in Figure 8.2.

a **(mm)**	c	Δt **(s)**	$\lvert\bar{q_p}\rvert$ **cm s^{-1}**	$\lvert\bar{q_f}\rvert$ **cm s^{-1}**	$\lvert\bar{q}\rvert$	$\bar{Re}_p$
0.100	0.500	0.004	0.817	0.863	0.046	0.291
0.200	0.500	0.004	0.641	0.756	0.115	1.452
0.300	0.500	0.004	0.536	0.685	0.148	2.800
0.400	0.500	0.004	0.496	0.645	0.150	3.767
0.500	0.500	0.004	0.484	0.623	0.139	4.379
0.600	0.500	0.004	0.482	0.609	0.127	4.809
0.700	0.500	0.004	0.483	0.601	0.117	5.168
0.800	0.500	0.004	0.485	0.595	0.109	5.507
0.900	0.500	0.004	0.487	0.591	0.103	5.848
1.000	0.500	0.004	0.489	0.588	0.098	6.198

Table 8.2: Calculated quantities for various particles of various diameter a moving through the stagnation flow described by Taylor [22]. $|\bar{q_p}|$ and $|\bar{q_f}|$ are the average absolute particle and fluid velocity magnitudes respectively.

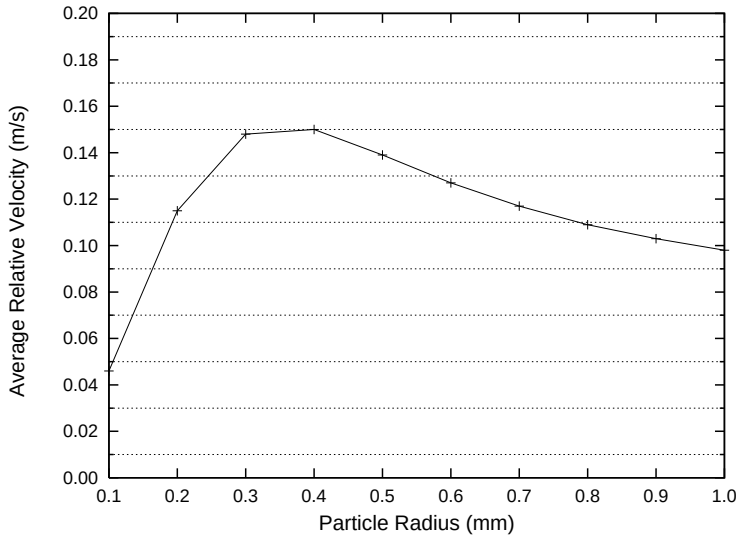

Figure 8.2: The average velocity relative to the fluid for particles of various diameter $2a$ moving through the stagnation flow described by Taylor [22].

It is important to bear in mind that (i) the relatively inaccurate LPA/Euler approximation was used, (ii) Stokes flow is assumed, (iii) the particle size a is coupled through an inverse proportionality to the freestream velocity. Velocities are calculated for a fixed simulated time t_s, so that average velocities for a particular input mainstream velocity can be compared.

Acknowledging these limitations, it can be seen that $|\bar{q}|$ initially increases with increasing particle radius a before decreasing slightly to a fixed value as a becomes large. This can be explained qualitatively as follows. Very light particles (e.g. $a = 0.01$ cm) move almost entirely with the fluid streamlines and so $|\bar{q}|$ is very small. As a grows larger, the particle begins to deviate from the fluid and cuts streamlines in areas of relatively high velocity gradients. As a continues to grow, the paths followed by successive particles become very similar (essentially straight lines) and cut the fluid streamlines in areas of relatively low velocity gradient, i.e. the relative velocity will be lower for larger particles. Small and light particles travel with the flow while large and heavy particles move bullet-like through the flow with very little deflection.

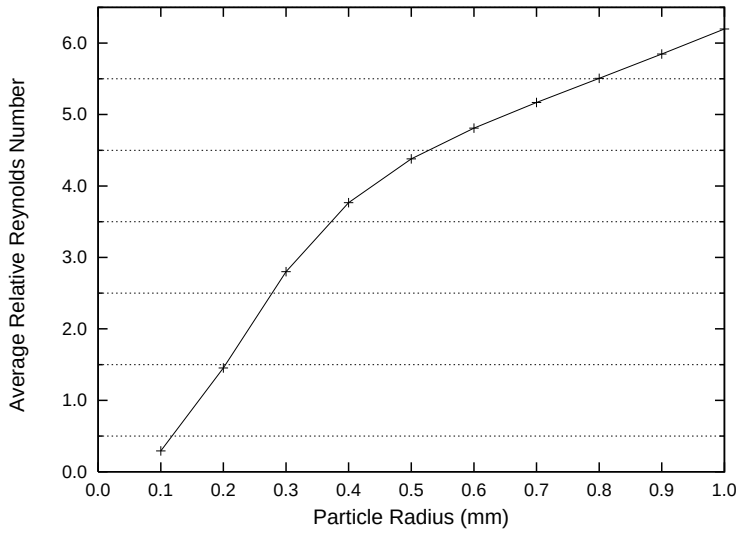

Figure 8.3: The average relative Reynolds number for particles of various diameter a moving through the stagnation flow described by Taylor [22].

It is further speculated that the total mass transfer from a particle moving through a velocity field may be a linear function of the maximum velocity or the difference between the maximum and minimum fluid velocities encountered, i.e. $m = \gamma(v_{\max})$ or $m = \gamma(v_{\max} - v_{\min})$. This is because the particle will have a velocity of at least the minimum velocity encountered in the fluid and at most the maximum velocity encountered. Since the mass transfer ought to be related to the average relative velocity between the particle and the fluid, it can be surmised that the average relative velocity $|\bar{q}|$ is perhaps a linear function of either $v_{\max}$ or $(v_{\max} - v_{\min})$.

Results do indicate that the average particle velocity for any given particle size seems to be a constant factor of the maximum fluid velocity encountered by the particle, becoming more stable as the particle size increases. The maximum fluid velocity magnitude ($q_{f,\,\max}$)) is always about 1.45 times the average absolute particle velocity magnitude for the Taylor flow, i.e. $\bar{q}_p \approx 1.45(q_{f,\,\max})$. This is not surprising since, as the particle size increases, a particle is more inclined to follow the same track and experience the same velocities; the ratio of the average particle velocity

and the maximum fluid velocity encountered by the particle should approach a constant. It seems that a similar curve should exist for all velocity fields.

8.2.1 Particle Size and Average Relative Reynolds Number, $\bar{Re}_p$

For very small particles, fluid and particle motion will be practically identical at each point in space, growing less similar with particle size until some critical value when the particle never moves very closely with the fluid. For small particles which move with the fluid, diffusion models, analytical and semi-analytical, are sufficient to estimate the mass transfer and the particle motion simulation ends at this point. There is no need for further calculation of the forced convective component of mass transfer.

The most important relationship is that between the size of the particle, as defined by its radius a, and the average relative Reynolds number ($\bar{Re}_p$) encountered. The two-dimensional information considered was produced, as described in Section 5.4.

These results indicate that this mechanism is extant; there is a threshold or critical a below which convective mass transfer can be ignored and an analytical diffusion mass transfer model applied. Extrapolating linearly from the two-dimensional plot in Figure 8.5, we can say that for particles of diameter less than 0.05 mm, or 50 microns, the relative Reynolds number is practically zero and so we posit that an analytical diffusion model can be be used for all particles of diameter 50 microns and less.

8.3 USP Dissolution Apparatus

8.3.1 Particle Size and Average Reynolds Number

Following from the two-dimensional case, a plot of a against $\bar{Re}_p$ for the three dimensional flow in a USP apparatus should produce a curve with $\bar{Re}_p$ high for

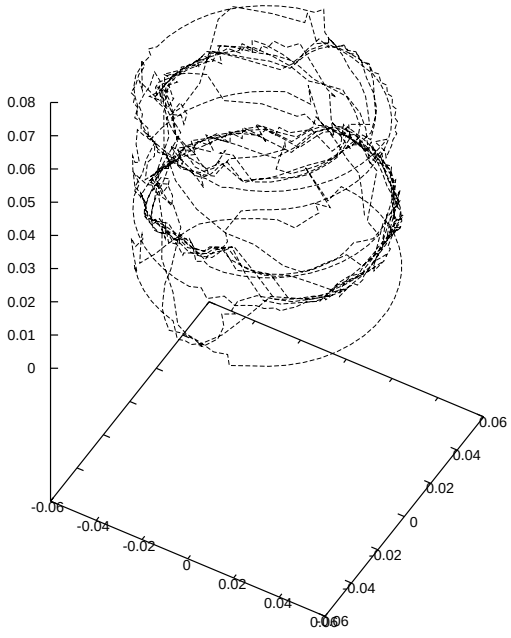

Figure 8.4: The streakline of a particle moving through the USP apparatus. Representing a 100 second run, this path was generated using the CGNS data provided by Deirdre D'Arcy at the School of Pharmacy in Trinity College Dublin [19]. Visualised for this thesis using GnuPlot.

large a and tending to zero as a tends to zero. And indeed, this behaviour can be clearly seen in Table 8.3 and Figure 8.5. Particle trajectories were calculated using a simple LPA/Euler integration scheme and a nearest-neighbour search algorithm. Particles are, however, not forced to the nearest node point after each time-step.

For particle diameters of 0.01 cm and smaller, the average relative Reynolds number is very small, less than 0.04, see Table 8.3; the average relative Reynolds number becomes small very quickly as the particle diameter decreases. This pattern is seen for both the two-dimensional stagnation flow and the three dimensional USP apparatus flow, shown in the diagram below.

a **(cm)**	$\bar{Re}_{\mathrm{p}}$	
	(i)	**(ii)**
0.01	0.291	0.036
0.03	2.800	0.815
0.05	4.379	3.254
0.07	5.168	7.595
0.09	5.848	13.496

Table 8.3: Particle sizes with corresponding average Reynolds number relative to the flow for (i) two-dimensional particle motion through a stagnation flow and (ii) particle motion through the three-dimensional velocity field with a USP apparatus (from data produced by Deirdre D'Arcy and others at the School of Pharmacy in Trinity College Dublin [19]).

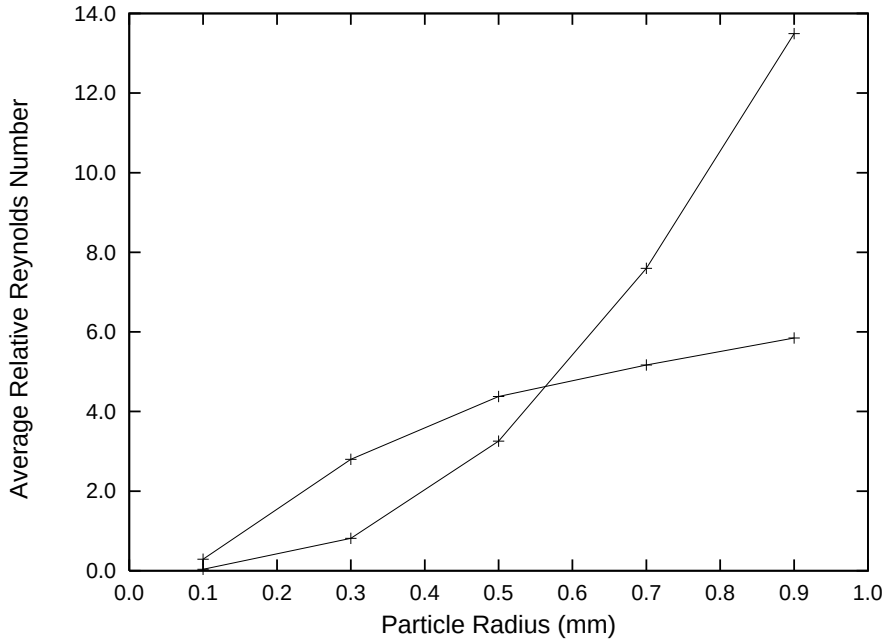

Figure 8.5: Particle sizes with corresponding average Reynolds number relative to the flow for (i) two dimensional particle motion through a stagnation flow and (ii) particle motion through the three dimensional velocity field with a USP apparatus (from data produced by Deirdre D'Arcy and others at the School of Pharmacy in Trinity College Dublin [19]). Note that the particle radii are given in mm.

Accepting that further work is required to validate these graphs, i.e. more simulation runs with denser grids, better implementation of the equations of motion as well as a more sophisticated interpolation scheme, we can think about the implications of these preliminary results.

One interesting observation is that a power series of the particle radius a can be fitted to the three-dimensional curve. This power series takes the form of $\bar{Re}_{\mathrm{p}} = A \times a^c$ where $c \approx 2.72$. A takes the value 19.94. Taking the curve $\bar{Re}_{\mathrm{p}} = A \times a^c$ to represent the relationship between Re_p and a (mm), then we can extend the table of values above (see Table 8.4) and Figure 8.4.

a **(cm)**	Re_p	a **(cm)**	$\bar{Re}_{\mathbf{p}}$
0.0001	1.39581E-07	0.006	0.009513568
0.0002	9.18568E-07	0.007	0.014465174
0.0003	2.76552E-06	0.008	0.020795153
0.0004	6.04499E-06	0.009	0.028642379
0.0005	1.10873E-05	0.01	0.038140891
0.0006	1.81996E-05	0.02	0.251000857
0.0007	2.76721E-05	0.03	0.755685126
0.0008	3.97814E-05	0.04	1.651808024
0.0009	5.47933E-05	0.05	3.029620975
0.001	7.29641E-05		
0.002	0.000480168		
0.003	0.001445636		
0.004	0.003159932		
0.005	0.005795708		

Table 8.4: Particle radii with corresponding average Reynolds number relative to the flow for particle motion through the three dimensional velocity field with a USP apparatus using the curve $Re_p = A \times a^c$, $c = 2.72$ and $A = 19.94$.

From this table we note that for a particle of diameter 0.01 cm (100 microns), the average relative Reynolds number $\bar{Re}_p$ is about 0.006, 7.29641×10^{-5} for a particle diameter of 0.002 cm (20 microns) and only 1.39581×10^{-7} for a particle diameter of 0.0002 cm (2 microns).

There is some overlap between the curve(s) produced from the three-dimensional USP flow field and the curve(s) produced in a two-dimensional stagnation flow for small a. It may not be absolutely necessary, for certain particle sizes, to conduct

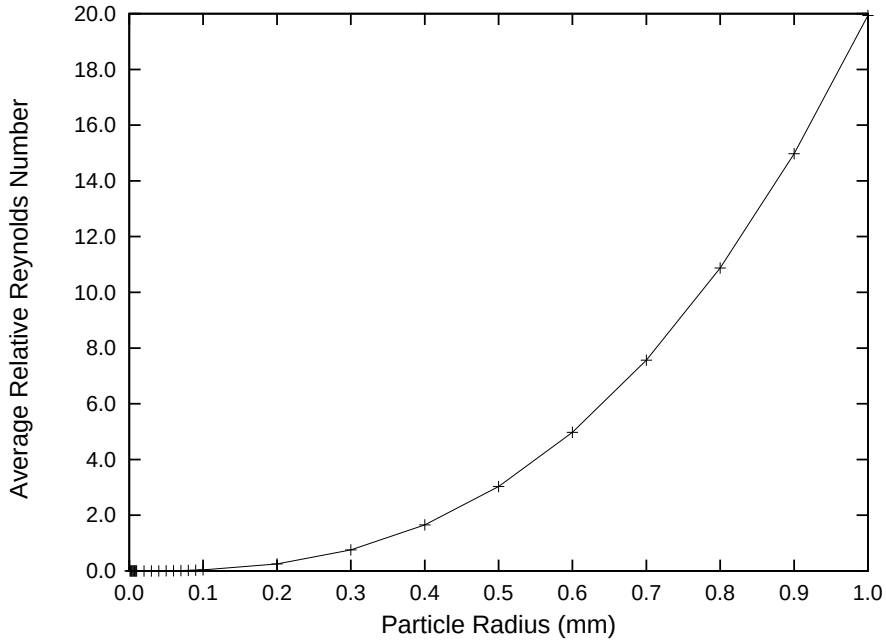

Figure 8.6: Particle sizes with corresponding average Reynolds number relative to the flow for particle motion through the three dimensional velocity field with a USP apparatus using the curve $Re_p = A \times a^c$, $c = 2.72$ and $A = 19.94$. Note that the particle radii are given in mm.

three-dimensional simulations; a single curve may suffice to describe the relationship between a and $\bar{Re}_{\mathrm{p}}$ in all flows.

The mass transfer rate can be calculated piece-wise after each time-step Δt using an experimental correlation. In addition, when the relative Reynolds number is very low, there is no need to calculate its motion through the fluid and a radial diffusion model can be used.

8.3.2 Mass Transfer from a Particle in the USP Apparatus

Average mass transfer rates were calculated for particles of various diameters using experimental correlations, together with the quantities presented in Table 8.5 [254; 255; 256; 257]. Forced convective results were generated using the average relative Reynolds numbers, presented in Section 8.3.1. Important dimensionless

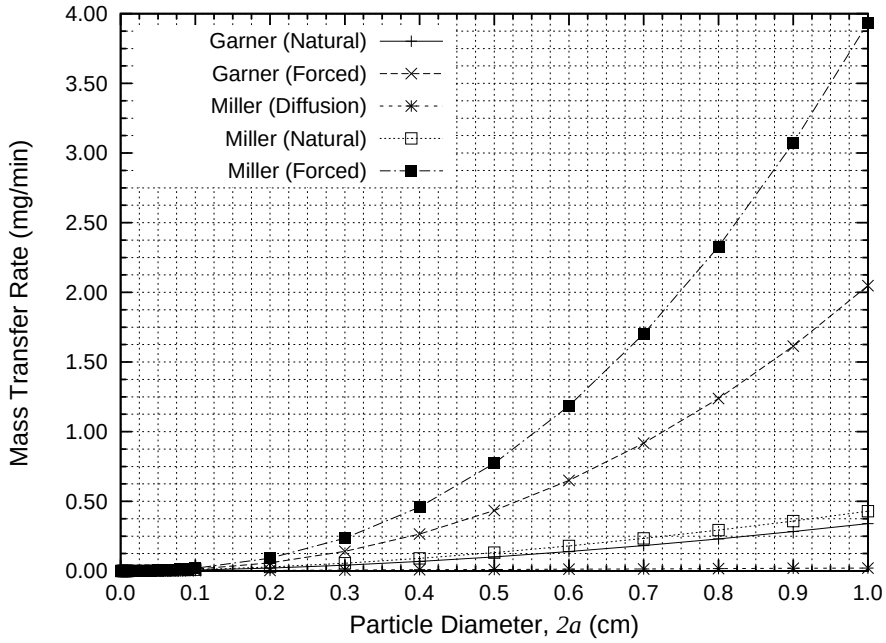

Figure 8.7: Average mass transfer rates for particles of various diameters using experimental correlations and the quantities presented in Table 8.5 [254; 255; 256; 257]. Forced convective results were generated using the average relative Reynolds numbers presented in the Section 8.3.1. Garner's natural convection model and Miller's diffusion model converge to the same values for small particle sizes and are superimposed in this figure.

groups include the Reynolds number (Re_p), Schmidt number (Sc), Grashof number ($G' = \frac{8ga^3}{\nu^2}\frac{\Delta\rho}{\rho}$) and the average Sherwood number, $Sh_p = \frac{2ah_m}{D_{AB}}$. Results are presented in Figures 8.7, 8.8 and 8.9.

Quantity		**Value**	
ρ	(HCl)	1.186	g cm^{-3}
ν	(HCl)	7.870×10^{-3}	cm^2 s^{-1}
C_s	(Benzoic Acid)	4.550×10^{-3}	g cm^{-3}
$\Delta\rho$	(Benzoic Acid in HCl)	1.990×10^{-3}	g cm^{-3} [258]
D	(Benzoic Acid in HCl)	1.236×10^{-5}	cm^2 s^{-1}
g		980	cm s^{-2}

Table 8.5: Values of important quantities for the problem under consideration. The solute is benzoic acid and the solvent is 0.1M HCl.

Miller reports Harriott's finding that radial diffusion becomes the dominant mode

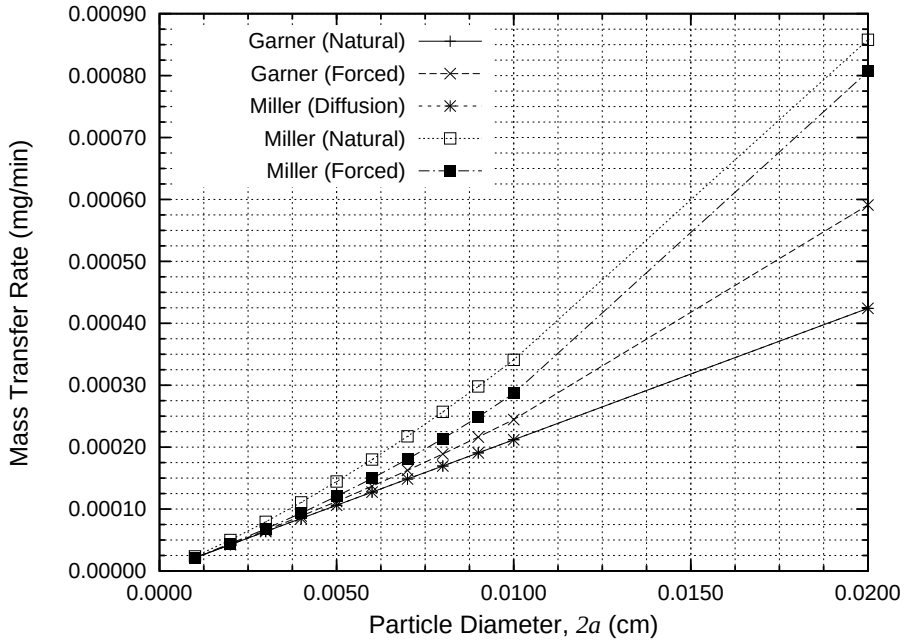

Figure 8.8: Mass transfer rates for particles of diameter 200 microns and smaller using experimental correlations and the quantities presented in Table 8.5 [254; 255; 256; 257]. Forced convective results were generated using the average relative Reynolds numbers presented in the Section 8.3.1. Garner's natural convection model and Miller's diffusion model converge to the same values for small particle sizes and are superimposed in this figure.

of mass transfer for particles of diameter 205 microns and less [255; 256; 257]. From our numerical study of the average relative Reynolds number of particles of various sizes moving through the USP apparatus, presented in Section 8.3, we estimated that radial diffusion becomes the principal mode of mass transfer for particles of diameter 200 microns and smaller. This is close to Harriott's figure. In this section we used mass transfer correlations to estimate the mass transfer from particles for the case of free (natural) and forced convection as well as for diffusion-only transfer. From Figure 8.7 it can be seen that, for large particles, forced convection is the dominant mode of mass transfer. For small particles, natural convection dominates as the primary mode of mass transfer (Figure 8.8) and for particles of diameter 100 microns and smaller, radial diffusion dominates (Figure 8.9).

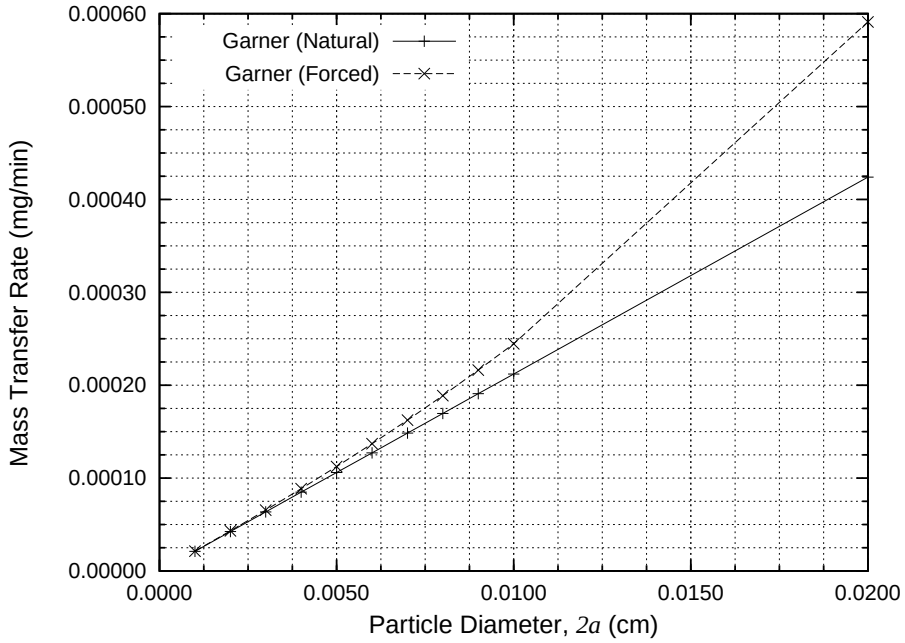

Figure 8.9: Mass transfer rates for particles of diameter 200 microns and smaller using only the experimental correlations of Garner [254] together with the quantities presented in Table 8.5. Forced convective results were generated using the average relative Reynolds numbers presented in the Section 8.3.1.

From Figure 8.8, we can see that there is no need to calculate the trajectory of particles smaller than 100 microns through the USP apparatus as a radial diffusion model [see e.g. 254; 257; 102] will be sufficiently accurate.

8.4 Errors and Additional Considerations

8.4.1 Calculation Stability

Results indicate that the relative Reynolds numbers for small particles are similar for two-dimensional and three-dimensional flows. However, filling in the 3D data in this region leads to the same recurring problem: the LPA/Euler and Verlet integration schemes require ever smaller timesteps as the particle size decreases to maintain stability. This means that for a given number of timesteps, the total simulation time is reduced and the average Reynolds number is computed over smaller times.

It is useful to consider what causes this problem.

8.4.2 Effect of t_s on $\bar{Re}_p$

It was observed that varying Δt leads to different average relative Reynolds Numbers, $\bar{Re}_p$. This is sensible: as t_s increases, $\bar{Re}_p$ should converge on a fixed value. It is also reasonable to think that this value will be different to $\bar{Re}_p$ calculated over shorter t_s. This is because, for small simulated times, a particle will have moved only a small distance through the velocity field and sudden changes in the velocity field, i.e. high or low relative Reynolds Numbers, have a much larger effect on $\bar{Re}_p$ calculated over that period. For longer simulated times, $\bar{Re}_p$ approaches a constant as the simulated time increases.

8.4.3 Additional Assumptions and Shortcomings of the Models

8.4.4 Considering Many Particles

At present we have considered a single particle moving through simple velocity fields. However, even with many drug particles moving in the USP apparatus, the particles may be distributed sparsely enough to allow us still neglect particle-particle interactions and particle-fluid effects. We do not have enough experimental information yet to state this with confidence.

If this is not the case, i.e. particles are not distributed sparsely enough, then there may be complicated interactions between the particles and the fluid and the problems of particle motion and fluid motion may indeed be coupled. The problem of calculating such fluid and particle motion within the USP apparatus is certainly not a trivial one. This is further complicated by the fact that the particles dissolve as they move through the fluid, meaning that a complete solution to the problem will involve a multiphysics approach. A complete, detailed, solution that captures these interactions is likely to require more sophisticated mathematical analysis, numerical algorithms and computational implementations, e.g. parallel implementation. The

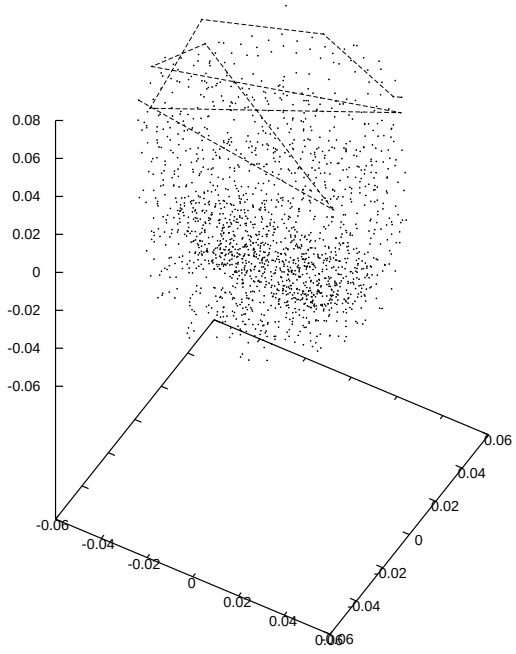

Figure 8.10: When the timestep is too large, e.g. 1 second as shown here, the particle covers almost half the width of the USP apparatus in one step. This quickly becomes unstable.

work set out here was to produce a useful model and a good foundation for future development.

8.4.5 Analytical Limits

There is the possibility of running up against *analytical limits*. An analytical limit in this context is understood to be the limit of a simulation's ability to correctly capture the physics of a process: when the simulation of a process begins to deviate significantly from the actual process and the simulation is no longer valid. It is certain that the simulations presented here, as with all simulations, do not capture all

the physics of the process we are investigating. This makes it all the more important to have realistic expectations of the models' capabilities and to understand their limitations.

8.5 Chapter Summary and Conclusions

In summary, this chapter presented results from the last of the three studies described in this thesis.

Calculations indicate that small particles move with the USP apparatus flow and that, for particles with a diameter of approximately 0.01 cm (100 microns) and smaller, radial diffusion is the dominant mode of mass transfer, i.e. *forced convection effects can be neglected for particles of diameter 100 microns and smaller.* This result is, it is believed, novel for the case of particle dissolution in the USP apparatus. Importantly, this study contributes to the basis for arguing that simulation is useful in the description of pharmaceutical processes.

8.5.1 Future Work

Proposed Complete Solution to the Problem of Drug Particle Dissolution in the USP Type 2 Dissolution Apparatus

The aim of this work was to begin the development of a particle trajectory tracing algorithm which can be used to predict the paths of and dissolution from tablet fragments of various sizes moving in the USP Type 2 Dissolution Apparatus. In a complete model, it is proposed that the initial drug particle size distribution could be determined through the use of experimental data and a probabilistic model. The particle motion and dissolution rate could be determined using classical particle tracking techniques together with a simulated fluid velocity field. These components: probabilistic model, particle tracking and a simulated velocity field, could together form a complete model of drug fragmentation. Together with the work on the initial

dissolution rate, this could form part of a complete model of tablet dissolution. Given a time-dependent distribution of particle sizes and a fluid velocity field, it should be possible to estimate the overall dissolution rate of a tablet dissolving and then fragmenting in a USP dissolution apparatus.

Outline of Probabilistic Component

A complete model of dissolution in a USP apparatus may require a probabilistic component. As discussed previously, there is significant variability in the dissolution rates of tablets dissolving in this standard dissolution test apparatus. This variability results from inherent factors in the operation of the dissolution apparatus and in the tablet itself, i.e. tablets may or may not disintegrate into fragments and those that do so will disintegrate at varying rates. The idea is that the probabilistic component, which may use an Inverse Monte Carlo technique in a Bayesian framework, adjusts the model at each time-step using a probable distribution of fragment sizes informed by and validated against concentration measurements and other data from experiment. This is based on previous work, e.g. [112; 113]. After each run, the distribution of particle sizes is corrected using an Inverse MC method.

A Possible Inverse Monte-Carlo Method

If a key result, e.g. the mass transfer rate, from the model is $M(x)$ and the true, measured, value from the physical system is denoted M_{True}, then the error E_{sys} between the simulated and actual systems will be $M - M_{\text{True}} = E_{\text{sys}}$. If a set of n values for M is obtained for n different x values, the Euclidean distance between the simulated and true values can be calculated for each instance. Instances with small distances are most likely. This information can be used to determine which possible combinations of system parameters are most useful and this, in turn, can be used to set these parameters so that further predictions can be made for a new set of initial conditions.

Chapter 9

Summary, Future Work and Conclusions

9.1 Summary

9.1.1 Study 1

The first study developed the understanding of quasi-steady drug dissolution from the surface of a multi-layered tablet in the USP apparatus. A Crank-Nicolson finite-difference approximation to the drug mass transfer rate from dissolving cylindrical *tablets*, consisting of alternating layers of drug and inert material, was presented and results were compared with recent solutions to the same problem and with previous experimental results produced using the USP apparatus. It was shown that (i) the theoretical estimates differ by up to 10%, a result of different implementations of a derivative surface boundary condition, (ii) the new finite-difference model is more physically realistic but that the recent analytical solution of Crane et al is shown to be usefully accurate. In addition, it was established that the assumption of a steady, axial mainstream flow is likely to be the primary reason for the error between the experimental and theoretical results.

9.1.2 Study 2

The second study investigated the flow around the top of a cylinder using a commercial fluid dynamics code. A specific application to a complementary problem in wind energy was considered. In addition to other sources of error, accelerated airflow, or *speed-up*, around the top of cylindrical meteorological (*met*) towers can cause incorrect wind-speed measurements. A particular configuration was considered where the anemometer was located only two tower diameters above a met tower. Using a standard computational fluid dynamics package, the maximum error for this configuration was found to be 2% of the wind-speed. It was concluded that top-mounted anemometers should be located at the windward side of a meteorological tower, where a particular wind direction prevails, and at least five diameters above the top. This will reduce speed-up to less that 1%. The IEA recommendation is for a minimum separation of about 6 tower diameters [203]. In line with the IEA's recommendation that the anemometer installation should be 'clean' [203], it is recommended that towers should be made from a corrosion resistant material and maintained and cleaned regularly to minimise flow disturbance.

9.1.3 Study 3

The third part of this work considered one possible end state for a dissolving tablet: fragmentation into small particles with dissolution continuing from the disintegrated solid masses. A framework for calculating the motion of and dissolution from a drug particle moving through the USP apparatus was outlined, beginning with a review of the classical work of Taylor and Glauert, who considered the motion of raindrops in airflows. Calculations indicate that small particles move with the USP apparatus flow and that, for particles of diameter of approximately 0.01 cm (100 microns) and smaller, radial diffusion is the dominant mode of mass transfer, i.e. *forced convection effects can be neglected for particles of diameter 100 microns and smaller.*

9.2 Future Work

The potential areas of research arising from this thesis are many. Specific and general suggestions include:

9.2.1 Specific Research Questions

Arising from Study 1

Future developments of this work must incorporate boundary-layer theory close to the surface using a more realistic free-stream velocity field, ideally calculated concurrently using a computational fluid dynamics code. Further research may also include: (i) exploring the limits of validity for the Pohlhausen solution, to further clarify the reasons for its deviation from the CN solution and to formally demonstrate that its convergence as the number of layers becomes very large can be written in a closed form; (ii) formulating other applications for the extended Pohlhausen solution. This may have some utility when considering matrix tablets, i.e. a large number of layers may approximate matrix tablet behaviour. Other applications might include microelectrode analysis; (iii) the CN finite-difference method can be extended in many ways including the already mentioned consideration of more realistic flows from a coupled CFD code. There are many outstanding investigations around the CN scheme, including, e.g. detailed investigations of its validity and incorporation of more efficient mesh distributions.

Arising from Study 2

Future work arising from the second study may include, in the area of wind energy, several essential refinements of the work presented; these include extending the analysis for different tower and anemometer configurations and for different tower types, e.g. considering the error in wind-speed measurements from anemometers mounted close to the *side* of a meteorological tower. Another useful study will be to

use more sophisticated turbulence models and to carry out a more complete study of the effect of turbulence on the wind-speed close to the tower. The use of similar techniques to examine the mass transfer from a cylindrical tablet in cross-flow may also be a useful avenue of research.

Arising from Study 3

Many research directions arise from the particle tracking work. These include (i) developing a more sophisticated CGNS based code (ii) investigating OpenFOAM as a platform for conducting this work, (iii) using more sophisticated algorithms which incorporate particle-particle interactions and so forth in particle tracking, (iv) considering a parallel version of the code and (v) integrating this work with a probabilistic framework.

9.3 Conclusions

The three main studies, (1) quasi-steady drug dissolution from a multi-layered tablet in the USP apparatus, (2) flow distortion about a cylinder and (3), the mass transfer from small particles moving in the USP apparatus, each form a part of a future complete framework for simulating drug dissolution in the USP apparatus. These investigations were consistent with our aim of building on earlier understanding of drug dissolution in the USP apparatus and to demonstrate the thesis that simulation has the potential to be of significant use for pharmaceutics.

Bibliography

[1] F. Norton, The art of writing scientific reports, TM 7, NACA (1921).

[2] A. Roland, Model Research, NASA, Scientific and Technical Information Branch, Washington, D.C., 1985, Ch. Volume 2, Appendix F, Research Authorization 201.
URL `http://history.nasa.gov/SP-4103/contents.htm`

[3] R. Langer, Drug delivery and targeting, Nature (392) (1998) 5 – 10, (Supp).

[4] IBM Business Consulting Services, Pharma 2010: The threshold of innovation, Executive brief, IBM Institute for Business Value (2004).

[5] H. A. Mucke, A new paradigm for clinical development: The clinical trial in 2015, Advances in Life Sciences Reports 58, Cambridge Healthtech Advisors (CHA) (2005).

[6] D. E. Leahy, Drug discovery information integration: virtual humans for pharmacokinetics, Biosilico 2 (2) (2004) 78–84.

[7] M. Aulton, Pharmaceutics, the Science of Dosage Form Design, 2nd Edition, Churchill-Livingstone, Edinburgh etc., 2002.

[8] V. Pillay, R. Fassihi, Unconventional dissolution methodologies, J. Pharm. Sci. 88 (9) (2000) 843 – 851.

[9] T. Mirza, Y. Joshi, Q. Liu, R. Vivilecchia, Evaluation of Dissolution Hydrodynamics in the USP, Peak^{tm} and Flat-Bottom Vessels Using Different Solubility Drugs, Tech. rep., Diss. Tech., Article 2 (Feb 2005).

[10] United States Pharmacopeial Convention, USP-NF 24, 19th Edition, Rockville, MD, 2000, Ch. Dissolution <711>, p. 1941.

[11] W. Higuchi, N. Mir, S. Desai, Dissolution rates of polyphase mixtures, J. Pharm. Sci. 54 (1965) 1405 – 1410.

[12] A.-M. Healy, O. Corrigan, The influence of excipient particle size, solubility and acid strength on the dissolution of an acidic drug from two-component compacts, Int. J. Pharm. 143 (1996) 211–221.

[13] Z. Ramtoola, O. Corrigan, Dissolution characteristics of benzoic acid and salicylic acid mixtures in reactive Media, Drug Dev. Ind. Pharm. 13 (1987) 1703–1720.

[14] A.-M. Healy, O. Corrigan, Predicting the dissolution rate of ibuprofen-acidic excipient compressed mixtures in reactive media, Int. J. Pharm. 84 (2) (1992) 167–173.

[15] S. A. Qureshi, J. Shabnam, Cause of high variability in drug dissolution testing and its impact on setting tolerances, Eur. J. Pharm. Sci. 12 (3) (2001) 271 – 276.

[16] J. Kukura, J. Baxter, F. Muzzio, Shear distribution and variability in the USP Apparatus 2 under turbulent conditions, Int. J. Pharm. 279 (1-2) (2004) 9 – 17.

[17] M. Crane, N. J. Hurley, L. Crane, A.-M. Healy, O. I. Corrigan, K. M. Gallagher, L. G. McCarthy, Simulation of the USP drug delivery problem us-

ing CFD: Experimental, numerical and mathematical aspects, Simul. Model. Pract. Th. 12 (2) (2004) 147–158.

[18] J. Baxter, J. Kukura, F. Muzzio, Hydrodynamics-induced variability in the USP apparatus II dissolution test, Int. J. Pharm. 292 (1-2) (2005) 17–28.

[19] D. D'Arcy, O. Corrigan, A. Healy, Hydrodynamic simulation (computational fluid dynamics) of asymmetrically positioned tablets in the paddle dissolution apparatus: impact on dissolution rate and variability, J. Pharm. Pharmacol. 57 (10) (2005) 1243 – 1250(8).

[20] PSUDO, Final report, Tech. rep., Parallel Simulation of Drug release code (PSUDO) Project (2000).
URL `http://icetact.tchpc.tcd.ie/icetact/examples/PSUDOfinal.html`

[21] M. Crane, L. Crane, A.-M. Healy, O. Corrigan, K. Gallagher, L. McCarthy, A Pohlhausen Solution for the Mass Flux From a Multi-layered Compact in the USP Drug Dissolution Apparatus, Simul. Model. Pract. Th. 12 (6) (2004) 397–411.

[22] G. Taylor, Notes on possible equipment and technique for experiments on icing on aircraft, ARC R & M 2024.

[23] M. Glauert, A Method of Constructing the Paths of Raindrops of Different Diameters moving in the neighbourhood of (1) a Circular Cylinder, (2) an Airfoil, placed in a Uniform Stream of Air ; and a Determination of the Rate of Deposit of Drops on the Surface and the Percentage of Drops Caught, ARC R & M 2025.

[24] Int. J. Pharm., Journal Information, Product Description [Online], Int. J. Pharm.[Viewed 15 March 2006].
URL `www.elsevier.com/locate/ijpharm/`

[25] R. Borchardt, A. Repta, V. Stella, Directed Drug Delivery: A Multidisciplinary Problem, Humana Press, Clifton, NJ, USA, 1985, Ch. 1.

[26] J. R. Robinson, Pharmaceutics and the evolving technology of drug delivery - a perspective, in: R. T. Borchardt, A. J. Repta, V. J. Stella (Eds.), Directed Drug Delivery, a Multidisciplinary Problem, Humana Press, New Jersey, 1984.

[27] J. Drews, Drug discovery: A historical perspective, Science 287 (2000) 1960–1964.

[28] R. Langer, Where a pill won't reach, Sci. Am. 288 (4) (2003) 32 – 39.

[29] R. Langer, Langer discusses drug delivery advances at AMA briefing, MIT News Office [Accessed March 15 2006].
URL http://web.mit.edu/newsoffice/2004/langer.html

[30] V. J. Stella, My mentors, J. Pharm. Sci. 90 (2001) 969–978.

[31] R. L. Juliano, Drug Delivery Systems - Characteristics and Biomedical Applications, Oxford University Press, New York, Oxford, 1980, Ch. 1.

[32] R. Langer, Polymer-controlled drug delivery systems, Accounts Chem. Res. 26 (1993) 537–542.

[33] S. Abdul, S. Poddar, A flexible technology for modified release of drugs: multi layered tablets, J. Control. Release 97 (3) (2004) 393–405.

[34] GlaxoSmithKline, Our history (Webpage), [Online, accessed 13th February 2006] (2006).
URL http://www.gsk.com/about/history.htm

[35] R. Blythe, Sympathometic preparation, United States Patent and Trademark Office, Patent 2,738,303 (March 13, 1956).

[36] M. Gohel, M. Panchal, Quantitative expression of deviation from zero-order drug release, Pharmaceutical Technology 25 (9) (2001) 62–74.

[37] J. Siepmann, A. Göpferich, Mathematical modeling of bioerodible, polymeric drug delivery systems, Adv. Drug Deliver. Rev. 48 (2-3) (2001) 229–247.

[38] A. Streubel, J. Siepmann, N. A. Peppas, R. Bodmeier, Bimodal drug release achieved with multi-layer matrix tablets: transport mechanisms and device design, J. Control. Release 69 (3) (2000) 455–468.

[39] U. Conte, L. Maggi, P. Colombo, A. La Manna, Multi-layered hydrophilic matrices as constant release devices (Geomatrix™ systems), J. Control. Release 26 (1) (1993) 39–47.

[40] Y. Qiu, N. Chidambaram, K. Flood, Design and evaluation of layered diffusional matrices for zero-order sustained release, J. Control. Release 51 (2-3) (1998) 123–130.

[41] U. Conte, L. Maggi, Modulation of the dissolution profiles from Geomatrix multi-layer matrix tablets containing drugs of different solubility, Biomaterials 17 (1996) 889–896.

[42] SkyePharma, Geomatrix, [Online], [10 November 2006] (2006).
URL `http://www.skyepharma.com/oral.html`

[43] S. A. Qureshi, I. J. McGilveray, Typical variability in drug dissolution testing: study with USP and FDA calibrator tablets and a marketed drug (glibenclamide) product, Eur. J. Pharm. Sci. 7 (1999) 249 – 258.

[44] L. McCarthy, G. Bradley, J. Sexton, O. Corrigan, A. Healy, Computational fluid dynamics modeling of the paddle dissolution apparatus: Agitation rate, mixing patterns, and fluid velocities, AAPS PharmSciTech 5 (2).

[45] Y. Wu, O. Kildsig, E. Ghaly, Effect of hydrodynamic environment on tablets dissolution rate, Pharm. Dev. Technol. 9 (1) (2004) 25 – 37.

[46] Tufts Center for the Study of Drug Development, Tufts center for the study of drug development pegs cost of a new prescription medicine at $802 million, Press Release.
URL http://csdd.tufts.edu/NewsEvents/RecentNews.asp?newsid=6

[47] M. Dickson, J. Gagnon, Key factors in the rising cost of new drug discovery and development, Nat. Rev. Drug Discov. 3 (2004) 417 – 429.

[48] J. DiMasi, R. Hansen, H. Grabowski, The price of innovation: new estimates of drug development costs, J. Health Econ. 22 (2) (2003) 151–185.

[49] R. G. Frank, New estimates of drug development costs, J. Health Econ. 22 (2003) 325–330.

[50] R. Mullin, Drug development costs about $1.7 billion, Chemical & Engineering News 81 (50) (2003) 8.
URL http://pubs.acs.org/cen/topstory/8150/8150notw5.html

[51] J. DiMasi, Risks in new drug development: Approval success rates for investigational drugs, Clin. Pharmacol. Ther. 69 (5) (2001) 297–307.

[52] G. M. Grass, P. J. Sinko, Physiologically-based pharmacokinetic simulation modelling, Adv. Drug Deliver. Rev. 54 (2) (2002) 433–451.

[53] PhRMA, What goes into the cost of prescription drugs?, Report, The Pharmaceutical Research and Manufacturers of America (PhRMA) (June 2005).
URL http://www.phrma.org/files/Cost_of_Perscription_Drugs.pdf

[54] C. George, J. M. Pearson, Riding the pharma roller coaster, The McKinsey Quarterly (4).

[55] Food and Drug Administration, Drug Approval Application Process, Website, U.S. Department of Health and Human Services (2006).
URL http://www.fda.gov/cder/regulatory/applications/

[56] M. Pandey, Investment decisions in pharmaceutical R&D projects, Drug Discov. Today 8 (21) (2003) 968–971.

[57] European Medicines Agency (EMEA), Questions and answers on recommendation for refusal of marketing application for Atryn, Press Release, document reference: EMEA/62022/2006 (February 2006).

[58] M. Peplow, Drug from GM animal gets thumbs down, Nature [Online].
URL doi:10.1038/news060220-17

[59] K. Honey, The comeback kid: TYSABRI now FDA approved for Crohn disease, J. Clin. Invest. 118 (3) (2008) 825–826.
URL http://dx.doi.org/10.1172/JCI35179

[60] Food and Drug Administration, Natalizumab (marketed as Tysabri) information (2005) 825–826.
URL http://www.fda.gov/cder/drug/infopage/natalizumab/default.htm

[61] W. Russell, R. Burch, The Principles of Humane Experimental Technique, Methuen & Co, London, 1959.

[62] S. Laville, One year on from schoolboy's fightback, animal rights activists are forced to rethink tactics, The Guardian (2007) February 26.
URL http://www.guardian.co.uk/animalrights/story/0,,2021453,00.html

[63] F. P. Gruber, T. Hartung, Alternatives to Animal Experimentation in Basic Research, ALTEX Archive Sup. 1 (1) (2004) .

[64] V. Robinson, Finding alternatives: an overview of the 3Rs and the use of animals in research, School Science Review 87 (2005) 319.

[65] European Union, Seventh Framework Programme for Research.
URL http://cordis.europa.eu/fp7/home_en.html

[66] D. R. Chapman, H. Mark, M. W. Pirtle, Computers vs. wind tunnels for aerodynamic flow simulations, Astronaut. Aeronaut. 13 (1975) 22–35.

[67] E. A. Muenger, Searching the Horizon, A History of Ames Research Center 1940-1976, Scientific and Technical Information Branch, NASA, Washington, D.C., 1985.
URL http://history.nasa.gov/SP-4304/sp4304.htm

[68] T. C. Bickel, H. Morgan, C. Peterson, Applications of computational mechanics at Sandia National Laboratories, in: Computational fluid and solid mechanics, 2005, Proceedings of the Third M.I.T. Conference on Computational Fluid and Solid Mechanics, held in Cambridge, Massachusetts, USA, June 14 - 17, 2005.

[69] A. Jameson, The Role of CFD in Preliminary Aerospace Design, in: 4th ASME-JSME Joint Fluids Engineering Conference, Honolulu, Hawaii, 2003.

[70] C. A. Fletcher, Computational Techniques for Fluid Dynamics 1: Fundamental and General Techniques, 2nd Edition, Springer-Verlag, Berlin, 1991, 6th Printing, 2005.

[71] IBM Business Consulting Services, Pharma 2005: Silicon rally, the race to e-R&D, Report, IBM Global Services, Originally published in 1999 by PricewaterhouseCoopers (PwC) (2002).

[72] B. Ataie-Ashtiani, S. Hosseini, The completed human genome: implications for chemical biology, Curr. Opin. Chem. Biol. 7 (4) (2003) 511–515.

[73] C. A. Hunt, S. Guzy, D. L. Weiner, A forecasting approach to accelerate drug development, Stat. Med. 17 (15-16) (1998) 1725–1740.

[74] S.-S. Feng, S. Chien, Chemotherapeutic engineering: Application and further development of chemical engineering principles for chemotherapy of cancer and other diseases, Chem. Eng. Sci. 58 (2003) 4087–4114.

[75] Entelos, Inc., Entelos Announces U.S. Patent for the Development and Use of Virtual Patients, Press Release.
URL http://www.entelos.com/news/pressArchive/press72.html

[76] T. S. Paterson, A. L. Bangs, Method and apparatus for conducting linked simulation operations utilizing a computer-based system model, United States Patent and Trademark Office, Patent 6,983,237 (US2006031059) (February 9, 2006).

[77] D. Teather, Virtual patient firm opts for Aim, The Guardian (2006) March 7.
URL http://business.guardian.co.uk/story/0,,1725167,00.html

[78] J. Russell, Optimizing Optimata, Bio-IT World (November 15, 2005).
URL http://www.bio-itworld.com/issues/2005/nov/russell-transcript/

[79] K. Skomorovski, H. Harpak, A. Ianovski, M. Vardi, T. P. Visser, S. C. Hartong, H. H. van Vliet, G. Wagemaker, Z. Agur, New TPO treatment schedules of increased safety and efficacy: pre-clinical validation of a thrombopoiesis simulation model, Brit. J. Haematol. 123 (4).

[80] P. Wellstead, Schrödinger's legacy: Systems and life, An E.T.S. Walton Lecture given as part of the W.R. Hamilton Bi-Centenary Lecture Series, The Royal Irish Academy (April 2005).

URL http://www.hamilton.ie/systemsbiology/files/2005/schroedinger.pdf

[81] G. S. Mack, Can complexity be commercialized?, Nat. Biotechnol. 22 (2004) 1223–1229.

[82] W. Russell, R. Burch, The Principles of Humane Experimental Technique, 2nd Edition, Universities Federation for Animal Welfare, Hertfordshire, 1992.
URL http://altweb.jhsph.edu/publications/humane_exp/het-toc.htm

[83] NC3Rs, The 3Rs, [Online], [April 18th 2006] (2006).
URL http://www.nc3rs.org.uk/

[84] The Human Genome Program, Genome Programs of the U.S. Department of Energy Office of Science, Website, U.S. Department of Energy Office of Science (2006).
URL http://www.doegenomes.org/

[85] E. Crampin, M. Halstead, P. Hunter, P. Nielsen, N. Noble, D amd Smith, M. Tawhai, Computational physiology and the physiome project, Exp. Physiol. 89 (1) (2004) 1 – 26.

[86] G. L.-T. Chiu, M. Gupta, A. K. Royyuru, Blue Gene, Preface, IBM J. Res. Dev. 49 (2/3).
URL doi:10.1147/rd.492.0191

[87] A. Noyes, W. Whitney, The Rate of Solution of Solid Substances in their own Solutions, J. Am. Chem. Soc. 19 (1897) 930–934.

[88] J. Wang, D. R. Flanagan, General Solution for Diffusion-Controlled Dissolution of Spherical Particles. 1. Theory, J. Pharm. Sci. 88 (7) (1999) 731–738.

[89] L. Prandtl, Motion of fluids with very little viscosity, TM 452, NACA (1928).

[90] W. Nernst, Theorie der Reaktionsgeschwindigkeit in Heterogenen Systemen, Z. Physik. Chem. 47 (1904) 52–55.

[91] E. Brunner, Reaktionsgeschwindigkeit in Heterogenen Systemen, Z. Physik. Chem. 47 (1904) 56–102.

[92] C. V. King, Reaction rates at solid–liquid interfaces, J. Am. Chem. Soc. 57 (1935) 828–831.

[93] L. Prandtl, Über Flüssigkeitsbewegung bei sehr kleiner Reibung, Verh. III. Intern. Math. Kongr., Heidelberg, 1904 (1905) 484–491.

[94] J. Crank, Mathematics of Diffusion, 2nd Edition, Oxford University Press, Oxford, 1975.

[95] C. C. Sun, Quantifying errors in tableting data analysis using the Ryshkewitch equation due to inaccurate true density, J. Pharm. Sci. 94 (2005) 2061–2068.

[96] S. W. Yu, L. J. van Vliet, H. W. Frijlink, K. van der Voort Maarschalk, The determination of relative path length as a measure for tortuosity in compacts using image analysis, Eur. J. Pharm. Sci. 28 (5) (2006) 433–440.

[97] P. J. O'Dowd, O. I. Corrigan, Dissolution kinetics of three component non-disintegrating compacts: theophylline, benzoic acid and salicylamide, Int. J. Pharm. 176 (2) (1999) 231–240.

[98] B. Killen, O. Corrigan, Factors influencing drug release from stearic acid based compacts, Int. J. Pharm. 228 (1-2) (2001) 189–98.

[99] E. Kenny, A moving boundary finite element solution of a pharmaceutical drug delivery problem, Msc. thesis, Trinity College, University of Dublin (1994).

[100] Hitachi Europe, European Esprit grant awarded to Hitachi Dublin Laboratory & Trinity College Dublin, Press Release (August 1998).
URL `http://www.hitachi.com/New/cnews/E/1998/980820B.html`

[101] C. Vuik, C. Cuvelier, Numerical solution of an etching problem, J. Comput. Phys. 59 (1985) 247–263.

[102] F. P. Incropera, D. P. DeWitt, Fundamentals of Heat and Mass Transfer, Fifth Edition, John Wiley & Sons, New York, 2002.

[103] P. Scott, Geometric irregularities common to the dissolution vessel, Diss. Tech. 12 (1) (2005) 18–21.

[104] A.-M. Healy, L. McCarthy, K. Gallagher, O. Corrigan, Sensitivity of dissolution rate to location in the paddle dissolution apparatus, J. Pharm. Pharmacol. 54 (3) (2002) 441–444.

[105] L. McCarthy, C. Kosiol, A.-M. Healy, G. Bradley, J. Sexton, O. Corrigan, Simulating the Hydrodynamic Conditions in the United States Pharmacopeia Paddle Dissolution Apparatus, AAPS PharmSciTech 4 (2).

[106] Fluent Inc., FLUENT User's Guide, Lebanon, NH, USA (2003).

[107] A. Lévêque, Les lois de la transmission de chaleur par convection, Ann. des Mines Mémoires, Tome XIII (13) (1928) 201 – 239.

[108] J. Kestin, L. Persen, The transfer of heat across a turbulent boundary layer at very high Prandtl numbers, Int. J. Heat Mass Tran. 5 (1962) 355–371.

[109] R. Seban, R. Bond, Skin friction and heat transfer characteristics of a laminar boundary layer on a cylinder in axial flow, J. Aeronaut. Sci. 18 (1951) 671–675.

[110] L. Verlet, Computer "Experiments" on Classical Fluids. I. Thermodynamical Properties of Lennard-Jones Molecules, Phys. Rev. 159 (1) (1967) 98.

[111] A. Tarantola, Inverse Problem Theory and Methods for Model Parameter Estimation, Society for Industrial and Applied Mathematics, Philadelphia, PA, USA, 2004.

[112] A. Barat, H. J. Ruskin, M. Crane, Probabilistic models for drug dissolution. Part 1. Review of Monte Carlo and stochastic cellular automata approaches, Simul. Model. Pract. Th. 14 (2006) 843–856.

[113] A. Barat, H. J. Ruskin, M. Crane, Probabilistic methods for drug dissolution. Part 2. Modelling a soluble binary drug delivery system dissolving in vitro, Simul. Model. Pract. Th. 14 (2006) 857–873.

[114] F. White, Viscous Fluid Flow, 2nd Edition, McGraw-Hill, New York, 1991.

[115] H. Schuh, A new method for calculating laminar heat transfer on cylinders of arbitrary cross-section and on bodies of revolution at constant and variable wall temperature, TN 33, KTH Aero (1954).

[116] H. Schuh, On asymptotic solutions for the heat transfer at varying wall temperatures in a laminar boundary layer with Hartree's velocity profiles, J. Aero. Sci. 20(2) (1953) 146–147.

[117] H. Schlichting, Boundary-Layer Theory, 7th Edition, McGraw-Hill, New York, 1979.

[118] H. Martin, The Generalized Lévêque Equation And Its Practical Use For The Prediction Of Heat And Mass Transfer Rates From Pressure Drop, Chem. Eng. Sci. 57 (16) (2002) 3217–3223.

[119] S.-C. Chang, J. Jin, Computation of special functions, 2nd Edition, Wiley-Interscience, New York, 1996.

[120] M. Dehghan, Weighted finite difference techniques for the one-dimensional advection-diffusion equation, Appl. Math. Comput. 147 (2004) 307 – 319.

[121] J. Alden, Computational electrochemistry, Ph.D. thesis, Oxford University (1998).

URL `http://physchem.ox.ac.uk/~rgc/john/Thesis/`

[122] M. Dehghan, Numerical solution of the three-dimensional advection-diffusion equation, Appl. Math. Comput. 150 (2004) 5 – 19.

[123] M. Dehghan, Numerical schemes for one-dimensional parabolic equations with nonstandard initial condition, Appl. Math. Comput. 147 (2004) 321–331.

[124] B. Laval, B. R. Hodges, J. Imberger, Numerical Diffusion in Stratified Lake Models, Proc. 5th Intl. Symposium on Stratified Flows, Vancouver July 7-11, 2000.

[125] B. Ataie-Ashtiani, D. Lockington, R. Volker, Truncation errors in finite difference models for solute transport equation with first-order reaction, J. Contam. Hydrol. 35 (1999) 409–428.

[126] J. Liu, E. S. Oran, C. R. Kaplan, Numerical diffusion in the FCT algorithm, revisited, J. Comp. Phys. 208 (2005) 416434.

[127] R. F. Warming, B. J. Hyett, The modified equation approach to the stability and accuracy analysis of finite-difference methods, J. Comput. Phys. 14 (2) (1974) 159–179.

[128] J. Alden, J. Booth, R. G. Compton, R. A. Dryfe, G. H. Sanders, Diffusional mass transport to microband electrodes of practical geometries: A simulation study using the strongly implicit procedure, J. Electroanal. Chem. 389 (1-2) (1995) 45–54.

[129] M. Dehghan, Quasi-implicit and two-level explicit finite-difference procedures for solving the one-dimensional advection equation, Appl. Math. Comput. 167 (2005) 46–67.

[130] V. Vemuri, W. J. Karplus, Digital Computer Treatment of Partial Differential Equations, Prentice-Hall, New Jersey, 1981.

[131] L. Chung-Yau, Applied Numerical Methods for Partial Differential Equations, Prentice Hall [Simon and Schuster (Asia) Pte Ltd.], Singapore, 1994.

[132] M. Thompson, O. V. Klymenko, R. G. Compton, Modelling homogeneous kinetics in the double channel electrode, J. Electroanal. Chem. 576 (2) (2005) 333 – 338.

[133] C. J. Freitas, Editorial policy statement on the control of numerical accuracy, ASME J. Fluids Eng. 115 (1993) 339–340.
URL http://journaltool.asme.org/Templates/JFENumAccuracy.pdf

[134] D. Britz, Investigation into the relative merits of some n-point current approximations in digital simulation, Anal. Chim. Acta 193 (1987) 277–285.

[135] D. E. Knuth, Big omicron and big omega and big theta, SIGACT News 8 (2) (1976) 18–24.

[136] D. Gavaghan, How accurate is your two-dimensional numerical simulation? Part 1. an introduction, J. Electroanal. Chem. 420(1-2) (1997) 147–158.

[137] L. Ehrlich, A numerical method of solving a heat flow problem with moving boundary, J. ACM 5 (1958) 161–176.

[138] L. Thomas, Elliptic problems in linear difference equations over a network, Watson Sci. Comput. Lab. Report, Columbia University (1949).

[139] G. Bruce, D. Peaceman, Rachford, H. H. Jr., Rice, J.D., Calculations of unsteady-state gas flow through porous media, Petroleum Transactions, AIME 198 (1953) 79–92.

[140] W. J. Minkowycz, G. E. Schneider, R. H. Pletcher, E. M. Sparrow, Handbook of Numerical Heat Transfer, John Wiley & Sons, Inc., New York etc., 1988.

[141] A. C. Fisher, R. G. Compton, Chronoamperometry at Channel Electrodes: A General Computational Approach, J. Phys. Chem. 95 (19) (1991) 7538–7542.

[142] C. J. Freitas, The issue of numerical uncertainty, App. Math. Model. 26 (2002) 237–248.

[143] J. Zhu, H. Guowei, Error estimation and uncertainty propagation in computational fluid mechanics, ICASE Interim Report 41, NASA (2002).

[144] I. Celik, Procedure for estimation and reporting of discretization error in CFD applications, in: C. Freitas (Ed.), Editorial Policy Statement on the Control of Numerical Accuracy, J. Fluids Eng., 2005.
URL http://journaltool.asme.org/Templates/JFENumAccuracy.pdf

[145] W. L. Oberkampf, Discussion: 'Comprehensive Approach to Verification and Validation of CFD Simulations - Part 1: Methodology and Procedures' (Stern, F., Wilson, R. V., Coleman, H. W., and Paterson, E. G., 2001, ASME J. Fluids Eng., 123, pp. 793802), ASME J. Fluid Eng. 124(3) (2002) 809–810.

[146] F. Stern, H. W. Coleman, E. G. Paterson, Comprehensive Approach to Verification and Validation of CFD Simulations - Part 1: Methodology and Procedures, J. Fluid. Eng. - T. ASME 123(4) (2000) 793–802.

[147] American Institute of Aeronautics and Astronautics, Recommended Practice for The CFD General Notation System - Standard Interface Data Structures (AIAA R-101-2002), AIAA Standards Series (2002).

[148] B. H. Thacker, ASME standards committee on verification and validation in computational solid mechanics, Report, The American Society of Mechanical Engineers (ASME) Council on Codes and Standards (Sep 2001).

[149] I. Celik, Numerical uncertainty in fluid flow calculations: Needs for future research, J. Fluid Eng. 115 (1993) 194 – 195.

[150] L. F. Richardson, The Approximate Arithmetical Solution by Finite Differences of Physical Problems Involving Differential Equations, with an Applica-

tion to the Stresses in a Masonry Dam, Philos. T. R. Soc. A 210 (1911) 307 – 357.

[151] L. F. Richardson, J. A. Gaunt, The Deferred Approach to the Limit. Part I. Single Lattice. Part II. Interpenetrating Lattices, Philos. T. R. Soc. A 226 (1927) 299 – 361.

[152] I. Celik, J. Li, G. Hu, C. Shaffer, Limitations of Richardson Extrapolation and Some Possible Remedies, J. Fluids Eng. 127(4) (2005) 795–805.

[153] W. L. Oberkampf, T. G. Trucano, Verification and validation in computational fluid dynamics, Prog. Aerosp. Sci. 38 (2002) 209 – 272.

[154] W. L. Oberkampf, T. G. Trucano, C. Hirsch, Verification, validation, and predictive capability in computational engineering and physics, SAND REPORT SAND2003-3769, Sandia (2003).
URL `http://www.prod.sandia.gov/cgi-bin/techlib/access-control.pl/2002/023769.pdf`

[155] D. Britz, Brute force digital simulation, J. Electroanal. Chem. 406 (1-2) (1996) 15–21.

[156] D. Britz, Stability of the backward differentiation formula (firm) applied to electrochemical digital simulation, Comput. Chem. 21 (2) (1997) 97–108.

[157] D. Britz, O. Østerby, J. Strutwolf, Damping of Crank-Nicolson error oscillations, Comp. Bio. Chem. 27 (3) (2003) 253–263.

[158] J. A. Cooper, R. G. Compton, Channel electrodes - a review, Electronanal. 10 (3) (1998) 141 – 155.

[159] R. Ferrigno, P. F. Brevet, H. H. Girault, Finite element simulation of the chronoamperometric response of recessed and protruding microdisc electrodes, Electrochim. Acta 42 (12) (1997) 1895–1903.

[160] W. Zhang, H. Stone, J. Sherwood, Mass transfer at a microelectrode in channel flow, J. Phys. Chem. 100 (1996) 9462–9464.

[161] N. P. Stevens, A. C. Fisher, Finite Element Simulations in Electrochemistry. 2. Hydrodynamic Voltammetry, J. Phys. Chem. B 101 (1997) 8259–8263.

[162] N. V. Rees, R. A. W. Dryfe, J. A. Cooper, B. A. Coles, R. G. Compton, S. G. Davies, T. D. McCarthy, Voltammetry under High Mass Transport Conditions. A High Speed Channel Electrode for the Study of Ultrafast Kinetics, J. Phys. Chem. 99 (18) (1995) 7096–7101.

[163] P. Laasonen, Über eine Methode zur Lösung der Wärmeleitungs-gleichung, Acta Math-Djursholm 81 (1949) 309–317.

[164] R. G. Compton, B. A. Coles, A. C. Fisher, Chronoamperometry at Channel Electrodes: Theory of Double-Electrodes, J. Phys. Chem. 98 (9) (1994) 2441–2445.

[165] R. G. Compton, R. A. Dryfe, R. G. Wellington, J. Hirst, Modelling electrode reactions using the strongly implicit procedure, J. Electroanal. Chem. 383 (1-2) (1995) 13–19.

[166] J. Galceran, D. J. Gavaghan, J. S. Rollett, Two-dimensional implementation of the finite element method with singularity correction for diffusion limited current at an unshielded disc electrode, J. Electroanal. Chem. 394 (1-2) (1995) 17–28.

[167] C. Amatore, I. Svir, A new and powerful approach for simulation of diffusion at microelectrodes based on overlapping sub-domains: application to chronoamperometry at the microdisk, J. Electroanal. Chem. 557 (2003) 75–90.

[168] D. Gavaghan, J. Rollett, Correction of boundary singularities in numerical

simulation of time-dependent diffusion processes at unshielded disc electrodes, J. Electroanal. Chem. 295 (1990) 1–14.

[169] H. Motz, The Treatment of Singularities of Partial Differential Equations by Relaxation Methods, Quart. Appl. Maths IV (4) (1946) 371–377.

[170] L. Woods, The Relaxation Treatment of Singular Points in Poisson's Equation, Quart. Journ. Mech. and Applied Math. VI (2) (1953) 163–185.

[171] L. Fox, R. Sankar, Boundary singularities in linear elliptic differential equations, J. Inst. Math. Appl. 5 (1969) 340–350.

[172] D. Britz, The Saul'yev method of digital simulation under derivative boundary conditions, Anal. Chim. Acta 239 (1990) 87–93.

[173] A. Michael, R. Wightman, C. Amatore, Part I. Digital Simulation with a Conformal Map, J. Electroanal. Chem. 267 (1989) 33–45.

[174] L. K. Bieniasz, Use of dynamically adaptive grid techniques for the solution of electrochemical kinetic equations. part 2. an improved finite-difference adaptive moving grid technique for one-dimensional fast homogeneous reaction-diffusion problems with reaction layers at the electrodes, J. Electroanal. Chem. 374 (1994) 1–22.

[175] J. Strutwolf, D. E. Williams, Digital simulation of two-dimensional mass transfer problems in electrochemistry using the extrapolation method, Electroanal. 11 (7) (1999) 487–493.

[176] J. Strutwolf, D. E. Williams, Electrochemical sensor design using coplanar and elevated interdigitated array electrodes. a computational study, Electroanal. 17 (2) (2004) 169–177.

[177] R. Ferrigno, P. F. Brevet, H. H. Girault, Finite element simulation of the

amperometric response of recessed and protruding microband electrodes in flow channels, J. Electroanal. Chem. 430 (1-2) (2003) 235–242.

[178] D. Gavaghan, An exponentially expanding mesh ideally suited to the fast and efficient simulation of diffusion processes at microdisc electrodes. 1. derivation of the mesh, J. Electroanal. Chem. 456 (1-2) (1998) 1–12.

[179] D. Gavaghan, An exponentially expanding mesh ideally suited to the fast and efficient simulation of diffusion processes at microdisc electrodes. 2. application to chronoamperometry, J. Electroanal. Chem. 456 (1-2) (1998) 13–23.

[180] D. Gavaghan, Two-dimensional implementation of the finite element method with singularity correction for diffusion limited current at an unshielded disc electrode, J. Electroanal. Chem. 394 (1995) 17–28.

[181] S. W. Feldberg, C. I. Goldstein, Examination of the behavior of the fully implicit finite-difference algorithm with the Richtmyer modification: behavior with an exponentially expanding time grid, J. Electroanal. Chem. 397 (1995) 1–2.

[182] M. Lutz, Python Pocket Reference, 2nd Edition, O'Reilly & Associates, Inc., Sebastopol, CA, USA, 2001.

[183] Python Software Foundation, The Python Programming Language, [Online], [14 November 2006] (2006).
URL `http://www.python.org/`

[184] Biopython Project, Biopython, [Online; accessed 16-November-2006] (2006).
URL `http://biopython.org/`

[185] G. van Rossum, Foreword for "Programming Python" (1st Ed.), in: Programming Python by Mark Lutz, 1st Edition, O'Reilly & Associates, Inc., Sebastopol, CA, USA, 1996.

[186] J. K. Ousterhout, Scripting: Higher-level programming for the 21st century, Computer 31 (3) (1998) 23–30.

[187] D. Beazley, P. Lomdahl, Feeding a Large Scale Physics Application to Python (1997).
URL citeseer.ist.psu.edu/article/beazley97feeding.html

[188] CGNS Project Group, CGNS Documentation Home Page, [Online], [10 November 2006] (2006).
URL http://www.grc.nasa.gov/WWW/cgns/

[189] T. Williams, C. Kelley, GNUPLOT, An Interactive Plotting Program, [Online; accessed 16-November-2006] (2006).
URL http://www.gnuplot.info/docs/gnuplot.html

[190] T. Kawano, Gnuplot - Not So Frequently Asked Questions, [Online; accessed 27-August-2007] (2007).
URL http://t16web.lanl.gov/Kawano/gnuplot/index-e.html

[191] S. Gundavaram, CGI Programming on the World Wide Web, 1st Edition, O'Reilly, New York, 1996.

[192] N. Sastry, Visualize Your Data with Gnuplot, [Online; accessed 27-August-2007] (2004).
URL http://www.ibm.com/developerworks/library/l-gnuplot/

[193] L. Prandtl, O. Tietjens, Fundamentals of Hydro- and Aeromechanics, Dover Publications, New York, 1934.

[194] J. Heller, Fundamentals of polymer science, in: J. R. Robinson, V. H. Lee (Eds.), Controlled Drug Delivery, Fundamentals and Applications, 2nd Edition, Vol. 29, Dekker, New York, 1987, p. 206.

[195] H. Schlichting, Lecture Series "Boundary Layer Theory" Part I - Laminar Flows, TM 1217, NACA (1949).

[196] L. K. Bieniasz, O. Østerby, D. Britz, Numerical stability of finite difference algorithms for electrochemical kinetic simulations: Matrix stability analysis of the classic explicit, fully implicit and Crank-Nicolson methods and typical problems involving mixed boundary conditions, Comput. Chem. 19 (1995) 351.

[197] B. Ataie-Ashtiani, S. Hosseini, Error analysis of finite difference methods for two-dimensional advection-dispersion-reaction equation, Adv. Water Resour. 28 (8) (2005) 793–806.

[198] O. Østerby, Five ways of reducing the Crank-Nicolson oscillations, Daimi PB-558, Department of Computer Science, Aarhus University (2004).

[199] European Wind Energy Association, Wind Force 12, Report (2005).
URL `http://www.ewea.org/`

[200] E. L. Petersen, N. G. Mortensen, L. Landberg, J. Højstrup, H. P. Frank, Wind power meteorology. Part II: siting and models, Wind Energ. 1 (2) (1998) 55–72.

[201] S. Frandsen, I. Antoniou, J. C. Hansen, L. Kristensen, H. A. Madsen, B. Chaviaropoulos, D. Douvikas, J. A. Dahlberg, A. Derrick, P. Dunbabin, R. Hunter, R. Ruffle, D. Kanellopoulos, G. Kapsalis, Redefinition power curve for more accurate performance assessment of wind farms, Wind Energ. 3 (2) (2000) 81–111.

[202] N. Jenkins, Engineering wind farms, Power Eng. J. 7 (2) (1993) 53–60.

[203] IEA, Recommended Practices for Wind Turbine Testing and Evaluation, 11.

Wind Speed Measurement and Use of Cup Anemometry. 1st Edition, IEA Recommendations, available from: `www.iea.org` (1999).

[204] C.-W. Park, S.-J. Lee, Free end effects on the near wake flow structure behind a finite cylinder, J. Wind Eng. Ind. Aerod. 88 (2-3) (2000) 231–246.

[205] J. Kline, Effects of Tubular Towers on Wind Speed Measurements, in: Proceedings of the American Wind Energy Association Conference, 2002.

[206] J. Franke, W. Frank, Large eddy simulation of the flow past a circular cylinder at $Re_D = 3900$, J. Wind Eng. Ind. Aero. 90 (10) (2002) 1191–1206.

[207] F. H. Durgin, C. J. Pastrone, O. B. Marenzi, Comparison of measured wind velocities from the top of an 800 foot tower in Boston and Logan Airport Boston, J. Wind Eng. Ind. Aerod. 36 (1-3) (1990) 403–413.

[208] S.-H. Shin, R. N. Meroney, R. L. Ewald, D. E. Neff, Effect of upwind obstacles and meteorological tower structure on sensor measurements, J. Wind Eng. Ind. Aerod. 36 (1-3) (1990) 371–379.

[209] Brady, Oisín (Thales-Ventec) , Personal Communication (2006).

[210] L. Prandtl, O. Tietjens, Applied Hydro- and Aeromechanics, Dover Publications, New York, 1934.

[211] G. K. Batchelor, An Introduction to Fluid Dynamics, Cambridge University Press, Cambridge, 1967.

[212] M. Coutanceau, J. Defaye, Circular cylinder wake configurations: A flow visualization survey, Appl. Mech. Rev. 44 (6).

[213] W. Lindsey, Drag of cylinders of simple shapes, NACA Report 619, NACA (1937).

[214] C. Wieselsberger, New data on the laws of fluid resistance, TN 84, NACA (1922).

[215] A. Zahm, Flow and drag formulas for simple quadrics, NACA Report 253, NACA (1937).

[216] C. Apelt, The Steady Flow of a Viscous Fluid Past a Circular Cylinder at Reynolds Numbers 40 and 44, ARC R & M 3175.

[217] Y. Liu, R. M. C. So, Z. X. Cui, A finite cantilivered cylinder in a cross-flow, J. Fluids Struc. 20 (2005) 589–609.

[218] Y. Uematsu, M. Yamada, Aerodynamic forces on circular cylinders of finite height, J. Wind Eng. Ind. Aero. 51 (2) (1994) 249–265.

[219] R. I. Basu, Aerodynamic Forces on Structures of Circular Cross-Section. Part 2. The Influence of Turbulence and Three-Dimensional Effects, J. Wind. Eng. 24 (1986) 33–59.

[220] S. Luo, T. Gan, Y. T. Chew, Uniform flow past one (or two in tandem) finite length circular cylinder(s), J. Wind Eng. Ind. Aero. 59 (1) (1996) 69–93.

[221] J. M. Cimbala, FLUENT and Gambit Learning Modules, [Online].
URL `http://www.me.psu.edu/cimbala/`

[222] E. Romeo, C. Royo, A. Monzón, Improved explicit equations for estimation of the friction factor in rough and smooth pipes, Chem. Eng. J. 86 (3) (2002) 369–374.

[223] W. Gong, A. Ibbetson, A wind tunnel study of turbulent flow over model hills, Bound-Lay. Meteorol. 49 (1-2) (1989) 113–148.

[224] J. J. Finnigan, M. R. Raupach, E. F. Bradley, G. K. Aldis, A wind tunnel study of turbulent flow over a two-dimensional ridge, Bound-Lay. Meteorol. 50 (1-4) (1990) 277–317.

[225] S. E. Belcher, J. C. R. Hunt, Turbulent flow over hills and waves, Annu. Rev. Fluid Mech. 30 (1998) 507–538.

[226] N. R. Bergrun, A method for numerically calculating the area and distribution of water impingement on the leading edge of an airfoil in a cloud, NACA Report 1397, NACA (1947).

[227] R. J. Brun, H. M. Gallagher, D. E. Vogt, Impingement of water droplets on NACA 65(1)-208 and 65(1)-212 airfoils at 4 degrees angle of attack, NACA Report 2952, NACA (1953).

[228] W. Pracht, Calculating three-dimensional fluid flows at all speeds with an Eulerian-Lagrangian computing mesh, J. Comput. Phys. 17 (1975) 132–159.

[229] Q. Zhou, M. Leschziner, An improved particle-locating algorithm for Eulerian-Lagrangian computations of two-phase flows in general coordinates, Int. J. Multiphas. Flow 25 (5) (1999) 813–825.

[230] N. Mordant, J.-F. Pinton, Velocity measurement of a settling sphere, Eur. Phys. J. B 18 (2000) 343–352.

[231] D. Auerbach, Some limits to Stokes' law, Am. J. Phys. 56 (9) (1988) 850–851. URL doi:10.1119/1.15442

[232] E. Loth, Numerical approaches for motion of dispersed particles, droplets and bubbles, Prog. Energ. Combust. 26 (3) (2000) 161–223.
URL doi:10.1016/S0360-1285(99)00013-1

[233] R. Chordá, J. Blasco, N. Fueyo, An efficient particle-locating algorithm for application in arbitrary 2D and 3D grids, Int. J. Multiphas. Flow 28 (9) (2002) 1565–1580.

[234] R. Löhner, Robust, vectorized search algorithms for interpolation on unstructured grids, J. Comput. Phys. 118.

URL http://www.ingentaconnect.com/content/ap/cp/1995/00000118/00000002/art01107

[235] Lawrence Livermore National Laboratory, VisIt, [Online], [April 18th 2006] (2006).
URL http://www.llnl.gov/visit/

[236] D. Poirier, S. R. Allmaras, D. R. McCarthy, M. F. Smith, F. Y. Enomoto, The CGNS System, in: AIAA, Fluid Dynamics Conference, 29th, Albuquerque, NM, USA, 1998.
URL http://www.grc.nasa.gov/WWW/cgns/papers/aiaa98-3007.pdf

[237] C. Rumsey, D. Poirier, R. Bush, C. Towne, User's Guide to CGNS (2001).
URL citeseer.ist.psu.edu/rumsey01users.html

[238] N. Pirzkal, R. N. Hook, Python in Astronomy, in: D. M. Mehringer, R. L. Plante, D. A. Roberts (Eds.), ASP Conf. Ser. - Astronomical Data Analysis Software and Systems VIII, Vol. 172, San Francisco, 1999.

[239] G. B. J. Thomas, R. L. Finney, Calculus and Analytic Geometry, 8th Edition, Addison-Wesley, Reading, Massachusetts etc., 1992.

[240] M. Abramowitz, I. A. Stegun, Handbook of mathematical functions, 10th Edition, Applied Mathematics Series - 55, National Bureau of Standards, 1972.

[241] A. Cromer, Stable solutions using the Euler approximation, Am. J. Phys. 49 (5) (1981) 455–459.

[242] I. Gatland, Numerical integration of Newtons equations including velocity-dependent forces, Am. J. Phys. 62 (1994) 259.

[243] D. Darmofal, R. Haimes, An Analysis of 3D Particle Path Integration Algorithms, J. Comput. Phys. 123 (14) (1996) 182–195.

[244] A. Bellemans, Stable algorithms for integrating Newtons equation, Am. J. Phys. 51 (1983) 275.

[245] W. Drish Jr, W. Wild, Numerical solutions of Van der Pols equation, Am. J. Phys. 51 (1983) 439.

[246] R. Stanley, Numerical methods in mechanics, Am. J. Phys. 52 (1984) 499.

[247] H. Laue, Elementary numerical integration methods, Am. J. Phys. 56 (1988) 849.

[248] S. Eubank, W. Miner, T. Tajima, J. Wiley, Interactive computer simulation and analysis of Newtonian dynamics, Am. J. Phys. 57 (1989) 457.

[249] K. Lemmens, An Investigation, Implementation and Comparison of 3 Important Particle Simulation Techniques: PP: Particle-Particle PM: Particle-Mesh and TC: Tree-Code, Report, Faculty of Applied Physics, University of Technology, Delft (1997).

[250] H. Ingram, A comparison of digital computer programs for the numerical solution of ordinary differential equations, Rep. NASA TMX-64781, Marshall Space Flight Center, Alabama.

[251] F. Calvino, C. Martinez, Educational Software. Simulation of Charged Particle Trajectories in Presence of Magnetic Fields, in: Proceedings of the European Particle Accelerator Conference, Sitges, Barcelona, 1996.

[252] A. Smirnov, I. Celik, A Lagrangian Particle Dynamics Model with an Implicit Four-Way Coupling Scheme, in: Proceedings of IMECE00, International Mechanical Engineering Congress & Exposition, Orlando, Fl., USA, 2000.

[253] W. C. Swope, H. C. Andersen, P. H. Berens, K. R. Wilson, A computer simulation method for the calculation of equilibrium constants for the formation of

physical clusters of molecules: Application to small water clusters, J. Chem. Phys. 76 (1) (1982) 637–649.

[254] F. H. Garner, R. W. Grafton, Mass transfer in fluid flow from a solid sphere, Proc. R. Soc. A 224 (1156) (1954) 64–82.
URL http://www.jstor.org/stable/99506

[255] P. Harriott, Mass transfer to particles: Part i. suspended in agitated tanks, AIChE J. 8 (1) (1962) 93–101.
URL http://dx.doi.org/10.1002/aic.690080122

[256] P. Harriott, Mass transfer to particles: Part ii. suspended in a pipeline, AIChE J. 8 (1) (1962) 101–102.
URL http://dx.doi.org/10.1002/aic.690080123

[257] D. N. Miller, Scale-up of agitated vessels. mass transfer from suspended solute particles, Ind. Eng. Chem. Proc. Des. Dev. 10 (3) (1971) 365–375.
URL http://pubs3.acs.org/acs/journals/doilookup?in_doi=10.1021/i260039a015

[258] D. M. D'Arcy, O. I. Corrigan, A. M. Healy, Evaluation of hydrodynamics in the basket dissolution apparatus using computational fluid dynamics–dissolution rate implications, Eur. J. of Pharm. Sci. 27 (2-3) (2006) 259–267.
URL http://www.sciencedirect.com/science/article/B6T25-4HNSG3N-1/1/1be6fd2f9fcf182b804ec886ebfb4891

[259] D. N. Kenwright, G. D. Mallinson, A 3-d streamline tracking algorithm using dual stream functions, in: VIS '92: Proceedings of the 3rd conference on Visualization '92, IEEE Computer Society Press, Los Alamitos, CA, USA, 1992, pp. 62–68.

[260] B. Wedan, ADFviewer, [Online; accessed 16-November-2006] (2006).

URL http://www.grc.nasa.gov/WWW/cgns/cgnstools/adfviewer/index.html

[261] N. McMahon, M. Crane, H. J. Ruskin, L. Crane, The importance of boundary conditions in the simulation of dissolution in the usp dissolution apparatus, Simul. Model. Pract. Th. 15 (3) (2007) 247–255.

[262] E. Loth, On comparing finite difference schemes applied to nolinear multi-region heat and mass transfer problem, Comput. Mech. 28 (2002) 55–62.

[263] H. Werlé, M. Gallon, Flow Control by Cross Jet, Aeronaut. Astronaut. (34) (1972) 21–33.

[264] C. Norberg, Effects of Reynolds number and low-intensity free-stream turbulence on the flow around a circular cylinder, Publ. No. 87/2, Department of Applied Thermoscience and Fluid Mechanics, Chalmers University of Technology (1987).

[265] J. Son, T. Hanratty, Velocity gradients at the wall for flow around a cylinder at Reynolds numbers from 5×10^3 to 10^5, J. Fluid. Mech. (1969) 353–368.

[266] Y. Uematsu, Aeroelastic behavior of a pair of thin circular cylindrical shells in staggered arrangement, J. Wind Eng. Ind. Aero. 22 (1) (1986) 23–41.

Glossary

ADF: Advanced Data Format.

AIAA: American Institute of Aeronautics and Astronautics.

API: Application Programming Interface.

CFD: Computational Fluid Dynamics.

CGNS: CFD General Notation System.

CN: Crank-Nicolson (finite-difference scheme).

DCU: Dublin City University.

DDS: Drug Delivery System.

EMEA: European Medicines Agency.

FD: Finite Difference.

FDA: Food and Drug Administration (US Federal Agency).

HCl: Hydrogen Chloride (in water, Hydrochloric Acid).

IND: Investigational New Drug Application.

In silico: Computer model, a more easily remembered modification of the Latin *in silicio*.

In vivo: within a living organism.

In vitro: in an artificial environment outside the living organism.

IVIVC: *In Vitro/In Vivo* Correlation.

NACA: National Advisory Committee for Aeronautics.

NCE: New Chemical Entity.

NICB: National Institute for Cellular Biotechnology.

PBPK: Physiologically Based Pharmacokinetic.

(Base) Pressure Coefficient: the base pressure coefficient C_{pb} can be derived from Bernoulli's equation, $p + \frac{1}{2}\rho V^2 = \text{const}$, where ρ is the fluid density. This can be re-written as $p_s = p_\infty + \frac{1}{2}\rho U_\infty^2(1 - 4\sin^2\theta)$ for flow about a cylinder. C_{pb} can then be written, $C_{pb} = \frac{p_s - p_\infty}{\frac{1}{2}\rho U_\infty^2}$.

PSUDO: Parallel Simulation of Drug Release Code [20].

R&D: Research and Development.

Reynolds Number: the Reynolds number (Re) is the ratio of the inertial forces of the flow to the viscous or frictional forces and is normally expressed in the form, $Re = \frac{UL}{\nu}$, where U is the flow velocity, L is a representative dimension of the flow and ν is the viscosity of the fluid. For flows about cylinders and spheres, L is normally taken to be the diameter.

Schmidt Number: the Schmidt number is defined as the ratio of kinematic viscosity to diffusivity, i.e. $Sc = \frac{\nu}{D}$.

TCD: Trinity College Dublin.

TDMA: Tridiagonal Matrix Algorithm.

USP: United States Pharmacopeia.

w/w: *by weight*, the concentration of a substance in a mixture or solution expressed as a % of the total mass.

Appendices

Published Papers